DOT/FAA/TC-18/5

Federal Aviation Administration
William J. Hughes Technical Center
Aviation Research Division
Atlantic City International Airport
New Jersey 08405

Delamination/Disbond Arrest Features in Aircraft Composite Structures

June 2018

Final Report

U.S. Department of Transportation
Federal Aviation Administration

NOTICE

Technical Report Documentation Page

1. Report No.	2. Government Accession No.	3. Recipient's Catalog No.
DOT/FAA/TC-18/5		

4. Title and Subtitle	June 2018
DELAMINATION/DISBOND ARREST FEATURES IN AIRCRAFT COMPOSITE STRUCTURES	6. Performing Organization Code AIR-600

7. Author(s)	8. Performing Organization Report No.
Kuen Y. Lin, Luke Richard and Chi Ho Eric Cheung	

9. Performing Organization Name and Address	10. Work Unit No. (TRAIS)
University of Washington, William E. Boeing Department of Aeronautics and Astronautics, P.O. Box 352400, Seattle, WA 98195	11. Contract or Grant No.

12. Sponsoring Agency Name and Address	13. Type of Report and Period Covered
FAA Northwest Mountain Regional Office 1601 Lind Ave SW Renton, WA 98057	Final Report 14. Sponsoring Agency Code AIR-600

15. Supplementary Notes

The FAA William J. Hughes Technical Center Aviation Research Division CORs were Lynn Pham and Curtis Davies

16. Abstract

Experimental and analytical study was conducted to assess the arrest capability of fasteners in composite structures. The results of the study verified the fail-safe nature of fastened composite structures in delaminations, with the size, spacing, and installation treatment of the fastener determined by the maximum allowable crack length. The primary drivers of the crack arrest mechanism are the elimination of the mode I delamination through the fastener clamping and shear engagement of the fastener shank, and frictional load transfer providing load alleviation at the crack tip. The installation torque and level of clearance in the fastener hole influenced the second two methods of crack arrest, whereas all tested fastener sizes successfully provided mode I elimination. It is important to note that the fastener provided this arrest capability only after the crack had reached or passed the fastener. This constrains the design of the parameters because the fastener location and pitch must account for growth prior to the installation point.

Analysis of the system showed the capability of accurately capturing the delamination propagation in relation to the applied loading, allowing for analysis of fastened composite structures in service. One-, two-, and three-dimensional models were generated, each matching the experimental data and providing varying levels of detail. The three-dimensional model captured the curvature of the crack front generated by the installation of the fastener, whereas the one- and two-dimensional models assumed a flat crack front with the length of the crack correlating well to the measured values along the side of the specimens tested.

Experimental work was conducted to verify the modeling predictions. The initial test article that generated a pure mode II delamination front proved to be weaker in tension than in delamination and prompted the design of a mixed-mode specimen, which was retained for subsequent testing. A novel test specimen was chosen to provide adequate crack propagation length through the specimen without creating an excessively long or thick sample, as an end-notched flexure would have necessitated.

17. Key Words	18. Distribution Statement
Composites, Carbon/epoxy, Bonded, Bolted structures, Delamination arrest, Mode I, Mode II fracture	This document is available to the U.S. public through the National Technical Information Service (NTIS), Springfield, Virginia 22161. This document is also available from the FAA William J. Hughes Technical Center at actlibrary.tc.faa.gov.

19. Security Classif. (of this report)	20. Security Classif. (of this page)	21. No. of Pages	22. Price
Unclassified	Unclassified	109	

ACKNOWLEDGEMENTS

This study was jointly sponsored by the FAA through AMTAS (Advanced Materials in Transport Aircraft Structures at The University of Washington), The Boeing Company, and Toray Composite Materials America, Inc. The authors wish to thank Eric Sager, Marc Piehl, Gerald Mabson, Eric Cregger, Matt Dilligan of Boeing, Kenichi Yoshioka, Don Lee of Toray, and Lynn Pham, Curt Davies, and Dr. Larry Ilcewicz of the FAA for their support and discussion.

TABLE OF CONTENTS

APPENDICES

LIST OF FIGURES

LIST OF TABLES

LIST OF ACRONYMS

DCB	Double cantilever beam
ENF	End-notched flexure
FEA	Finite element analysis
FEM	Finite element modeling
FHT	Filled hole tension failure
G_I	Mode 1 strain energy release rate
G_{II}	Mode 2 strain energy release rate
G_{IC}	Mode 1 critical strain energy release rate
G_{IIC}	Mode 2 critical strain energy release rate
NA	No crack observed before failure
OHT	Open hole tension failure
PMPE	Principle of minimum potential energy
SERR	Strain energy release rate
VCCT	Virtual crack closure technique

EXECUTIVE SUMMARY

Delaminations are one of the primary damage mechanisms in composite structures and, therefore, delamination arrest is a key area of research. The work in this report focused on the use of fasteners as a delamination arrest feature. Arrest fasteners can be used in a dual-use role, both for load transfer and delamination arrest. Fasteners are one of the only features that can be successfully used in thick pre-preg composite structures because other methods cannot penetrate such a thick laminate.

The work performed found that fasteners provide excellent mode I delamination arrest and good mode II delamination resistance. The clamping of the fastener was extremely effective at eliminating mode I delamination, while mode II resistance occurred through shear engagement of the fasteners and load transfer through friction. Multiple fasteners were found to provide greater arrest capability, but each additional fastener does not add to the arrest capability until the crack has reached it, placing a limit on the usefulness of installing an ever-increasing number of fasteners.

1. INTRODUCTION

The increased use of composites in aircraft has enabled the use of large-bonded (including co-cured, co-bonded, and secondary-bonded) structures, with the main advantages being the reduction in part counts and weight. These large integrated structures, in contrast to assembled structures common for metallic aircraft, eliminate many of the mechanical joints, fasteners, and rivets, reducing the cost and complexity associated with this common design approach.

However, the large integrated, laminated structures are susceptible to delamination, a damage mode not encountered in typical metallic structures. Delamination remains one of the key issues for primary structures in composite aircraft because the loss in bending stiffness due to skin-stiffener separation can cause catastrophic failure. As a result, delamination arrest fasteners are installed in the structure to ensure fail safety should the part experience a delamination during service. These are then tested in a point design manner, with large scale components tested to failure to ensure the successful arrest of the delaminations.

This point design approach is inefficient as it simply inserts a large number of fasteners to ensure safety without understanding the underlying mechanism and improving the layout to best arrest the cracks. It is necessary to understand how delaminations grow and interact with the arrest features installed to better design against delamination growth.

The work presented in this report was done to better understand the delamination/disbond arrest process and predict the capability of varying arrest features. It shows that fasteners are extremely effective at suppressing mode I delamination, but not as effective for mode II type propagation. Therefore, the research focuses on delamination growth through fasteners in mode II. A pure mode II specimen was developed with the goal of better understanding the arrest features by avoiding effects of mode mixity.

Initial testing of candidate specimen designs led to difficulties because the original test articles were too delamination-resistant and the composite samples failed in tension, not delamination, during the experiments. Work was shifted toward a mixed-mode delamination specimen, which provided for significant delamination growth prior to net section failure [1 - 3]. Using the currently developed mixed-mode specimen, single fastener experiments were first conducted to better understand the influence of an individual fastener on delamination propagation along the length of the specimen. Because of the success of the mixed-mode delamination specimens, all subsequent tests were based on this, as developed by Bruun et al. [1].

In this study, experiments on both single and multiple fastener samples were conducted under quasi-static loading. In the single fastener case, delamination under mode I was completely suppressed after it reached the fastener. However, mode II propagation began as load was increased by 25%–50%, depending on the clearance, layup, friction coefficient, and installation torque. For the multiple fastener case, the addition of a second fastener did increase arrest capability, with the caveat that each fastener only increased the arrest process after the crack reached that fastener. These experimental results verified initial modeling of the system. Additional work investigated the influence of clearance on the arrest capability of the fastener system, with good agreement between the arrest predictions and experimental work.

A final round of experiments was conducted to verify the strip one-dimensional model assumption, which was used for all the research previously done. Just as in metallic designs, in which a single strip of a fastener array is assumed to behave in a manner identical to the entire pattern, the assumption here was that a single strip with width equal to the fastener pitch would appropriately represent the fastener delamination arrest system. Tests subsequently supported this assumption.

In addition to the experimental work performed, analytical and finite element models were generated that accurately captured the delamination propagation and arrest. Models were created in three levels of complexity using beams, plates, shells, and bricks. The varying levels of complexity for each solution were developed to balance the level of detail in the solution with the complexity of the results. The various analytical solutions and the experiments were in good agreement. Different challenges were encountered for each level of modeling. In particular, the fastener flexibility presented significant challenges for accurately predicting delamination behavior, but this was subsequently rectified.

The arrangement of this report follows the approximate chronological order of the experimental and analytical work, with separate sections detailing the two different aspects. Typically, the modeling and experiments were conducted concurrently, but the model design tended to guide the specimen design. Experimental success or failure led to modifications in both the parts and models.

The final goal of this work was accomplished in understanding the delamination-arrest process through fasteners and making accurate predictions of their arrest capability. Three key parameters contributed to the arrest through fasteners: elimination of mode I when present, load transfer through interfacial friction, and load transfer through shear engagement of the fastener shank.

2. SINGLE-FASTENER EXPERIMENTS

Initial testing and analytical work focused on the delamination response and arrest using a single fastener to best isolate the influence of other fasteners on the system. While initial work also attempted to generate a pure mode II delamination, this design did not provide for adequate crack growth for correlation with analysis. As a result, further testing was performed using a mixed-mode specimen, which generated adequate crack extension prior to net section failure. The first batch of 18 specimens was manufactured by The Boeing Company and were secondary bonded and co-cured. Additional samples were then manufactured at The University of Washington and were co-cured.

2.1 PURE MODE II SPECIMEN [2]

The objective of this work was to design and conduct an experiment to investigate the capability of a fastener to arrest and stabilize pure mode II crack propagation in composite structures. It also sought to develop a closed-form analytical solution to simulate the crack growth of the experimental design and provide a parametric analysis tool.

There has been recent research on fracture testing of bolted and bonded (hybrid) composite joints. A number of tests have been conducted on composite hybrid single lap joints. For example, Jen and Lin [4, 5] performed tensile strength tests of several hybrid single lap configurations with varying stacking sequences, overlap lengths, fastener properties, rivets, and clamping forces. The results showed disbonding of the joint and subsequent loading of the fastener, which, depending on the configuration, continued to carry the joint load. An unavoidable result of a single lap configuration was that disbond occurred as mixed-mode (modes I and II) because of bending of the adherends from the asymmetry of the load path. Lee et al. [6] performed strength testing of composite hybrid double lap joints which has a symmetric load path. Test images showed that failure occurred as disbonding from the single end of the joint and propagated to the fastener, where the load began to be transferred by the fastener. Although the load path was symmetric, there was a peeling force that developed at the end of the joint that caused mixed-mode crack propagation. The review of single and double hybrid lap joints showed that crack propagation was initiated and then followed by loading of the fastener, but disbonding of the joints occurred in mixed-mode, which was undesirable for this study.

Currently there is no ASTM standard for pure mode II interlaminar fracture. The draft standard ASTM D6671 [7] involves interlaminar fracture testing of a three-point end-notched flexure (ENF) specimen for measuring fracture toughness, but the disbonding of the specimen is mixed-mode and does not accommodate a fastener. Testing has been performed with three-point ENF flexural-type specimens that result in pure mode II fracture. For example, Todo et al. [8] performed a quasi-static three-point ENF test to measure the critical strain energy release rate (SERR), G_{IIC}, of composites. The tests successfully resulted in pure mode II crack propagation in the composites. Carlsson et al. [9] conducted a study on the analysis and design of ENF specimens for mode II testing. The study showed that deflection of the ENF must be limited to maintain linear behavior of the specimen. For materials with relatively high fracture toughness, greater loads were required to propagate a crack. Therefore, the thickness of the specimen must be increased to limit deflection. The addition of a fastener increased the effective fracture toughness as a crack grew, and the length available for crack growth became limited. The effect was that the length and thickness of the

specimen became coupled with arrested crack growth, and the specimen became unreasonably long and thick to perform any testing. The ENF tests were specifically designed to provide G_{IIC} values of the material, not to perform crack arrestment tests. Therefore, the ENF configuration was undesirable for the current study.

Research has been conducted on the load transfer by fasteners from multi-row fastener joints. Tate and Rosenfeld [10] developed a solution for the load transferred by fasteners in symmetric butt joints by solving for the fastener compliance. The solution was derived for multi-fastener metallic symmetric butt joints. The total fastener compliance is given as the sum of four individual compliances as follows: fastener shear, fastener bending, fastener bearing, and plate bearing. Based on the assumptions made to generate the model, the authors [10] stated that additional joint configurations would require further testing to accurately apply their equation. More recently, Huth [11] developed an empirical expression for fastener compliance of multi-row single and double lap joints based on empirical data. The solution for fastener compliance is valid for bolted metallic joints, riveted metallic joints, and bolted graphite/epoxy joints. Several experiments were conducted to show that analytical expression accurately predicted the fastener transfer loads. (Huth claimed his solution was more accurate than previously existing expressions.). Although the original study was for single fasteners, the load was not entirely transferred by the single fastener, so it was important to have an expression for faster compliance of multi-row fastened joints. The load was transferred by both the fastener and the bond at the crack tip, which was analogous to a multi-fastener joint.

With disbond and delamination being common failure modes in composites, research was conducted to determine the onset of these failure modes. The virtual crack closure technique (VCCT) is commonly used for a wide variety of applications [12]. VCCT considers the force required to close a crack at a short distance from the crack tip. Based on this information, the load needed for a crack to propagate a small distance is equal to the load required to close the crack. The method is useful because it provides full SERR mode decomposition for modes I, II, and III from relatively simple expressions. VCCT is well suited for finite element modeling (FEM) because it relies on local information at the crack tip; for example, the force between two nodes of adjacent elements. VCCT has been implemented in the commercial FEM code ABAQUS™ [13]. Although it is very useful, VCCT was not desirable for the initial analytical study because the local behavior at the crack tip must be resolved in addition to the global behavior. Wang and Qiao [14] have developed closed-form expressions for the SERR mode I and II decomposition of asymmetric and bi-material double cantilever beams (DCBs), which are subjected to combined axial and transverse loading conditions. The expressions take into account the rotation and shear deformation of the beams at the crack tip. The total SERR is decomposed in modes I and II in a global sense. The research concluded that the developed solution provided better agreement with finite element models than classical solutions. The solution did account for the global behavior of the entire DCB sample, however it was necessary to reduce the region of interest into a DCB-type analysis to apply the solution for fracture analysis of complex structures.

In general, there is a lack of existing experimental work dealing with the ability of a fastener to arrest pure mode II crack propagation. Pure mode II test specimens (e.g., ENF) do exist, but the main purpose of the tests is to obtain material data, G_{IIC}, and they do not accommodate a fastener or relatively large cracks. The existing solutions to predict the onset of fracture, although

sophisticated and powerful, do not directly account for the global behavior of complex structures, such as structures containing fasteners, and the area of fracture must be treated independently. There is a need to develop an interlaminar test specimen that results in pure mode II crack propagation and accommodates a fastener to provide crack arrestment while allowing enough room for a crack to grow. Additionally, there is a need for a simple expression that can predict the behavior of the specimen to aid in design and analysis.

2.1.1 Design of Pure Mode II Specimen

The current standards used to determine the mode II fracture energy are not suitable for delamination arrest experiments. A sample needs to have sufficient size so that the fastener can be installed and the crack can propagate and be arrested, making it unwieldy. Bending split-beam specimens are commonly used to measure the mode II critical SERR, G_{IIC}. Figure 1 gives three examples of such specimens: three-point ENF, four-point ENF, and end-loaded split. The benefit of using bending of a split-beam for mode II crack propagation is the ability to keep the crack tip closed, which keeps G_I at zero. These types of specimens also result in stable crack propagation, which means that multiple measurements can be taken from a single coupon. However, the total deflection of the specimen is limited to maintain linear behavior, which requires a high thickness-to-length ratio, and sufficient length to allow relatively small crack propagation.

Unfortunately, the bending specimens in figure 1 are specifically designed to measure only G_{IIC}. They are not suitable for crack-arrestment tests and typically do not include a fastener. The length available for crack growth is very limited, because it is coupled with the size of the specimen. Only a fraction of the full length of a typical bending specimen can be used for crack propagation. There is not sufficient space for fastener installation to demonstrate the effectiveness of the fastener to arrest a crack. The only way to increase the available crack-growth area is to increase the specimen length, which requires increasing the specimen thickness to maintain linearity or bending failure. Also, as the effective G_{IIC} increases with the presence of a fastener, the amount of deflection required to obtain results increases. This may lead to bending failure before crack arrestment can be tested. The presence of the fastener also introduces a bending moment when loaded, which adds nonlinearity and complexity to the simple split-beam system. The general lack of control in these test parameters means that these specimens are not suitable for this research.

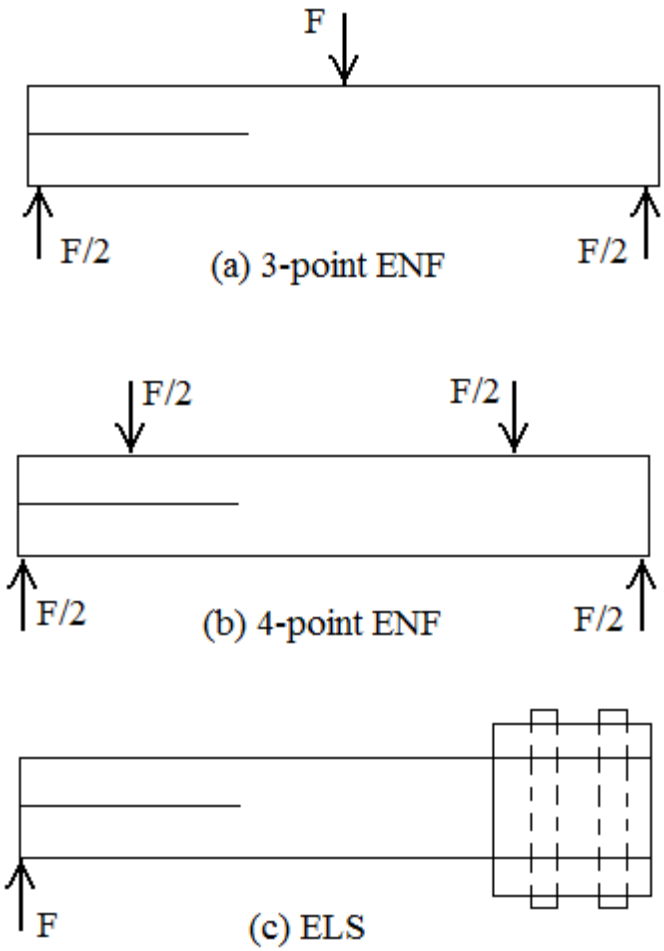

Figure 1. Examples of flexure mode II disbond/delamination test specimens [2]

Because the current flexural specimens were not desirable for fastener-arrest testing, a novel mode II crack-arrestment specimen was developed. The two competing designs shown in figure 2 were initially tested using an axial load frame. When using an axial load frame instead of a bending fixture, the usable specimen length is increased.

Figure 2 shows how the crack propagates under the two different load conditions. The three-beam design ensures that load and deformation will be symmetric about the midplane, which eliminates coupling of out-of-plane bending and extension. The specimen can be lengthened as desired to provide ample space for crack propagation without the need to increase the thickness. This design provides freedom in the choice of different layup combinations because the layup is only limited by the need to accommodate the fastener joint. Such a specimen would be simple to manufacture and easy to test in any axial load frame.

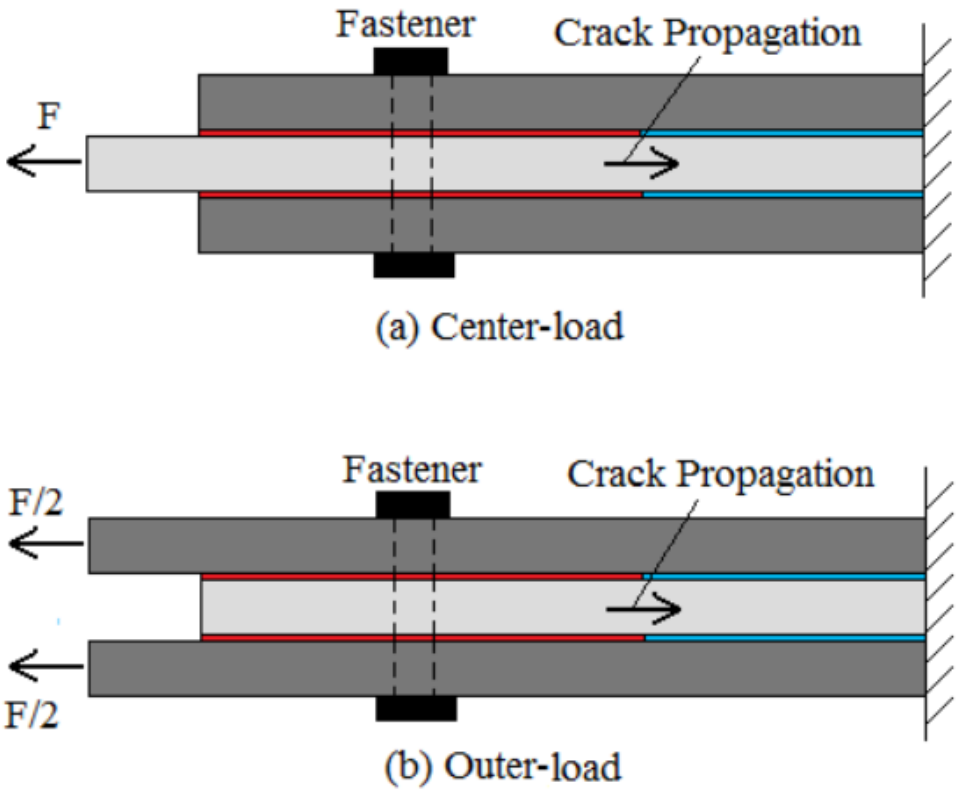

Figure 2. Potential specimen configurations [2]

A finite element model was constructed in ABAQUS to analyze the crack propagation characteristic of the candidate three-beam specimens. The model information is summarized in table 1.

Table 1. Material properties used for the FEM analysis [2]

Parameter	Value
Lamina Properties (AS4/3501-6)	
E_1	18.5 Msi
E_2	1.64 Msi
G_{12}	0.871 Msi
ν_{12}	0.3
Thickness	0.0075 in
Laminate Properties	
Center And Outer Laminate Layups	$[(0/45/90/-45)_3]_S$
G_{IC}	1.5 lb/in
G_{IIC}	7.0 lb/in
Fastener Properties	
E	16.5 Msi
E_x	8.25 Msi
Diameter	0.25 in
Fastener Joint Stiffness	$4.3*10^5$ lb/in
Fastener Axial Stiffness (2 springs)	$2.15*10^5$ lb/in
Element Properties	
Thickness	.0075 in
Width	0.0015 in
Element Type	4-node bi-linear strain quad (CPE4)
Fracture Method	VCCT
Mixed-Mode Fracture Law	Reeder Law (η =1.75)

Msi=megapounds per square inch

Figure 3 shows the finite element analysis (FEA) in a nondeformed state and the deformed states for both center-load and outer-load configurations. The total length of the finite element model is 12.5 inches, and the thickness of each beam is 0.18 inches. The initial crack extends to 4.25 inches from the loaded end of the model (left end in figure 3). The fastener is located at 4.5 inches past the loaded end. This leaves 8.0 inches for the cracks to propagate past the fastener to the fixed end. For the first run, the center beam is uniformly loaded in tension over the cross section at the free end. For the second run, the outer beams are uniformly loaded over the cross section at the free end. A fixed-boundary condition is applied to all three beams at the opposite end. The fastener is modeled as three springs: one spring models the clamping of the fastener, in which no preload is

applied, and the other two model the transverse stiffness of the fastener. Rigid elements are attached to the line of nodes at the location of the fastener and the springs are attached to the rigid element, which prevent excessive deformation that would otherwise occur if the spring were attached to single nodes. Crack propagation is modeled using VCCT. Cracks propagate to the next node when the mixed-mode fracture law (Reeder Law, η=1.75) is reached.

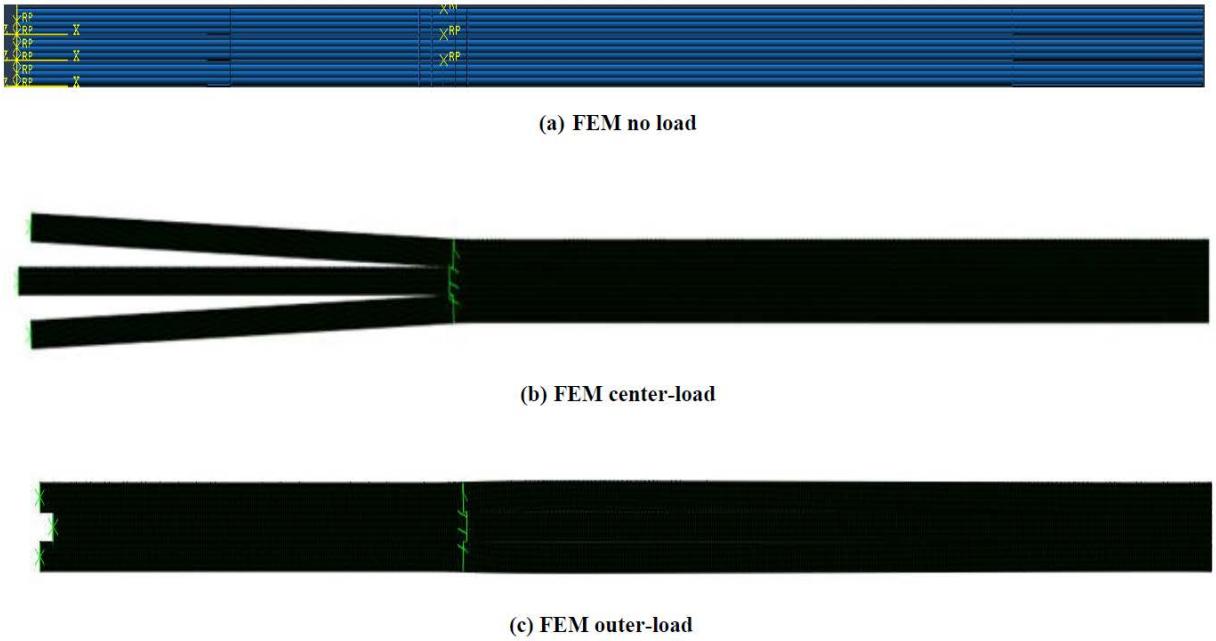

(a) FEM no load

(b) FEM center-load

(c) FEM outer-load

Figure 3. FEA model: (a) unloaded, (b) center load, and (c) outer-load [2]

The results of the FEA are shown in figure 4. The figure shows the amount of mode I and mode II SERR that cause crack propagation for a given crack length. It was expected that after the crack passed beyond the fastener, the mode I component would be eliminated by the clamping effect of the fastener and crack propagation would become pure mode II. This is not true for the center-load configuration; crack propagation is mixed-mode. As the crack tip passes the fastener location, the clamping effect diminishes, and G_I increases, as the crack grows. This is because as the load is transferred through shear from the center to outer laminates at the crack tip, a moment is induced to maintain equilibrium. This is an opening moment at the crack tip, and results in a mode I component. This means that a three-beam, center-loaded specimen fails to provide a pure mode II crack propagation across its length.

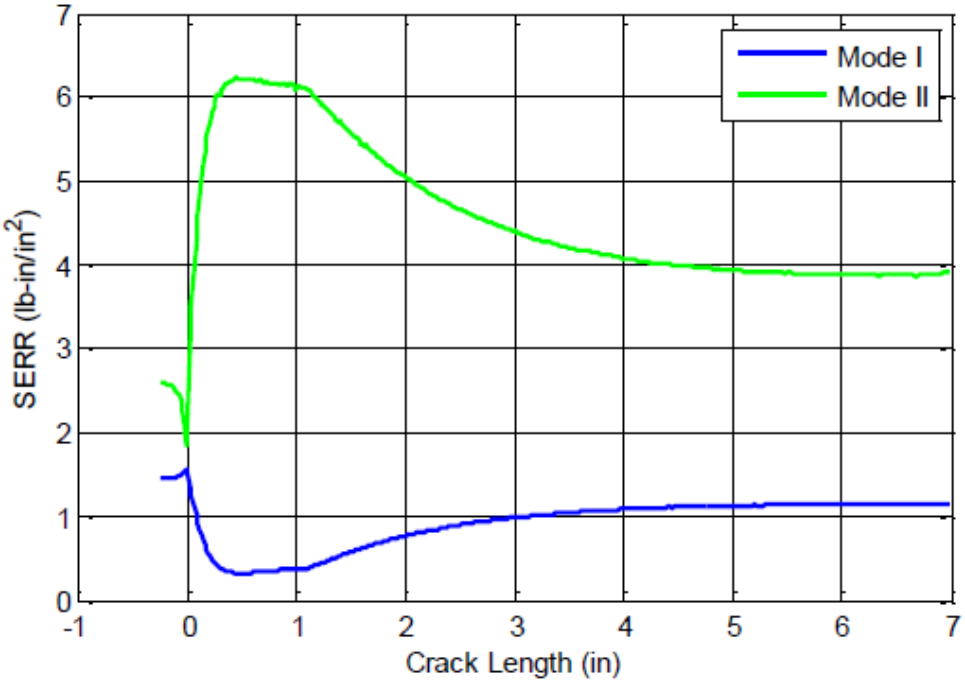

(a) SERR components for center-load

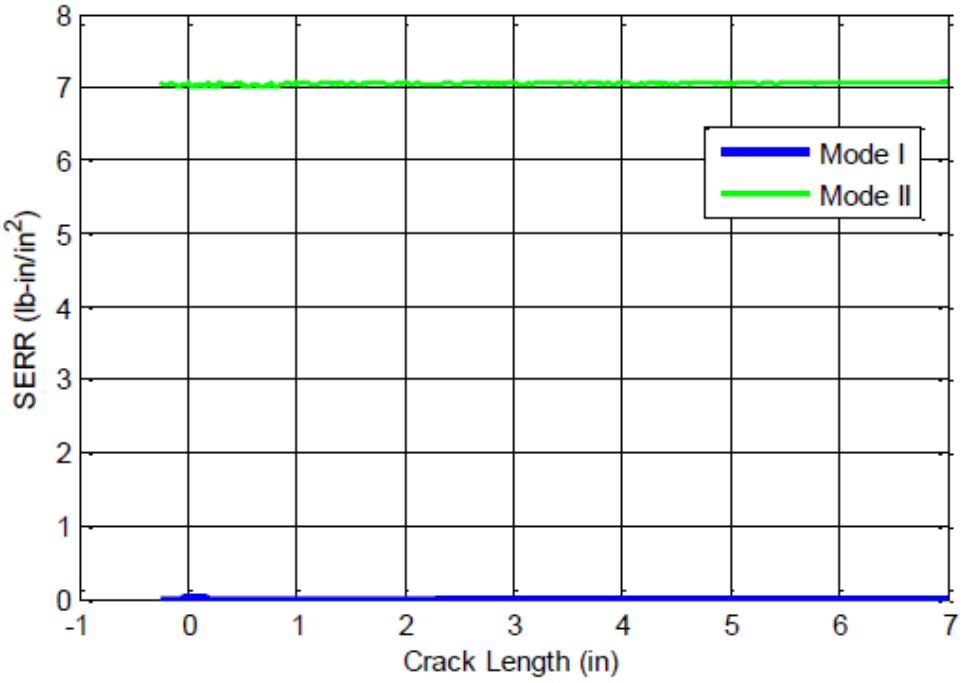

(b) SERR component for outer-load

Figure 4. SERR vs. crack length past fastener for center load (a) and outer load (b) [2]

For the outer-load configuration, the results show that crack propagation is entirely mode II on both sides of the fastener. This is because the load is transferred through shear from the outer laminates to the center laminate at the crack tip. A bending moment is induced to maintain equilibrium. This is a closing moment at the crack tip that forces mode I crack propagation to zero. The outer-load configuration is pure mode II, which is independent of the fastener clamping force and results strictly from the closing moment induced at the crack tip. This can be seen in figure 4(b) because crack propagation is pure mode II before reaching the fastener.

Based on the FEA results, it was determined that the three-beam outer-load specimen would be used to conduct the crack arrestment experiments. This allowed a consistent, pure mode II delamination throughout the length of the specimen while still allowing for easy fastener installation and testing using an axial load frame.

2.1.2 Specimen Configuration

The specimen configuration was driven by input from Boeing and FEA modeling to determine a design that would give pure mode II crack tip forces when a tensile load was applied. One of the primary reasons for using an axially loaded specimen was the ability to install arrest features in the system and have sufficient distance for the crack to grow during the test. A symmetric sample was required to achieve pure mode II, and this resulted in twin crack tips. It was assumed that the cracks would propagate symmetrically, as the driving force would be higher on the shorter crack.

The goal in designing the test specimen was to use laminates and a fastener representative of those used in actual structures. Because the goal of this experiment was to study crack arrestment capability of a fastener, the specimen used a design that allowed the crack to propagate more easily. The specimen was designed to use three 24-ply quasi-isotropic laminates bonded together, and a .25-inch diameter titanium fastener. The exact dimension of the specimen and an image of an actual specimen are shown in figure 5.

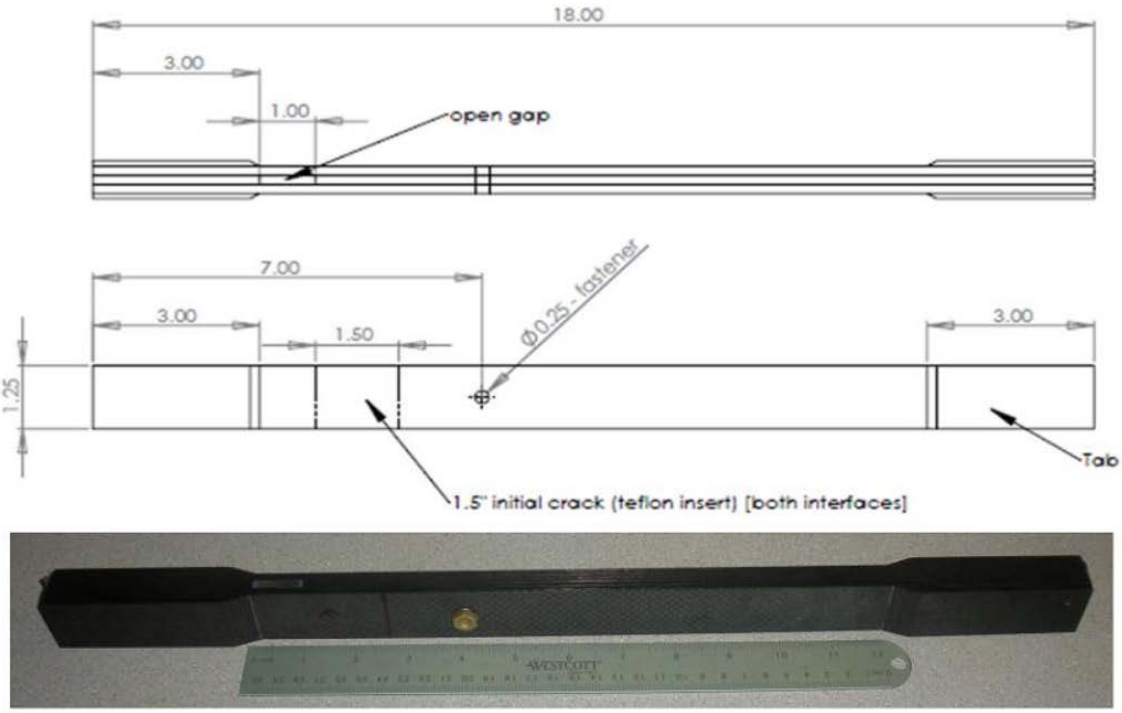

Figure 5. Three-plate specimen [2]

The specimen had a total length of 18.0 inches. The specimen width was 1.25 inches, which was chosen as 5 times the diameter of the fastener. There were 3.0-inch tabs at each end for clamping in to the tensile test machine. There was a 1.0-inch open gap at one end that provided the outer-loading required to achieve pure mode II crack propagation. Next to the open gap at a length of 1.50 inches were Teflon^{TM} tabs inserted between the laminates to provide initial cracks. The fastener was placed 1.5 inches from the crack tip, so that the stress concentrations at the hole did not affect crack initiation.

During testing, the specimen was loaded in tension and cracks initiated from the implanted crack tip at each bond interface. The cracks then propagated unarrested to the fastener, where the ability of the fastener to arrest and stabilize crack growth could be observed.

2.1.3 Experimental Procedure

Table 2 shows the test matrix for this experimental study. All the specimens were manufactured by Boeing, with exact details of the process not made available. A total of 18 specimens spanning 6 configurations was tested. The differences in specimen configurations were characterized by the bond type and plies at the crack interface. The coupon identification code was based on bond type, interface plies, and number. For example, SB-0/90fab-2 was secondary bonded with [0/90] fabric plies at the bond interface and was sample number 2. A fastener torque of 0 inch-lb (finger tight) was tightened just until the fastener could not be rotated by hand in the hole.

Table 2. Test matrix [2]

Coupon ID	Bond Type	Interface Plies	Fastener Torque
SB-0/90Fab-1	Secondary Bond	[0/90]/[0/90] fabric	40 in-lb
SB-0/90Fab-2	Secondary Bond	[0/90]/[0/90] fabric	40 in-lb
SB-0/90Fab-3	Secondary Bond	[0/90]/[0/90] fabric	40 in-lb
SB-0/90Fab-4	Secondary Bond	[0/90]/[0/90] fabric	40 in-lb
SB-0/90Fab-5	Secondary Bond	[0/90]/[0/90] fabric	40 in-lb
SB-0/90Fab-6	Secondary Bond	[0/90]/[0/90] fabric	40 in-lb
SB-0/90Fab-7	Secondary Bond	[0/90]/[0/90] fabric	40 in-lb
SB-0/90Fab-8	Secondary Bond	[0/90]/[0/90] fabric	No fastener
SB-0/0-1	Secondary Bond	0/0	0 in-lb (finger tight)
SB-0/0-2	Secondary Bond	0/0	0 in-lb (finger tight)
CC-0/0-1	Co-Cured	0/0	40 in-lb
CC-0/0-2	Co-Cured	0/0	40 in-lb
CC-0/0-3	Co-Cured	0/0	40 in-lb
CC-0/0-4	Co-Cured	0/0	40 in-lb
CC-$\pm$45-1	Co-Cured	+45/-45	0 in-lb (finger tight)
MB1-0/90Fab-1	Modified Bond 1	[0/90]/[0/90] fabric	0 in-lb (finger tight)
MB1-0/90Fab-2	Modified Bond 1	[0/90]/[0/90] fabric	40 in-lb
MB2-0/90Fab-1	Modified Bond 2	[0/90]/[0/90] fabric	0 in-lb (finger tight)

Each specimen had a strain gauge (Micro-Measurements EA-06-125AC-350) installed on the outside of one of the outer laminates 4.0 inches from the fastener within the initial cracked region. All stress values determined from the strain measurements were considered to be “nominal stress.” To determine the location of the crack, one side of the specimen was spray painted white and marked with black lines spaced at 0.125 inches near the location of the fastener and spaced at 0.25 inches farther away from the fastener. After strain gauge installation and markings, the fastener was installed to the required torque. Figure 6 shows an example of the location of the strain gauge and an image of the markings on the side of another specimen.

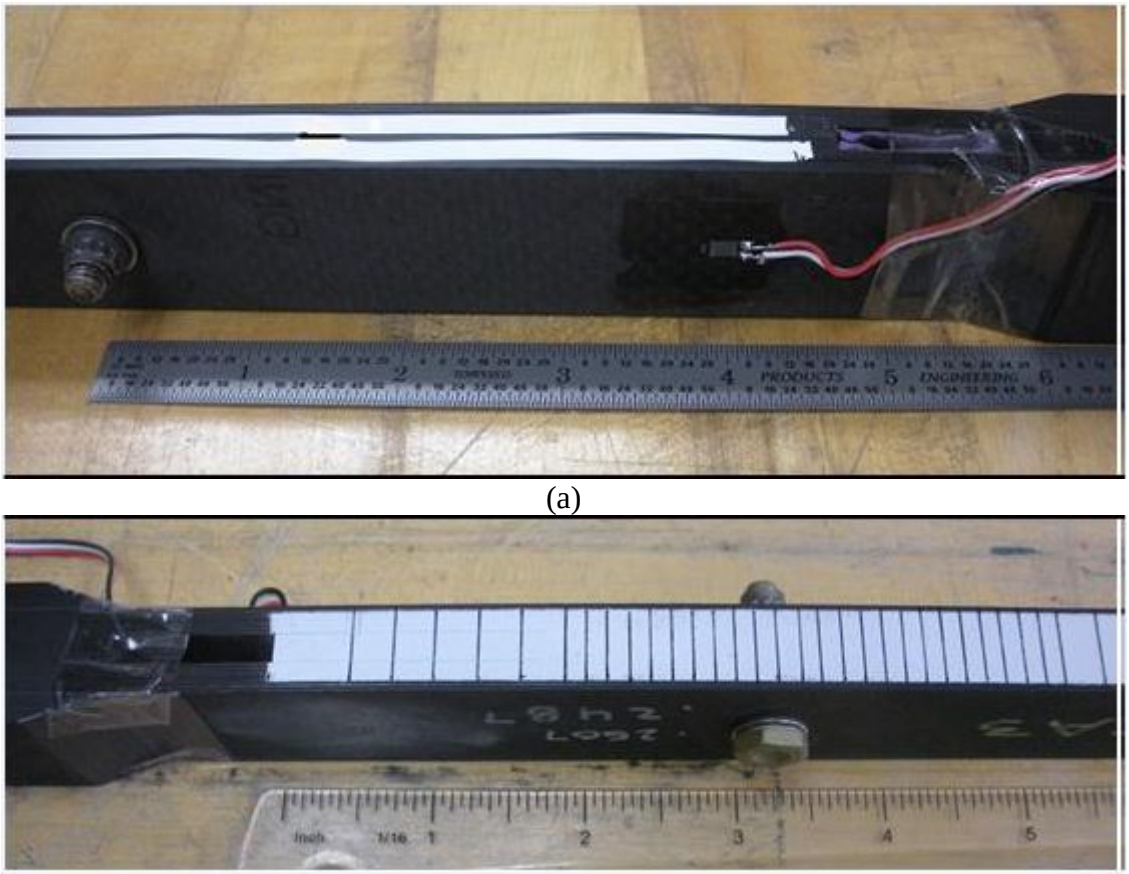

(a)

(b)

Figure 6. (a) Strain gauge location and (b) crack location markings [2]

Loading was performed at The University of Washington on an Instron® static load frame, with a displacement rate of 0.20 inches/minute. As the crack propagated, the load was read from the computer and recorded.

2.1.4 Experimental Results

The results of the secondary bonded specimens are summarized in table 3. Of particular note, none of the samples exhibited crack propagation, even when a fastener was not present. This indicated that the design was too strong in mode II delamination compared to its tensile strength; therefore, the fastener was not providing any benefit because the laminate did not require crack-arrest features to prevent crack growth.

Table 3. Secondary-bonded specimen results [2]

Coupon ID	Fastener Torque	Nominal Stress at Crack Initiation	Failure Mode and Failure Stress	Observed Crack Location at Failure
SB-0/90Fab-1	40 in-lb	78.9 ksi	FHT (78.9 ksi)	NA
SB-0/90Fab-2	40 in-lb	81.4 ksi	FHT (81.4 ksi)	NA
SB-0/90Fab-3	40 in-lb	82.2 ksi	FHT (82.2 ksi)	NA
SB-0/90Fab-4	40 in-lb	81.8 ksi	FHT (81.8 ksi)	NA
SB-0/90Fab-5	40 in-lb	77.8 ksi	FHT (77.8 ksi)	NA
SB-0/90Fab-6	40 in-lb	82.7 ksi	FHT (82.7 ksi)	NA
SB-0/90Fab-7	40 in-lb	80.5 ksi	FHT (80.5 ksi)	NA
SB-0/90Fab-8	No fastener	79.8 ksi	OHT (79.8 ksi)	NA
SB-0/0-1	0 in-lb (finger tight)	79.8 ksi	FHT (79.8 ksi)	NA
SB-0/0-2	0 in-lb (finger tight)	80.9 ksi	FHT (80.9 ksi)	NA

FHT = Filled-hole tension failure, OHT = Open-hole tension failure, NA = No crack observed before failure

The results of the co-cured specimens are summarized in table 4. The co-cured samples did experience crack propagation, albeit small amounts. For the 0/0 interfaced specimens, the crack remained within the interface. However, for the ± 45 specimen, the crack initiated within the implanted crack interface and propagated noncohesively, jumping plies into the outer laminate and propagating within the 90/45 interface, suggesting that the interface ply combination of ± 45 was stronger than others within the laminate.

Table 4. Co-cured specimen results [2]

Coupon ID	Fastener Torque	Nominal Stress at Crack Initiation	Failure Mode and Failure Stress	Observed Crack Location at Failure
CC-0/0-1	40 in-lb	45.8 ksi	FHT (67.6 ksi)	0.5 in past fastener
CC-0/0-2	40 in-lb	43.1 ksi	FHT (66.0 ksi)	0.5 in past fastener
CC-0/0-3	40 in-lb	47.1 ksi	Stopped before failure	0.5 in past fastener
CC-0/0-4	40 in-lb	54.0 ksi	Stopped before failure	0.5 in past fastener
CC-$\pm$45-1	0 in-lb (finger tight)	62.0 ksi	FHT (61.8 ksi)	NA

The test results for the modified bond specimens are summarized in table 5. Modifications to the bond were not described by Boeing. The cracks propagated cohesively, remaining in the interface, but did not propagate symmetrically. For specimen MB1-0/90Fab-1, the crack reached 3.5 inches

past the fastener on one interface and 5.0 inches past on the other. For MB1-0/90Fab-2, the cracks reached 4.75 inches and 6.125 inches past the fastener along the two different interfaces.

Table 5. Modified bond specimen results [2]

Coupon ID	Fastener Torque	Nominal Stress at Crack Initiation	Failure Mode and Failure Stress	Observed Crack Location at Failure
MB1-0/90Fab-1	40 in-lb	70.0 ksi	FHT (65.6 ksi)	3.5 and 5.0 in past fastener
MB1-0/90Fab-2	Finger tight	68.4 ksi	FHT (68.7 ksi)	4.75 and 6.125 in past fastener
MB2-0/90Fab-1	Finger tight	93.8 ksi	FHT (93.8 ksi)	NA

2.1.5 Measured Laminate Properties

The effective laminate modulus of elasticity in the *x*-direction, E_x, was determined for each specimen configuration from measured load and strain data. Figure 7 shows a comparison of the typical plots for nominal stress versus measured strain for each configuration tested. The values of E_x were determined by dividing the nominal stress by the measured strain and averaging over the linear range of the stress-strain curve. The nominal stress was calculated from the measured load-frame force divided by the nominal cross-section area. Strain was measured by strain gauges. [2]

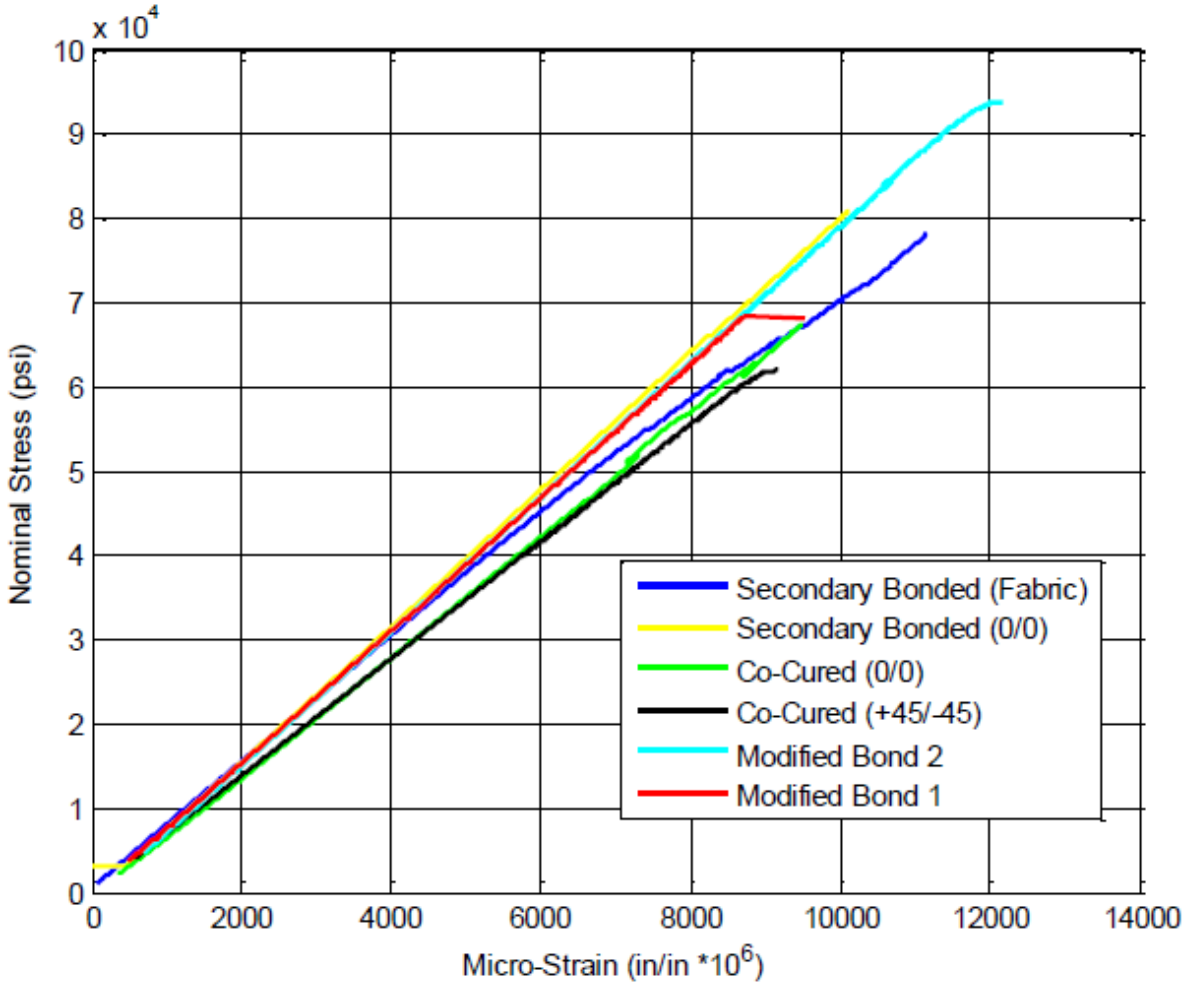

Figure 7. Typical plots for nominal stress vs. measured strain [2]

Table 6 summarizes measured E_x for all configurations. As expected, the values of the tensile stiffness fall relatively close to one another. The co-cured structure appears to have a slightly lower value of E_X, but the reasons for this were not investigated.

Table 6. Summary of E_x for all specimen configurations [2]

Specimen Configuration	Measured E_x
Secondary Bonded [0/90] fabric interface	7.44 Msi
Secondary Bonded 0/0 interface	7.43 Msi
Co-Cured 0/0 interface	6.88 Msi
Co-Cured 0/0 interface	6.92 Msi
Modified Bond 1	7.72 Msi
Modified Bond 1	7.82 Msi

2.2 MIXED-MODE SPECIMEN [3]

The literature is rich in test designs and practices related to interlaminar fracture testing, but there is a relative paucity of tests done on arrest mechanisms. The ASTM has established standards for determining both mode I and mixed mode I-mode II interlaminar fracture toughness. The DCBs is a long-established specimen for determining the mode I critical energy release rate, G_{IC}. The mixed-mode bending test enables the measurement of the interlaminar fracture toughness with any mode I and mode II mix ratio. There is currently no standard for testing pure mode II interlaminar fracture toughness. ENF is the proposed standard and most widely used for measuring G_{IIC}. The four-point bend end-notched flexure (4ENF) is also pursued as a test method for G_{IIC} because constant moment is applied to the crack tip during propagation. These specimens have been adapted to measure the crack arresting capabilities of implementations such as z-pins.

However, the mode II test configurations could not be adapted to work with a delamination arrest fastener in mode II testing. This was because the mode II test configurations rely on bending to generate interlaminar shear to drive mode II crack propagation. These specimens were required to be compact (i.e., short and thick) to avoid large nonlinear bending deformation. For example, the typical ENF specimen dimensions were approximately 100–150 mm (4–6 inches) in length, and 3–8 mm (0.1–0.3 inches) in thickness. The active crack growth area was only a fraction of the specimen length. For typical fastener sizes ranging from 3–9.5 mm (0.125–0.375 inches) in diameter, the required specimen area for fastener installation and for demonstration of delamination arrest behavior would make specimen design impractical. In other words, the overall length of the specimen had to be increased to provide sufficient crack growth area, making the specimen become unrealistically thick. Also, the control over laminate thickness and layup, which is an important parameter in fastener joint design, would be lost.

In an attempt to produce an axially loaded mode II test specimen, a symmetric three-plate, two-crack design was tested (figure 5). The symmetric design allowed the moment generated at the crack tip to be reacted by the center plate, eliminating the mode I fracture component and out-of-plane bending. The concept also led to a simple analysis method. However, the crack driving force was lower because the applied load was shared by two crack tips. Provided the material properties of commonly used aerospace composite material systems (e.g., filled-hole tension failure at approximately 10,000 με and G_{IIC} at approximately 10 in-lb/in^2), it was found that for a 72-ply specimen (three plates × 24 ply each), laminate failure would occur before the crack could propagate past the fastener. In addition, there was no guarantee that the two cracks would propagate in synchrony, nullifying the benefits of having a symmetric design.

The hybrid bolted-bonded joint, originally presented as a fail-safe concept by Hart-Smith [15] and later tested by Kelly [16], came close to meeting all the requirements for the research. A novel test specimen was devised by modifying a bolted-bonded single-lap joint specimen into a crack propagation specimen (figure 8). Rapid analysis and data reduction of such test were enabled by the beam-column analytical method developed. The details of the design are discussed in the following sections.

2.2.1 Specimen Configuration

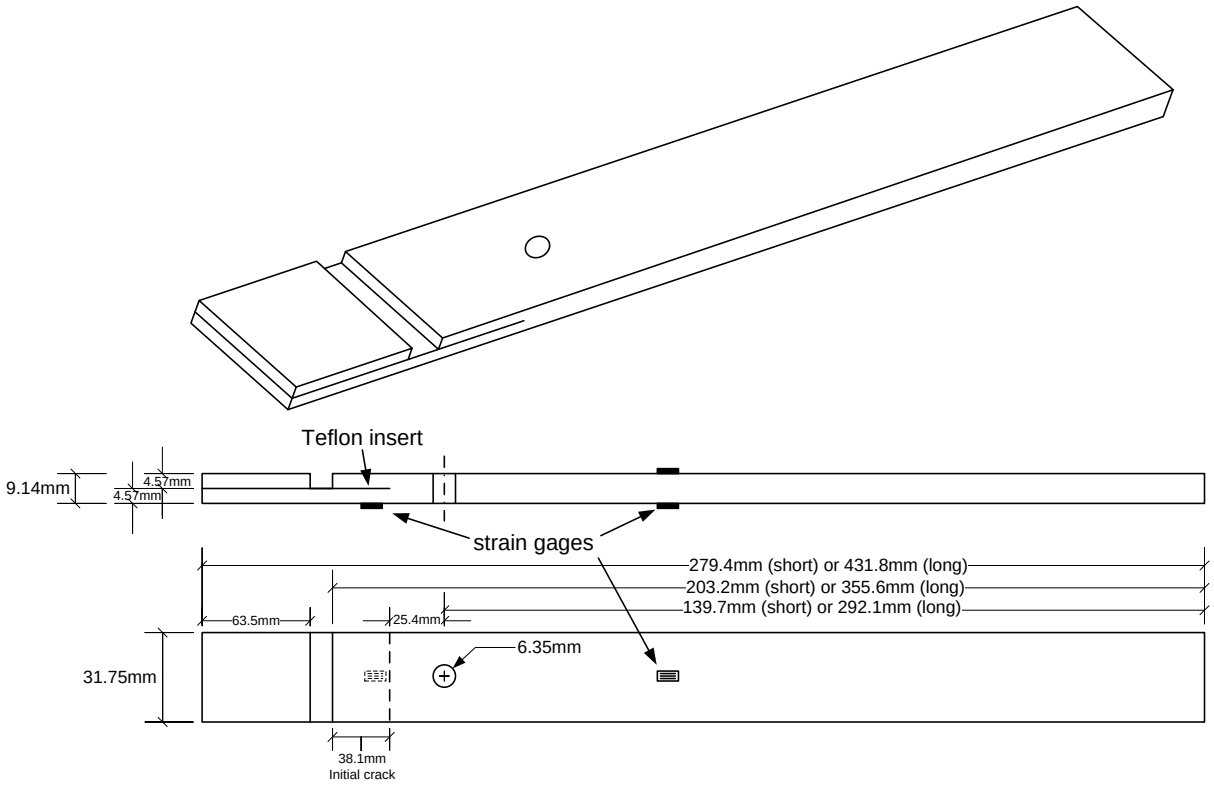

Figure 8. Drawing of the tension crack arrest test specimen (not to scale) [3]

The design of the delamination arrest specimen is shown in figure 8. The axially loaded specimen consisted of laminate with an initial through-width delamination, partially splitting the specimen into two sublaminates. One sublaminate was trimmed during layup, forming a notch. The initial crack measured 38.1 mm (1.5 inches) from the end of the notch, or 25.4 mm (1.0 inch) from the center of the fastener hole, and was formed by a Teflon film insert. Tension load was applied to the longer, untrimmed sublaminate. A tab was recommended to be added to the loaded sublaminate to eliminate the offset and the associated bending while placed in the test machine grip. A fastener was installed ahead of the crack, such that the fastener was not loaded at the beginning of the test. Two different specimen lengths were manufactured, 279.4 mm (11 inches) and 431.8 mm (17 inches). The specimens needed to be extraordinarily long to provide area for crack initial propagation, arrest, and retarded propagation. The specimen width was 31.75mm (1.25 inches), corresponding to a width of 5D using fasteners 6.35 mm (0.25 inches) in diameter.

Two 24-ply sublaminate layups were chosen for this study: a quasi-isotropic layup $(0/45/90/-45)_{3S}$ and a layup with 50% 0° plies $(0/-45/0_2/90/45/0_2/-45/90/-45/0)_S$. Two identical sublaminates were combined, with an initial crack, to form the 48-ply specimen. The use of symmetric and balanced layups eliminated curvature due to thermal stresses from curing and coupled bending under axial load. In addition, 0° plies with +/-5° offsets were used to bound the crack interface to avoid fiber bridging or cracking through the bounding lamina. The material system used was T800S/3900-2

pre-preg tape (Toray). The specimens had a nominal thickness of 9.144 mm (0.36 inches), using a reference ply thickness of 0.1905 mm (0.0075 inches).

Four panels 304.8 mm (12 inches) in width were prepared for curing. The first set of two panels (one with quasi-isotropic layup and one with 50% 0°) were 304.8 mm (12 inches) in length and were vacuum bagged and cured in an autoclave. Because of the unusually thick layup, the cured panels had nonuniform thickness, resulting in a dome shape. Also, bow waves were visible at the notch location. In an attempt to resolve the above issues, the second set of two panels, 457.2 mm (18inches) in length, were cured using a heat press. However, the panels cured using the heat press experienced a significant amount of ply migration (ply sliding and rotating). This was likely due to the low temperature ramp rate produced by the heat press, which was below the commanded parameter. Both sets of panels were used in the experiments, with no detectable difference in the experimental results.

The cured panels were cut to 31.75 mm (1.25 inches) wide specimens using a water-jet machine. Each panel yielded seven to eight specimens. The cutting also trimmed away 25.4 mm (1.0 inch) from the length of each panel.

A 6.35-mm (0.25-inch) diameter hole was drilled 38.1 mm (1.5 inches) from the notch at the midline of each specimen (figure 9). The hole was drilled with a milling machine using a conventional two-flute, carbide-tipped drill bit. The specimen was backed by an aluminum block to prevent exit damage, whereas the entry side was unprotected. The resulting holes were of high quality with no visible damage on the surface plies of the specimen or at the edge of the bore. A 6.35-mm (0.25-inch) diameter titanium fastener was installed with two 12.3-mm (0.48-inch) diameter washers on both sides of the hole (figure 10). Various levels of fastener installation torque, from finger-tight (no detectable slack of the fastener in the hole) to full installation torque of 9.04 N-m (80 in-lb), were used to generate various amounts of crack face friction. However, it should be noted that using bolt torque to control preload is associated with high uncertainty and can produce wide scatter in friction forces.

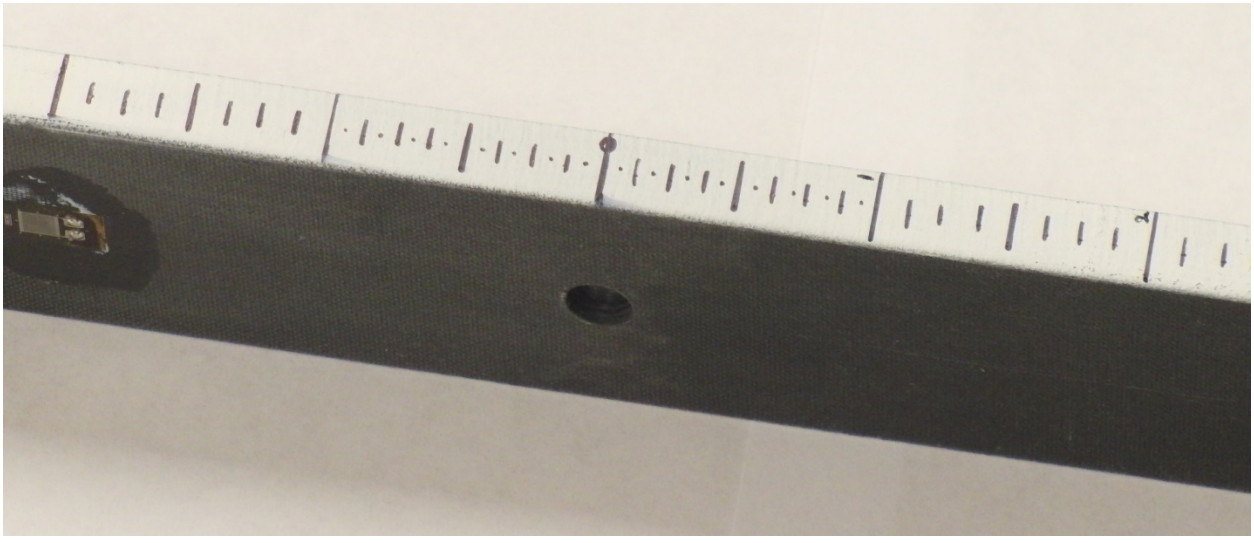

Figure 9. Specimen with drilled hole and painted scale (inches) on the edge [3]

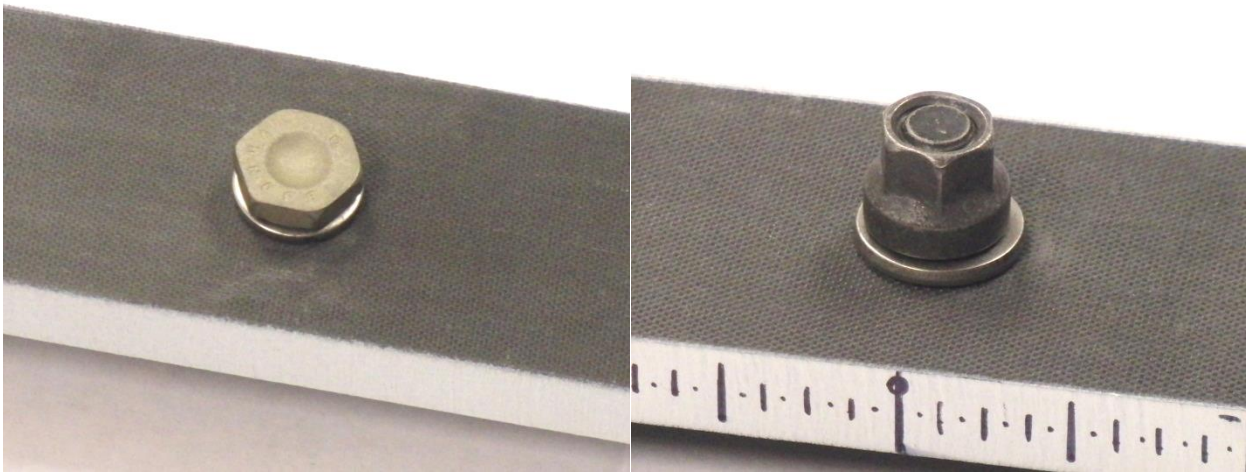

Figure 10. Specimen with fastener installed: (a) fastener head side and (b) fastener collar side [3]

Back-to-back strain gauge pairs were installed 63.5 mm (2.5 inches) and 127 mm (5 inches) from the hole in the shorter (279.4-mm/11-inch) and longer (431.8-mm/17-inch) specimens, respectively. The strain gauges were used to measure the axial and bending strains in the specimen. In some of the longer specimens, one strain gauge was installed 50.8 mm (2 inches) away from the hole on the notch side of the longer sublaminate. These strain gauges measured the surface strain of sublaminate at ultimate failure. To measure crack propagation, the specimens were painted with a thin layer of white spray paint on the edge of the specimen. Scales of 3.175-mm (0.125-inch) intervals were drawn on the edge for visual tracking of the crack tip. The scales were reduced by half near the fastener to provide higher resolution tracking (figures 11 and 12). Visual access to the other side of the specimen was unavailable because of the physical constraints of the test lab.

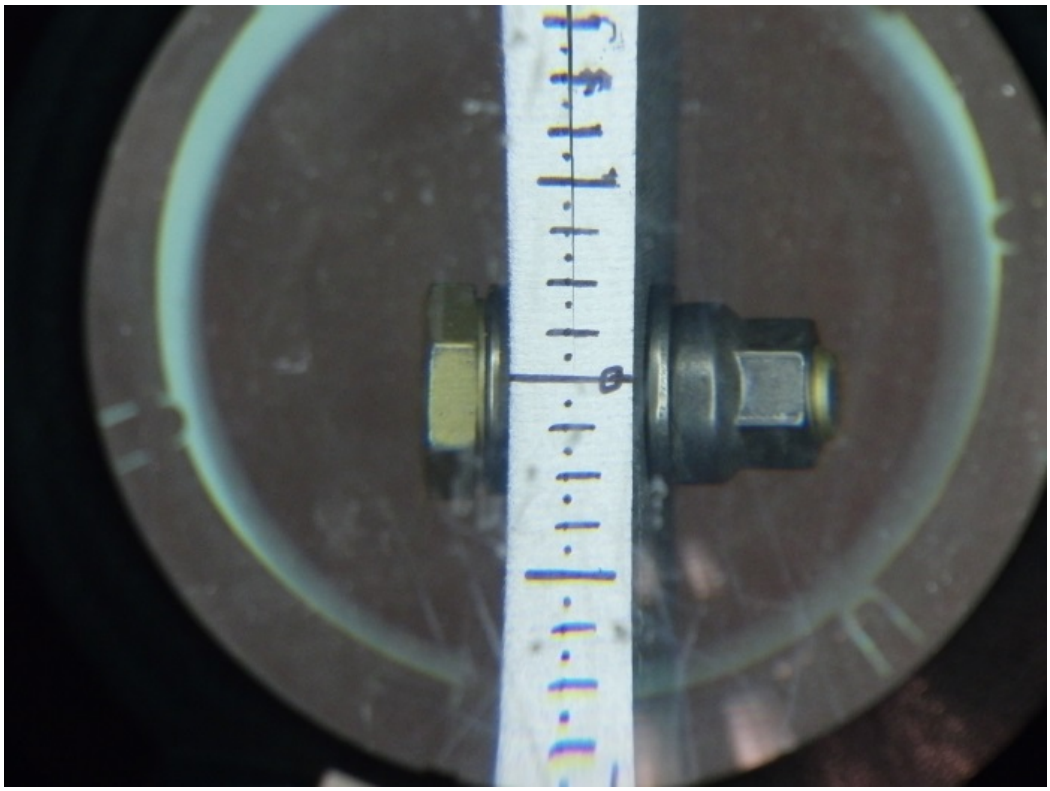

Figure 11. Visual tracking of crack-tip location—crack arrested at the fastener [3]

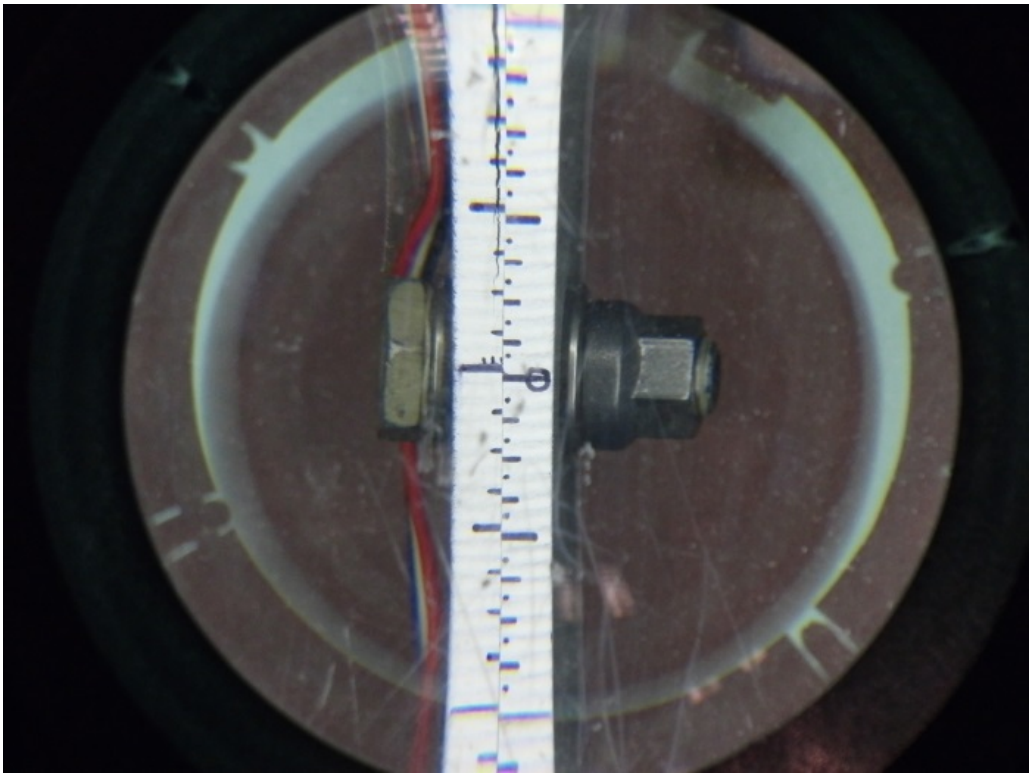

Figure 12. Visual tracking of crack-tip location—propagated past the fastener [3]

Specimens were placed into a displacement-controlled tension testing machine (Instron 5585H[1]) for testing (figure 13). Wedge-type grips were used to hold the specimens in the machine. The sublaminate with the notched end was placed into the upper grip with the laminated tab. The tab was used to reduce the amount of bending that would otherwise result from the grip pushing the 24-ply sublaminate to the midplane of the 48-ply specimen. (A few specimens were initially tested without the tab, which resulted in early laminate failure at the grip location. However, use of the tab made no appreciable difference in crack-propagation behavior.) Extension displacement was applied at a rate of 1.0 mm/min (0.039 inches/min) during ramp up and 0.5 mm/min (0.020 inches/min) during crack propagation. The slow displacement rate was used to allow real-time manual tracking of the crack propagation. The crack-extension data, crack-tip location, and applied load were collected every time crack propagation was detected along the scale painted on the edge of the specimen. During stable crack propagation, each time the crack extended and stopped, the new crack-tip location and the applied load that triggered extension were recorded as a data point. If crack propagation was momentarily unstable but stopped later (crack tip jumping large distances), only one data point would be collected at the final crack location.

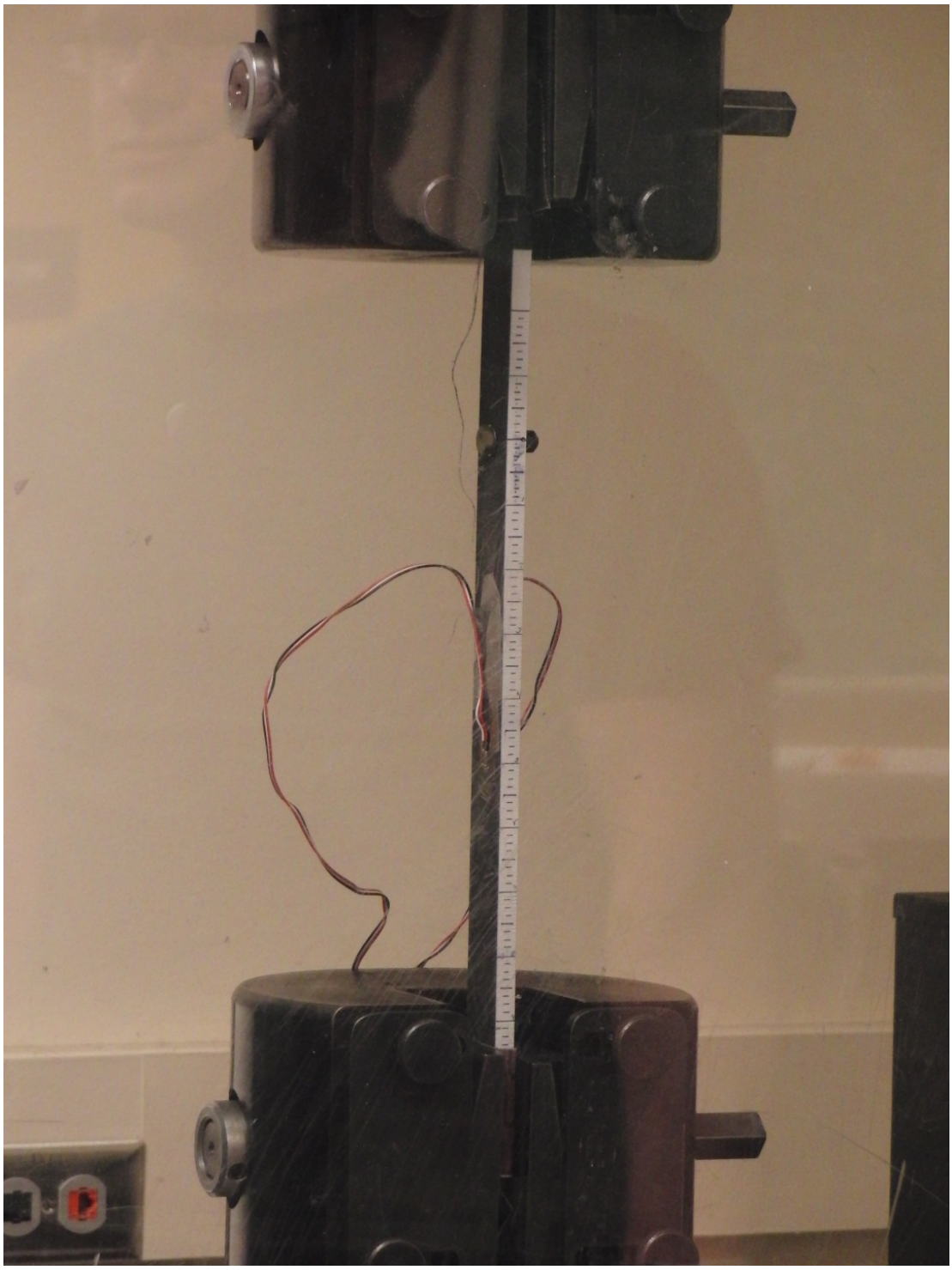

Figure 13. Specimen being loaded in the Instron 5585H test machine [3]

2.2.2 Experimental Results

Thirty specimens from four different panels were tested. Two panels were short (279.4 mm/11 inches) and two were long (431.8 mm/17 inches). One short panel and one long panel had quasi-isotropic layup, whereas the other two had 50% 0° layup. A summary of the tested configurations, ultimate failure loads, and nominal axial elastic moduli is provided in table 7. Specimens denoted by an asterisk (short panel Q1, Q3, Q5, Q7) were tested first without a tab at the upper grip to balance the thickness offset. While no detrimental effect was observed in regard to the crack-propagation behavior, the final failure mode was laminate fracture at the grip, which was undesirable.

Table 7. Summary of test final failure loads [3]

Panel	ID	Fastener Torque (N-m / in-lb)		Ultimate Load (kN / kips)		Nominal Axial Elastic Modulus - Ex (GPa / msi)		Remarks
Short Panel (Vacuum Bag in Autoclave) Quasi-isotropic	Q5*	Finger tight		60.5	13.6	52.2	7.57	Failed at the grip
	Q7*	Finger tight		60.4	13.6	51.6	7.48	Failed at the grip
	Q2	2.42	21.4	77.7	17.5	52.1	7.56	Filled-hole tension
	Q4	2.42	21.4	-	-	-	-	Stopped before failure
	Q6	2.42	21.4	67.7	15.2	54.2	7.86	Filled-hole tension
	Q1*	5.31	47.0	70.6	15.9	53.2	7.71	Failed at the grip
	Q3*	5.31	47.0	68.2	15.3	52.5	7.61	Filled-hole tension
Short Panel (Vacuum Bag in Autoclave) 50% 0°	S2	Finger tight		71.9	16.2	81.6	11.83	Failed at the grip
	S8	Finger tight		65.2	14.7	-	-	Failed at the grip
	S5	2.37	21.0	77.7	17.5	82.8	12.01	Filled-hole tension
	S7	2.37	21.0	77.6	17.4	84.3	12.22	Filled-hole tension
	S1	5.65	50.0	76.4	17.2	75.8	11.00	Filled-hole tension
	S3	5.65	50.0	78.5	17.6	82.5	11.96	Filled-hole tension
	S4	9.04	80.0	84.0	18.9	80.5	11.67	Failed at the grip
	S6	9.04	80.0	80.0	18.0	82.6	11.98	Filled-hole tension
Long Panel (Heat Press) Quasi-isotropic	Q1	Finger tight		72.0	16.2	-	-	Filled-hole tension
	Q2	Finger tight		71.6	16.1	50.7	7.35	Filled-hole tension
	Q3	2.26	20.0	68.8	15.5	-	-	Filled-hole tension
	Q4	2.26	20.0	74.1	16.7	-	-	Filled-hole tension
	Q5	5.65	50.0	-	-	-	-	Stopped before failure
	Q6	5.65	50.0	72.1	16.2	50.9	7.38	Filled-hole tension
	Q7	9.04	80.0	-	-	-	-	Stopped before failure
	Q8	9.04	80.0	70.0	15.7	52.0	7.54	Filled-hole tension
Long Panel (Heat Press) 50% 0°	S1	Finger tight		100.3	22.5	-	-	Filled-hole tension
	S2	Finger tight		-	-	73.3	10.62	Stopped before failure
	S3	2.26	20.0	85.7	19.3	-	-	Filled-hole tension
	S4	2.26	20.0	86.6	19.5	72.1	10.45	Filled-hole tension
	S5	5.65	50.0	93.4	21.0	-	-	Filled-hole tension
	S6	5.65	50.0	90.5	20.3	73.4	10.65	Filled-hole tension
	S7	9.04	80.0	91.0	20.5	72.8	10.57	Filled-hole tension

All subsequent tests were conducted with a tab to prevent laminate failure at the grip and to move the failure location to the fastener hole (figures 14 and 15). "Finger-tight" fastener torque was the minimum tightness applied such that there could be no free movement or rotation of the fastener in the hole. Finger tight was very close to zero torque. In the specimens from the short panel with quasi-isotropic layup, the fasteners were installed with a conventional wrench with controlled force applied at a fixed moment arm. A click-type torque wrench (range: 2.26-22.6N-m /20-200 inches-lb +/- 4%) was used for all other specimens. The nominal elastic modulus was calculated using test loads, midplane strains derived from back-to-back strain gauges, and nominal specimen width (31.75 mm/1.25 inches) and thickness (9.144 mm/0.36 inches). It was notable that the nominal axial elastic moduli of the two panels cured using heat press were lower than that cured using vacuum bag in an autoclave. This was likely due to ply sliding and rotation during curing in the heat press, in which the temperature ramp rate was too low to prevent ply movements before glass transition. Missing entries in the table are due to either erroneous data from poor strain gauge installation or specimens not being gauged.

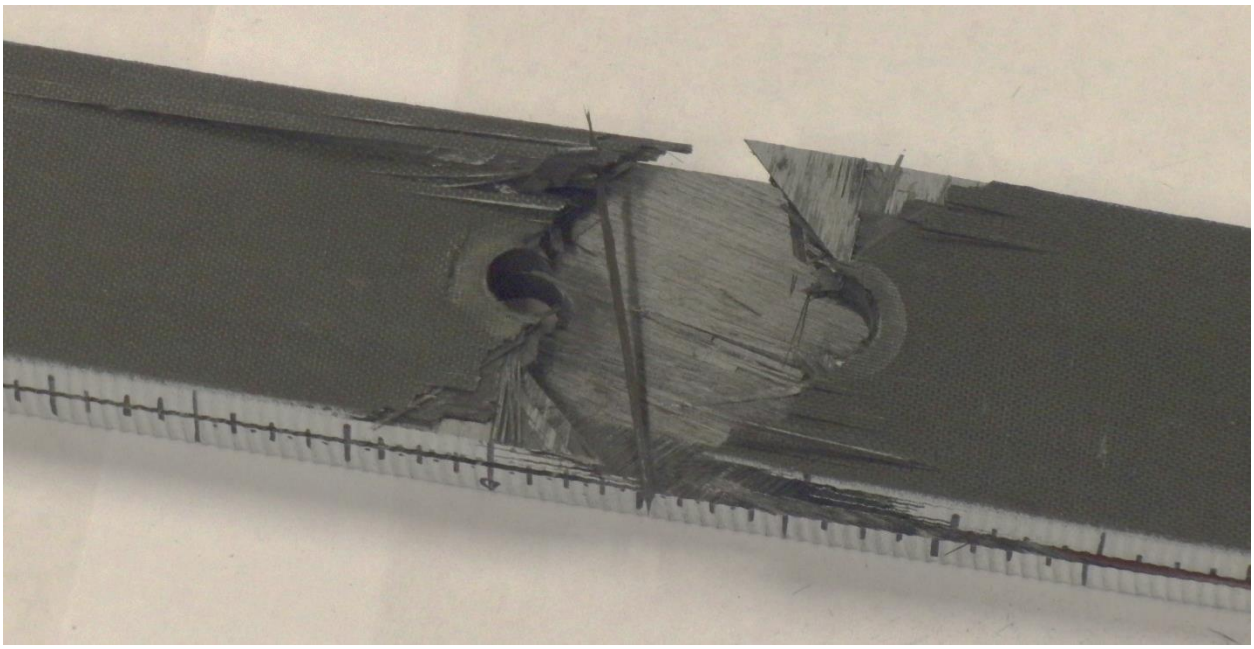

Figure 14. Specimen ultimate failure—filled-hole tension failure [3]

Figure 15. Specimen ultimate failure—filled-hole tension mixed with laminate delamination/splitting [3]

The results presented in this section focus primarily on crack-propagation behavior versus applied load of the test specimens. A technical discussion of the results and underlying mechanisms guiding the propagation behavior are subsequently discussed**.**

Figures 16–19 show the applied tension load versus crack-tip location results, grouped by panel lengths and layups. The tension load applied by the test machine was recorded every time a detectable crack-propagation event was observed, forming the data points in these figures. The *x*-axis shows the crack-tip location as measured from one side of the specimen, in which zero is at the center of the fastener. (For reference, the diameters of the fastener and the washers were 6.35 mm/0.25 inches and 12.7 mm/0.5 inches, respectively.) The crack propagated from negative to positive crack-tip location. The initial crack tip was at 25.4 mm (1.0 inch) for all specimens, which corresponded to 25.4 mm before reaching the fastener. For the short-panel specimens, the maximum crack-tip location was 127 mm (5.0 inches), which was the distance between the fastener and the test-machine grip. For the long-panel specimens, the maximum crack-tip location was 228.6 mm (9.0 inches). The *y*-axis shows the applied tension load. Solid lines in the figures correspond to stable crack propagation, in which incremental crack growth requires a corresponding increase in load. The horizontal dashed lines correspond to unstable crack propagation, in which the crack tip "jumped" long distances without any increase or a slight decrease in load (decrease in load was not recorded as part of the data because it could not be accurately and reliably captured in real time). All load versus crack tip location curves in these figures share a common characteristic. The crack propagation before the fastener was unstable, followed by a phase of arrested crack growth with a large increase in load in which the crack tip reached the fastener, ending in a long period of stable crack growth with relatively mild increase in load. For specimens with high stiffness or high fastener torque, there were often unstable crack jumps when the crack tip exited the fastener area.

For the specimens from the short panel with quasi-isotropic layup (figure 16), the first crack propagation from the initial flaw was unstable at an average load of 39.6kN (8.9 kips). The unstable propagation was arrested at approximately -6.35 mm (-0.25 inches). Large increases in applied load, proportional to fastener torque, were required to propagate the crack around the fastener. The steep slopes of the load versus crack tip location curves between -6.35 mm (-0.25 inches) and 12.7 mm (0.5 inches) demonstrate the highly effective arresting capability of the fastener. The finger-tight specimens (Q5, Q7) required an average of 55.9 kN (12.6 kips) to reach 12.7 mm (0.5 inches), whereas the highest torque specimens (Q1, Q3 at 5.31N-m/47in-lb) required an average of 64.7 kN (14.5 kips). At this crack-tip location, the fastener provided a 41%–63% additional load capability over the strength of the matrix itself. Between 12.7 mm (0.5 inches) and the end of test, crack propagation remained stable but required much smaller load increments, as shown by the shallow slope of the curves. In general, higher torque specimens required higher loads to reach any given crack-tip location. For example, at 50.8 mm (2.0 inches), the finger tight specimens were at 59.5 kN (13.4 kips), whereas the specimens with 2.42 N-m (21.4 in-lb) torque were at 65.8 kN (14.8kips). In the highest torque specimens, Q1 and Q3, unstable crack propagations were observed between 12.7 mm (0.5 inches) and 44.5 mm (1.75 inches). None of the specimens had a crack propagate to the grip, which was 127 mm (5.0 inches) from the fastener. Specimens Q1, Q5, and Q7 were tested without tabs, and the laminate failed at the grips at lower loads. The undesirable failure locations prompted the use of the tab to eliminate the offset in the grip, and therefore moved the failure location to the fastener and increased the failure loads of the specimens.

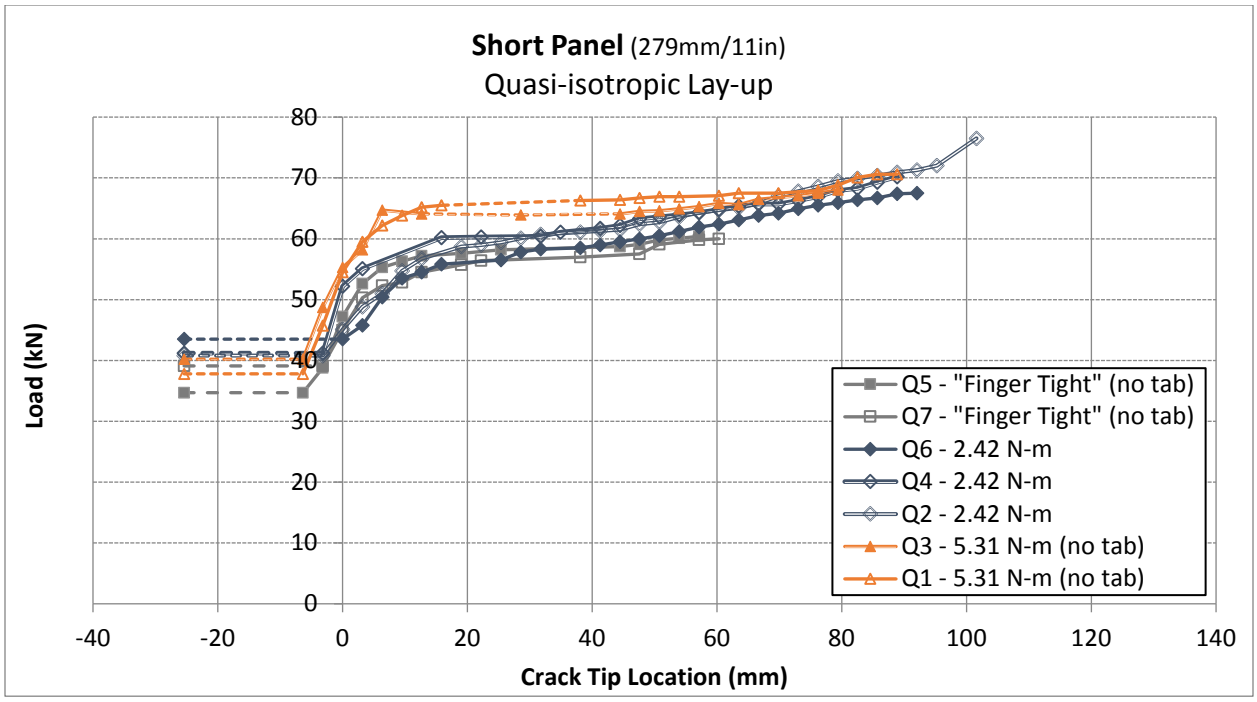

Figure 16. Applied load vs. crack-tip location—short panel (quasi-isotropic layup) [3]

For the specimens from the short panel with 50% 0° layup (figure 17), the first unstable crack propagation from the initial flaw occurred at an average load of 40.4kN (10.0 kips), essentially the same as that from the quasi-isotropic panel. The unstable propagation was arrested at approximately -6.35 mm (-0.25 inches). There was a weak trend for the higher torque specimens to arrest slightly earlier than the lower torque specimens. Large increases in applied load, proportional to fastener torque, were required to propagate the crack around the fastener. This arrested growth region extended to 19.05 mm (0.75 inches), slightly more than that of the quasi-isotropic specimens. The finger-tight specimens (S2, S8) required an average of 62.6 kN (14.1 kips) to reach 19.1 mm (0.75 inches), whereas the highest torque specimens (S4, S6 at 9.04N-m/80in-lb) required an average of 78.1 kN (17.6 kips). The fastener provided 55%–93% additional load capability, which was significantly greater than the improvements observed in quasi-isotropic specimens. All specimens experienced some unstable crack propagation when the crack tip exited the fastener area. The amount of unstable propagation was proportional to the fastener torque, from approximately 25 mm (1.0 inch) for finger-tight specimens up to 60 mm (2.5 inches) for the highest torque specimens. Following the unstable crack jumps, crack propagation remained marginally stable, requiring mild load increments to propagate the crack to the grip at 127 mm (5.0 inches). Similar to the quasi-isotropic specimens, higher torque specimens required higher loads to reach any given crack-tip location. Also, the highest torque specimens, S4 and S6, consistently recorded the longer unstable crack propagations, approximately 70 mm (2.75 inches), upon exiting the fastener location. All of the specimens had the crack tip reaching the grip at 127 mm (5.0 inches) before final failure because of the higher load-carrying capability of the stiffer layup.

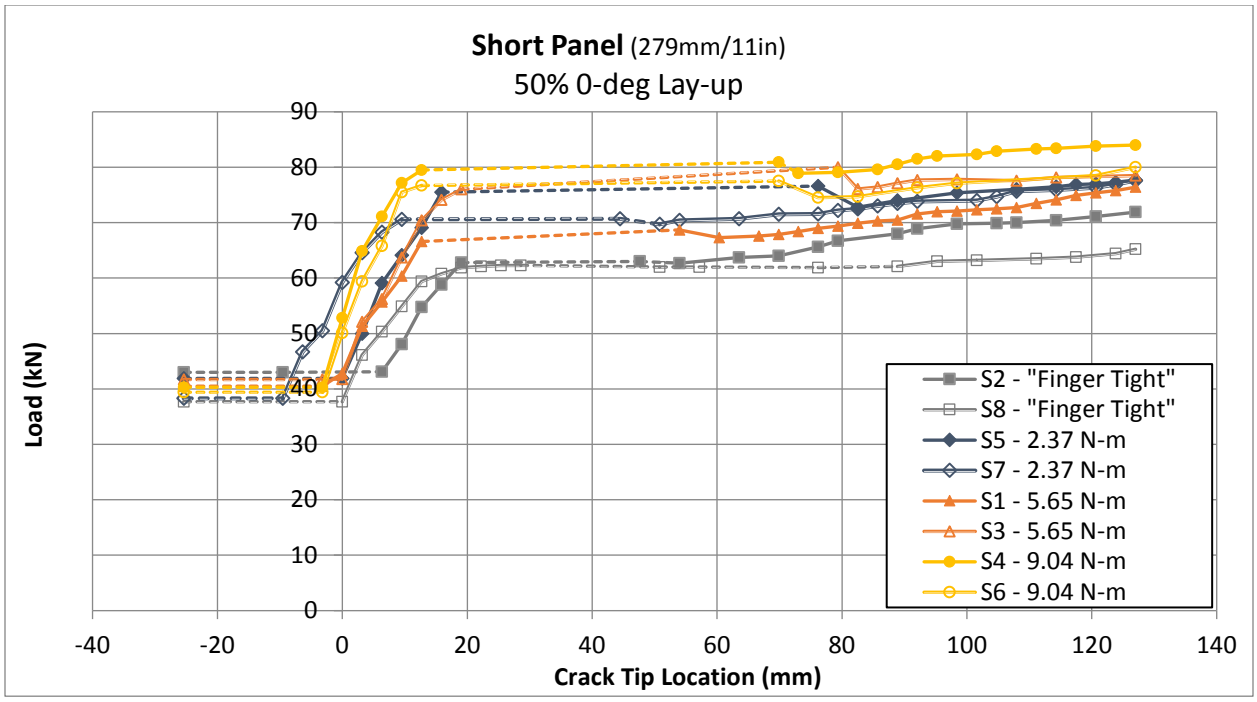

Figure 17. Applied load vs. crack tip location—short panel (50% 0-deg layup) [3]

For the specimens from the long panel with quasi-isotropic layup (figure 18), the first unstable crack propagation from the initial flaw occurred at an average load of 35.3kN (7.9kips). The unstable propagation was arrested at approximately -6.35 mm (-0.25 inches). Large increases in applied load, proportional to fastener torque, were required to propagate the crack around the fastener. The finger-tight specimens (Q1, Q2) required an average of 45.3kN (10.2kips) to reach 19.1 mm (0.75 inches), whereas the highest torque specimens (Q7, Q8 at 9.04N-m/80in-lb) required an average of 60.6kN (13.6kips). At this crack tip location, the fastener provided 28%–72% additional load capability over the strength of the matrix itself. Between 19.1 mm (0.75 inches) and end of test, crack propagation remained marginally stable, as shown by the shallow slope of the curves. The curves from different torques appeared to coalesce after the crack-tip location of 100 mm (4 inches). This phenomenon was not observed in the short-panel specimens. In the highest torque specimen, Q8, the most unstable crack propagations upon exiting the fastener location (approximately 60 mm/2.4 inches) were observed. All specimens except Q5 and Q7 were tested to ultimate failure. Q5 and Q7 tests were aborted when the specimen slipped out of the grip. None of the specimens were able to propagate the crack tip to the grip before ultimate failure. The long panel with quasi-isotropic layup generally recorded lower loads at any crack-tip location when compared to the short panel equivalent. This could be partly attributed to the change in manufacturing process from vacuum bag in autoclave to heat press. Curing in the heat press experienced a low heat rate across the thickness of the panel, resulting in ply sliding and rotation.

The effect of this could also be seen by the slightly lower axial stiffness in the specimens from the long panel (table 7).

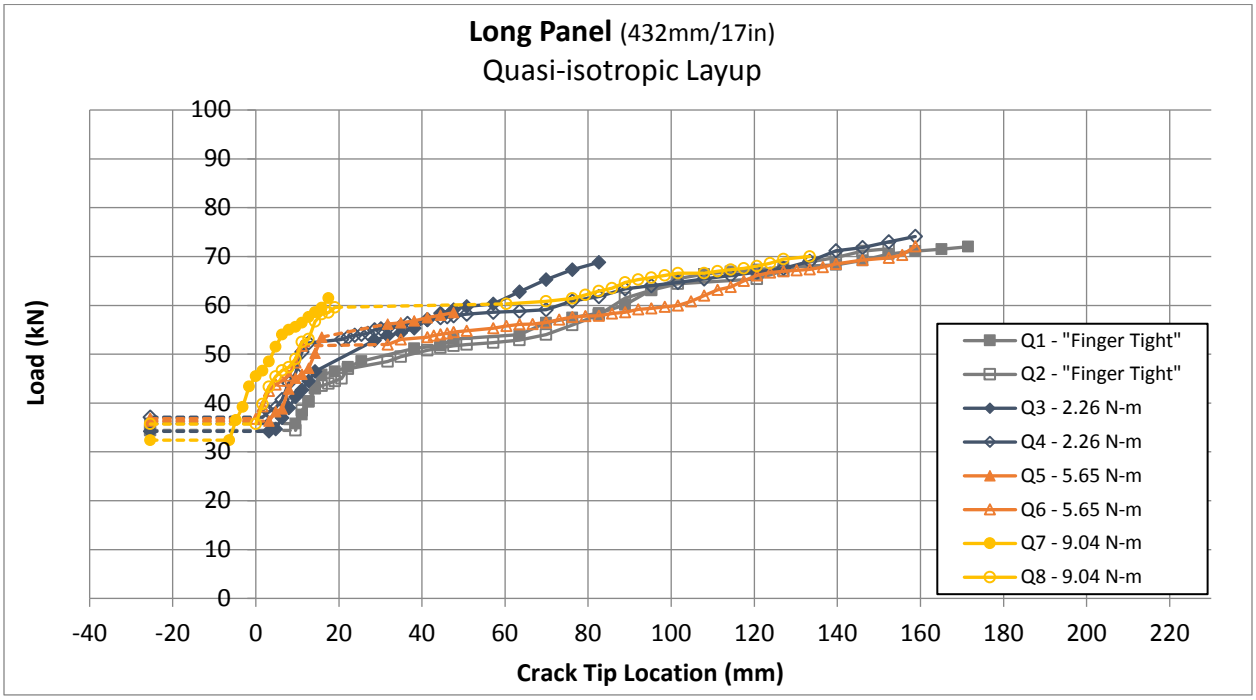

Figure 18. Applied load vs. crack-tip location—long panel (quasi-isotropic layup) [3]

For the specimens from the long panel with 50% 0° layup (figure 19), the first unstable crack propagation from the initial flaw occurred at an average load of 39.4kN (8.9 kips), but the scatter was unexpectedly large. The unstable propagation was arrested at approximately -6.35 mm (-0.25 inches). Specimens S3 and S4 experienced slightly earlier arrest. Large increases in applied load, proportional to fastener torque, were required to propagate the crack around the fastener. The finger-tight specimens (S1, S2) required an average of 57.9kN (13.0 kips) to reach 19.1 mm (0.75 inches), while the highest torque specimen (S7 at 9.04N-m/80.in-lb) required 70.3kN (15.8 kips). At this crack tip location, the fastener provided 47%–78% additional load capability over the strength of the matrix itself. Between 19.1 mm (0.75 inches) and the end of the test, crack propagation remained marginally stable, as shown by the shallow slope of the curves. Specimens S5, S6, and S7 experienced unstable propagation between 15 mm (0.6 inches) and 60 mm (2.4 inches). All specimens except S2 were tested to ultimate failure. All failures occurred when the crack tip was within 50 mm (2 inches) of the grip. The test was terminated in S2 when the crack tip reached the grip to preserve the specimen. The long panel with 50% 0° layup generally recorded lower loads at any crack tip location when compared to the short panel equivalent. This could be partly attributed to the change in manufacturing process from vacuum bag in autoclave to heat

press. The effect of this could also be seen in the noticeably lower axial stiffness in the specimens from the long panel (table 7).

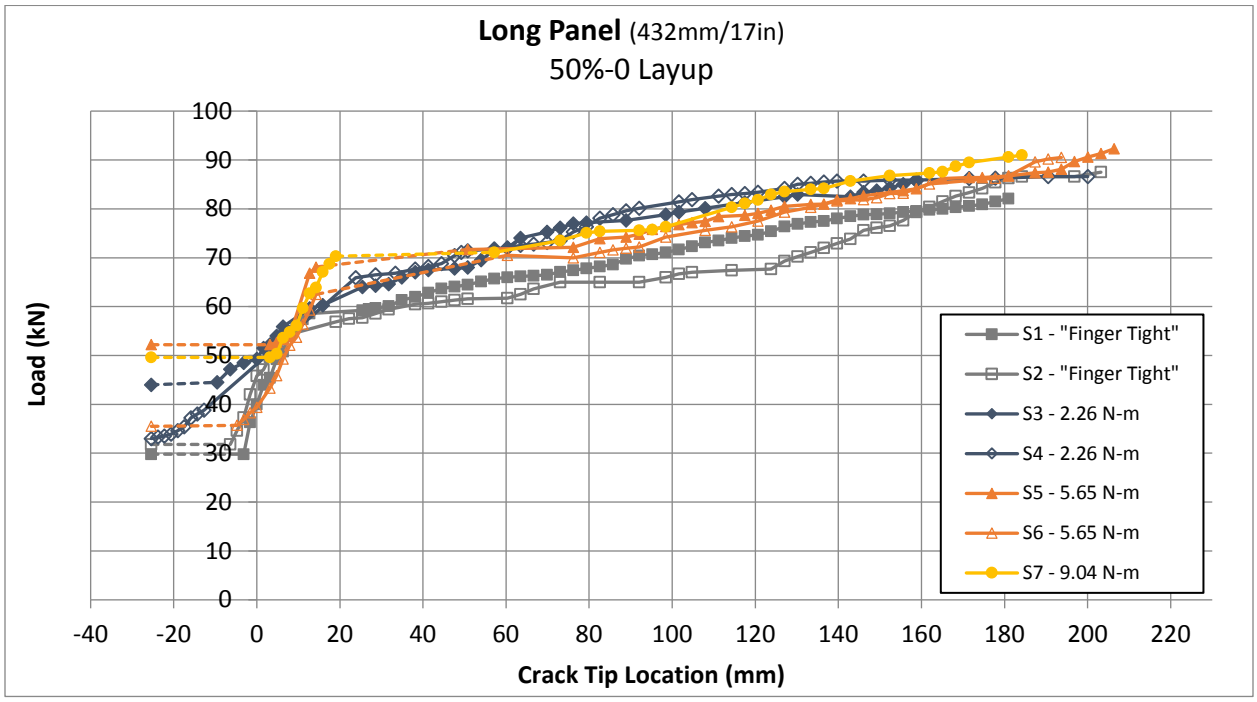

Figure 19. Applied load vs. crack tip location—long panel (50% 0-deg layup) [3]

More stable propagation was generally observed in the long panel specimens. This appeared true even for the specimens with high fastener torque. The long panel specimens provided better quality data for the stable propagation regime (after the crack tip exited the fastener location), as the longer specimens provided more area for propagation and data collection. This was especially evident for the long panel with 50% 0° layup, in which most specimens ended the test with final-crack tip locations of approximately 200 mm (8 inches) and ultimate loads near 90 kN (20 kips).

The percentage improvements in load capability with respect to fastener torque are plotted in figure 20. The improvement was calculated using the load at a reference crack-tip location of 19.1 mm (0.75 inches) for each specimen, divided by the average initial unstable propagation load from all the specimens in the same panel. The reference location of 19.1 mm (0.75 inches) was chosen because it marked the last point at which the crack tip was still being effectively arrested. When the crack tip exited the fastener area, the crack propagation rate greatly accelerated and often became unstable for a substantial distance. A clear trend can be identified from figure 20. The load improvement in propagation load increased with layup stiffness and fastener installation torque. While the layup of a structure is usually determined by the structural needs, the fastener torque could be controlled by using different fastener size, material, or change in installation process. It should be noted that the percentage improvements shown in this study are specific to the specimen configuration and the load case tested. They are not generally applicable to any other specimen configuration, load case, or real structures.

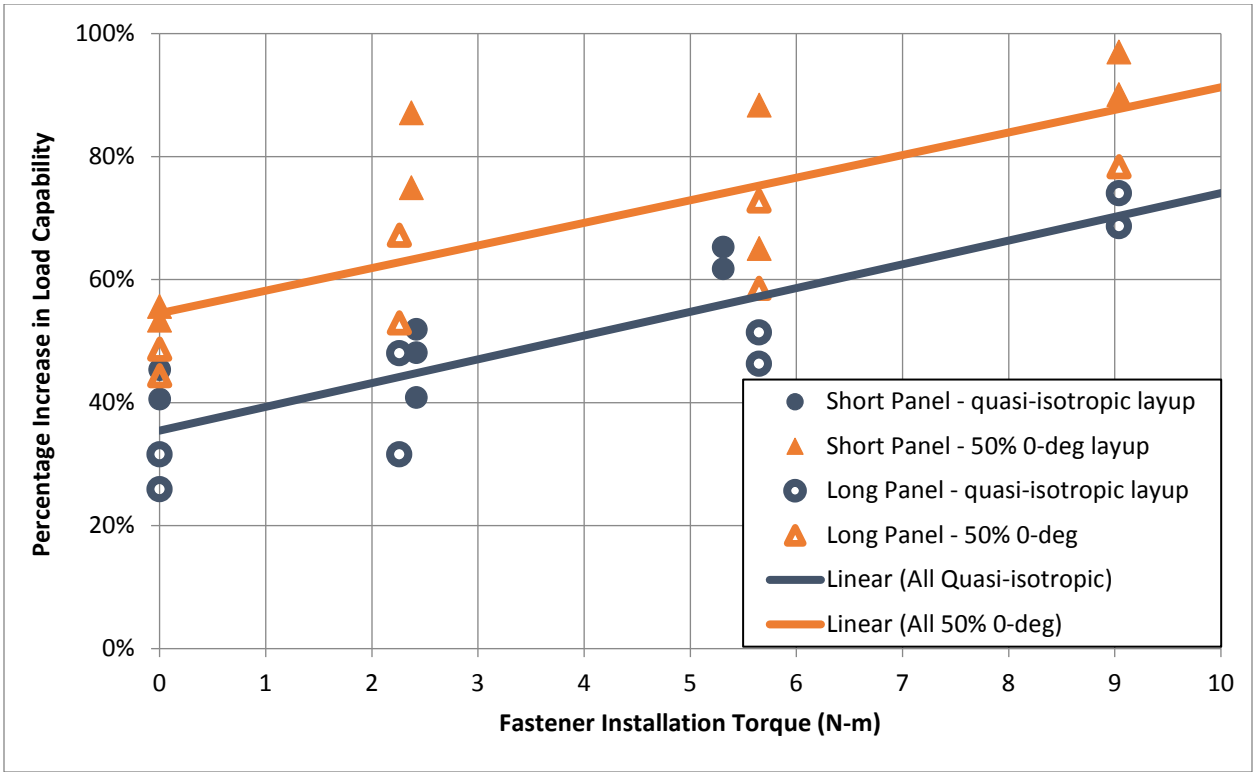

Figure 20. Improvements in load capability vs. fastener torque [3]

Post-test inspection of the test specimens revealed that the crack tip had a high tendency to jump from the 0/0 interface to the adjacent 0/45 interface after some lengths of propagation past the fastener (figure 21). This occurred because crack propagation beyond the fastener was forced to be pure mode II. However, the mode II fracture toughness of the matrix interface was high, providing high resistance to pure mode II cracking. This crack-tip shear could also be transformed into tension 45° away from the plane of the original crack interface. This tension drove failure 45° through the thickness of the 0° ply, but the crack could not easily cut across the 0° ply because strong fibers prevented cracking across the ply thickness. Therefore, this interlaminar failure mechanism was observed as the crack-jumping interface. Once the crack jumped to the 0/45 interface, it became even easier for the crack to cut across the 45° ply. As a result, additional changes in crack interface were commonly observed after the first jump from the 0/0 interface. Such behavior was not common in material property tests (e.g., DCB, ENF) because the specimens were usually made with a stack of 0° plies. In real structures, changes in crack interface would be much more common because of more general layups and complex loading.

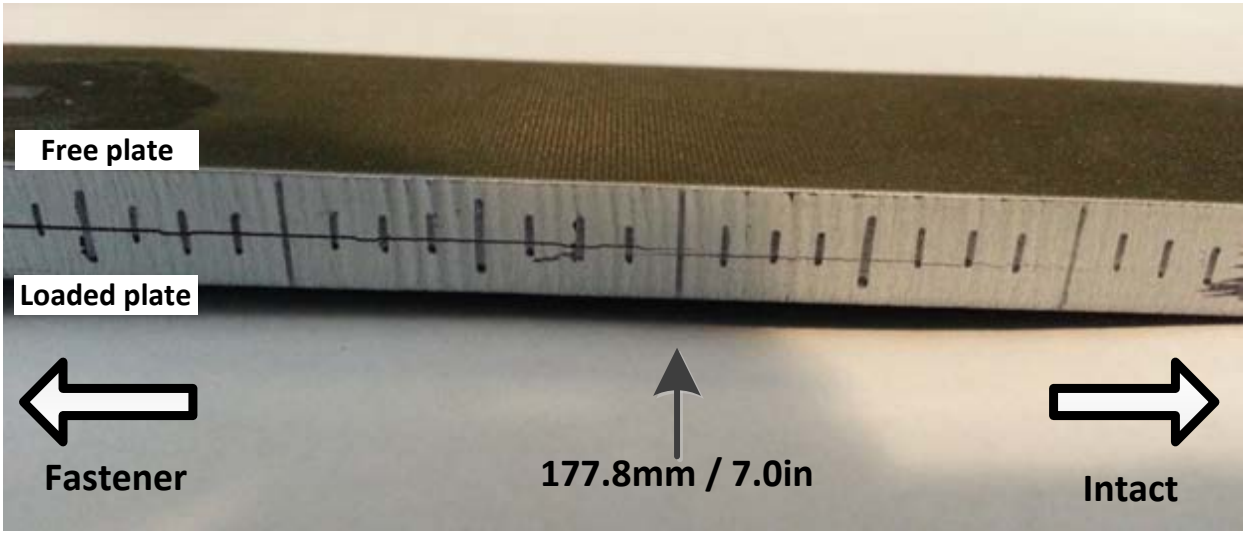

Figure 21. Photo of specimen showing changes in crack interface, which occurred during a test [3]

2.2.3 Crack Propagation Behavior Discussion

Figures 22 and 23 illustrate crack-front geometries and crack-growth behavior at various stages of the test. Upon initial loading, the initial crack visibly opened up because of the load eccentricity of the specimen configuration. At this stage, the fastener was not loaded, and the specimen behaved simply as a single-lap hard point with a crack. Although the load was applied in the axial direction, the crack tip was under mixed-mode condition. There was no crack propagation as long as the applied load was below the critical load for crack-tip fracture.

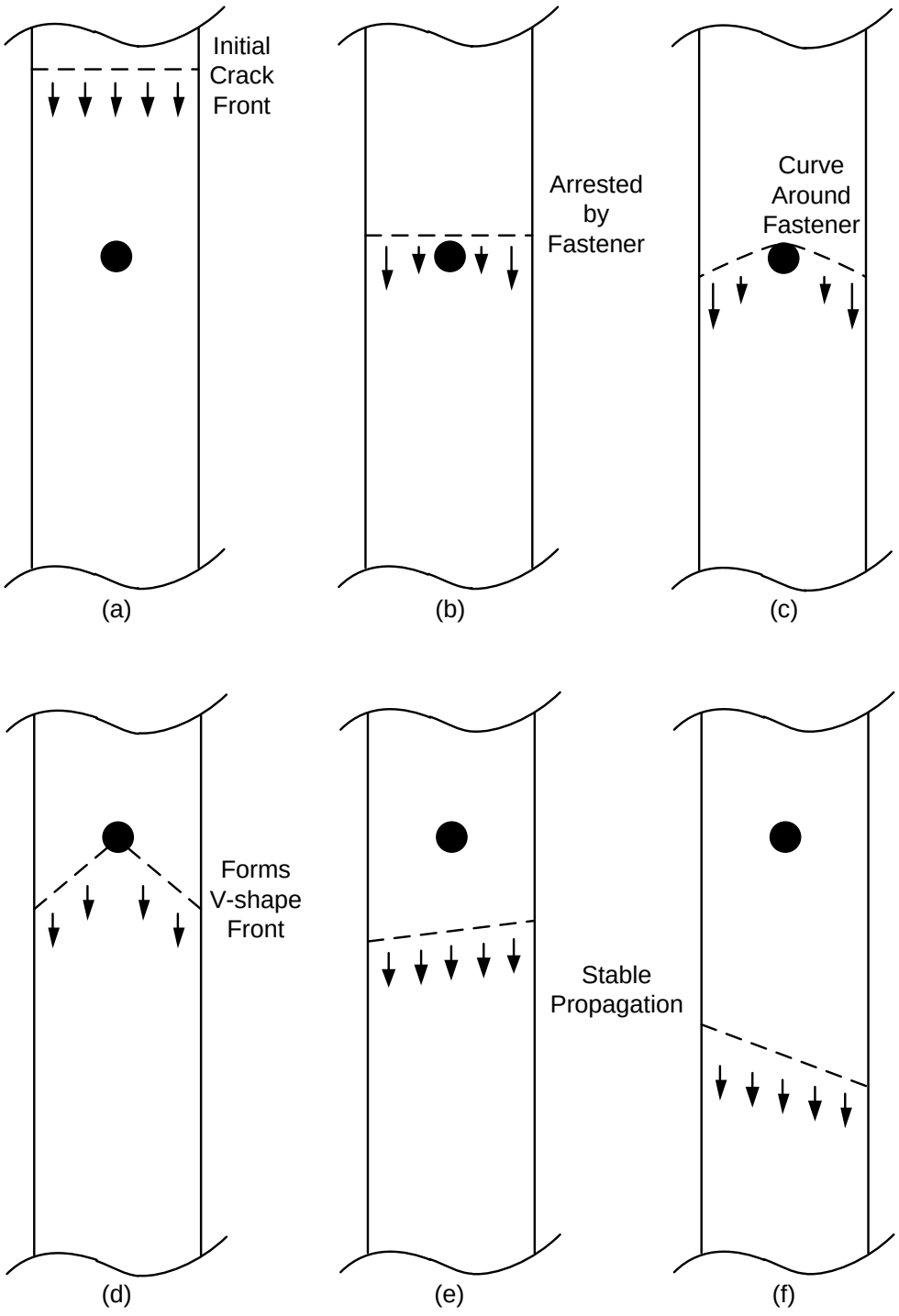

Figure 22. Crack propagation behavior—crack front geometries
(a) pre-arrestment; unstable propagation
(b) – (d) arrested; very limited propagation
(e) – (f) stable propagation [3]

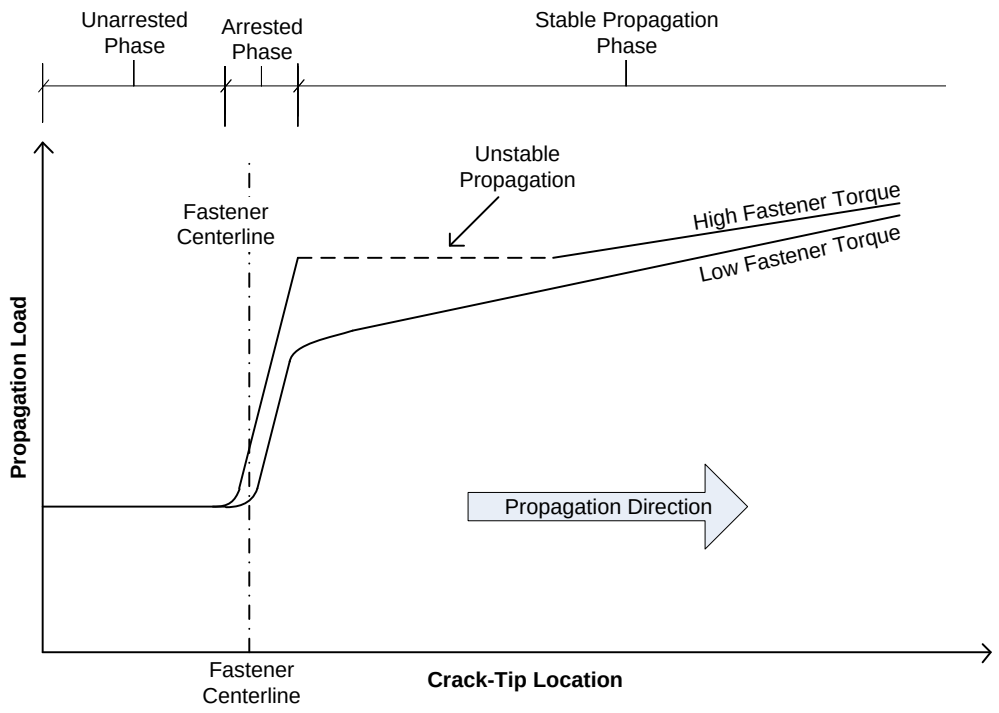

Figure 23. Crack-propagation behavior with arrest fastener [3]

The "pre-arrestment" phase began as the critical load was reached for the initial crack. The crack began to propagate based on the mixed-mode fracture law. However, crack propagation in this phase was unstable or marginally stable. This was because the crack-tip loading condition did not change as the crack propagated. The energy-release rates and mode-mix ratio remained the same, at the critical values, at the same applied load regardless of crack-tip location. Without any crack arrestment feature, the propagation would be catastrophic and the specimen would split into two halves. When a delamination arrest fastener was installed, the crack tip jumped to the fastener location and was stopped. That ended the unstable propagation in the pre-arrestment phase.

The arrested phase began when the crack tip stopped growth at the edge of the fastener (including head/nut and the washers). A large increase in applied load was required to further grow the crack. Even then, the crack growth rate with respect to load increment was extremely low. This slow growth occurred around the fastener and could be observed from the edges of the specimens. The center of the crack front directly under the fastener was almost completely stopped. While unable to directly observe the geometry of the crack front, previous studies revealed that the crack front forms a V-shape centered on the fastener. An example of this crack front is shown in the C-scan picture in figure 24. Crack propagation, though not entirely stopped, was practically arrested by the fastener. The arrested phase ended when the leading edges of the crack front were pushed approximately one fastener diameter past the fastener (for the specimen geometry and configuration tested). When the crack exited the fastener, the crack-propagation behavior changed, marked by a significant increase in propagation rate.

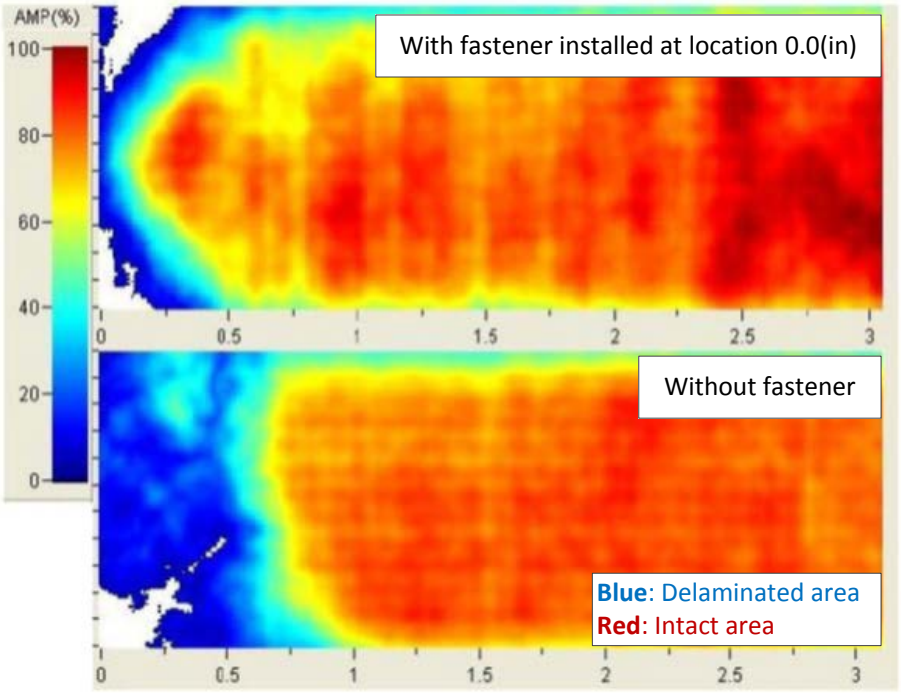

Figure 24. C-scans of crack-front geometries with and without a crack-arrest fastener [3]

In the arrested phase, higher fastener installation torque effectively increased the load required to push the crack out of the fastener location. Fastener torque, and ultimately crack-face friction, was a major parameter affecting the crack-arrest capability of the fastener.

The term "arrested" is borrowed from the metallic structure design experience to describe the observed crack behavior and to reflect the purpose of the crack-arrest fastener. In metallic pressurized vessels, crack arrestment features act by turning the crack away to a more harmless direction and preventing the unzipping of the structure. This happens before the through-thickness crack reaches the arrestment feature, usually in the form of a tear strap or a bonded doubler. The crack is contained between arrestment features, preventing catastrophic failure. However, in laminated composite structures, delamination propagation remains in the same interface. Mechanical arrestment features that reinforce the through-thickness strength of the structure, like fasteners and stitches, only become effective after the crack reaches the area occupied by the arrestment features. Also, only mode I can be effectively suppressed. The crack can continue to propagate in mode II/III. In this study, the in-plane load that drives G_{II}, tension in the laminate, was mostly unaffected by the closing of the crack tip. When sufficiently high load was applied, the crack propagation would resume. In other words, crack propagation was severely retarded, but never absolutely arrested. The term arrested was used to describe the apparent behavior of the crack in this phase of the test.

Crack propagation progressed to the stable propagation phase, at which the crack tip exited the local area of fastener influence. The transitional behavior from the arrested phase to the stable propagation phase differed noticeably depending on the fastener torque. For test specimens with minimal torque (finger tight), the transition was smooth, with a gradual increase in the crack-

propagation rate with respect to load as the crack tip existed the fastener. Subsequent propagation remained stable, approximately at a constant rate. For specimens with higher fastener torque, the transition to the stable propagation phase was much more abrupt. The crack jumped away from the fastener in an unstable fashion for some length before the crack growth slowed and propagation stability was regained. The length of the unstable propagation was generally proportional to the fastener torque. The stable propagation rate was approximately the same for different fastener torques, although the propagation loads were generally higher for the higher torque specimens. This behavior appeared to be attributed to the same mechanism (i.e., crack face friction), which increased the retardation capability with fastener torque. However, this trend may also indicate an underlying, less-understood behavior related to the propagation behavior in the vicinity of the fastener. When the crack tip was under the fastener, the fastener preload and friction effectively locked the crack tip in place. As the crack tip exited the fastener, it no longer interacted with the preload and friction (even though the preload and friction forces remained unchanged and continued to act on the crack face under the fastener), reversing the retardation effect of this interaction. This led to a period of unstable propagation as the lost retardation capability was recovered by the load transfer in the shear joint (which increased with crack length). The behavior observed in tests was consistent with the finite element studies.

The crack-propagation behavior in the stable-propagation phase was relatively consistent among specimens with different layups and fastener torque. The load-versus-crack-tip location curves are approximately parallel but eventually converge as the crack tip nears the test machine grip. This could be a boundary condition effect. The propagation stability was primarily provided by the fastener shear joint load path, the property of which may be quantified by the fastener-flexibility approach. The fastener joint was the only mechanism that provided increasing retardation capability as the crack length increases.

At ultimate failure of the specimen, the load-bearing sublaminate failed at the fastener hole. The failure mode was filled-hole tension (more specifically, tension bearing bypass because the fastener was transferring shear load).

2.2.4 Correlation of Analytical Method to Test Data

The analytical method developed in this study was correlated and validated with test results in this section. The test data from all four specimen configurations were used (short panel and long panel, each with quasi-isotropic and 50% 0° layups). The goal was to show the analytical method capable of capturing the delamination propagation behavior with a fastener feature using basic properties, such as laminar material properties, fracture toughness, and fastener properties.

The dimensions of the analytical model replicated the dimensions of the test specimen between the test-machine grips (figure 25). The distance from the fastener to the test-machine grip on the intact side was 127.0 mm (5 inches) for the short panel and 228.6 mm (9.0 inches) for the long panel. The distance from the fastener to the grip on the initially cracked side was 89 mm (3.5 inches) for both panels. The grips were represented by fixed boundary conditions, in which out-of-plane displacement and slope were set to zero. The specimen width was 31.75 mm (1.25 inches). Nominal ply thickness of 0.1905 mm (0.0075 inches) was used. The 48-ply specimen had a total thickness of 9.14 mm (0.36 inches); the 24-ply sublaminates were 4.572 mm (0.18 inches) in thickness.

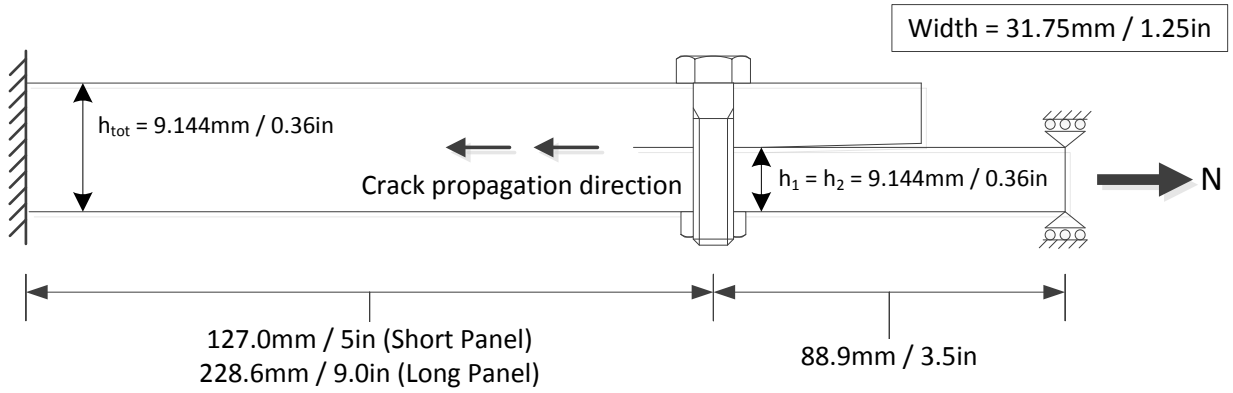

Figure 25. Schematic of analytical model for test correlation [3]

Table 8 summarizes all the basic material properties used in the analytical model and some derived structural properties, namely the effective axial stiffness of the laminates and the fastener joint shear stiffness calculated using the fastener flexibility approach. BMS 8-276 (Toray T800S/3900-2) laminar tape properties were used. The laminate in-plane axial stiffness in the loading direction based on classical laminate theory was 59.2 GPa (8.59 msi) and 86.9 GPa (12.6 msi) for the quasi-isotropic panel and the 50% 0-deg panel, respectively. They were 11–14% higher than that measured by strain gauges in the test (table 7). This discrepancy was attributed to the imperfect manufacturing processes that led to ply sliding and rotation. The in-plane stiffness of a composite panel was very sensitive to ply rotation. It was also evident that the long panel, which experienced low-temperature ramp-up rate during cure in the heat press, suffered from higher stiffness discrepancy. The fracture toughness values (G_{IC} and G_{IIC}) were taken from the T800H/3900-2 material system, which used the same epoxy resin but with a higher modulus fiber. Odagiri et al. published a G_{IIC} of 2450J/m^2 (14in-lb/in^2) [17].

Table 8. Properties used in calibrated analytical model [3]

	SI Units	English Units
E_1	142.0 GPa	20.6 msi
E_2	7.8 GPa	1.13 msi
v_{12}	0.34	
G_{12}	4.0 GPa	0.58 msi
G_{IC}	280 J/m^2	1.6 in-lb/in^2
G_{IIC}	1751 J/m^2	10 in-lb/in^2
Fastener diameter	6.35 mm	0.25 inches
Fastener elastic modulus	113.8 GPa	16.5 msi
E_x (quasi-isotropic)	59.2 GPa	8.59 msi
E_x (50% 0-deg)	86.9 GPa	12.6 msi
Joint shear stiffness (quasi-isotropic)*	12733 N/mm	72708 lb/in
Joint shear stiffness (50% 0-deg)*	17073 N/mm	97491 lb/in

* Estimated values: Huth's fastener flexibility with a constant "static test" knockdown of 0.4

However, this value of 2450J/m^2 corresponded to the fracture toughness without pre-cracking. The pre-cracked G_{IIC} has been found to be 1730J/m^2 (9.9in-lb/in^2). The fastener joint shear stiffness used in the model was the input parameter with the least certainty. The fastener flexibility approach was developed to capture the joint shear flexibility under fatigue loading. The joint flexibility measured during fatigue hysteresis loops (C2/3) was used to create the fastener flexibility formula [11]. However, Huth's test data showed that the joint flexibility would be more than two times higher and highly nonlinear in a static test condition (figure 26 [11]). As a result, an approximated "static test" knockdown factor of 0.4 was applied to the fastener joint shear stiffness calculated from the fastener flexibility formula. This constant factor was applied to all joint shear stiffness calculations and remained the same for the duration of this study.

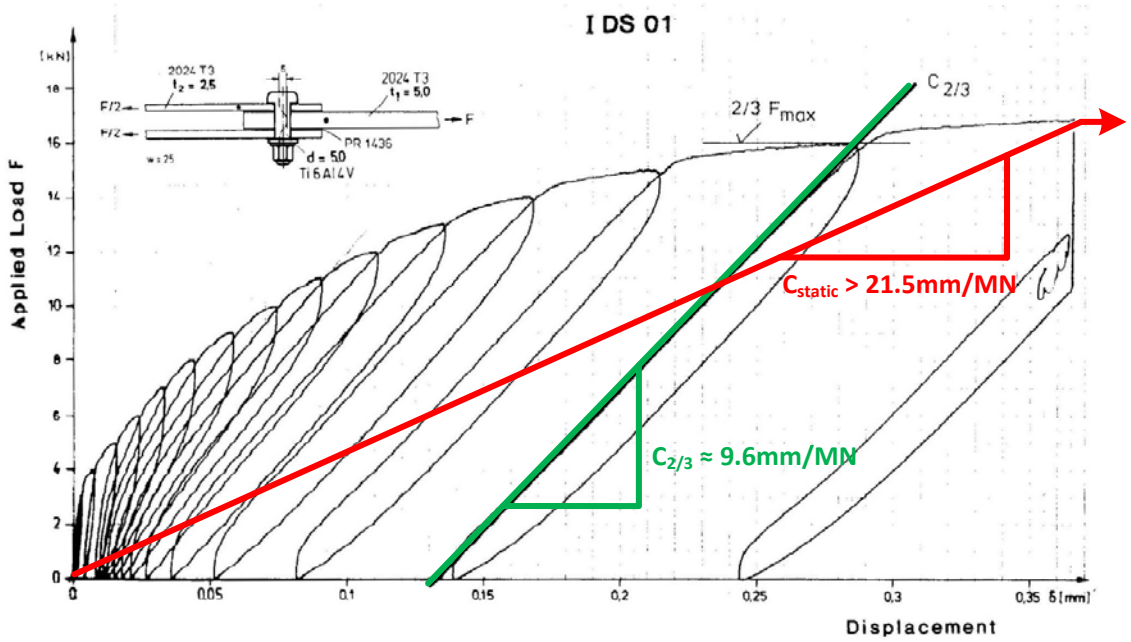

Figure 26. Fastener joint shear flexibility—fatigue vs. static flexibility [11]

Figures 27 and 28 show the analytical simulation of the short-panel specimen tests overlaid on the test data, whereas figures 29 and 30 show that of the long panel specimen tests. Although the friction due to fastener preload in the test specimens was not measured empirically, different magnitudes of friction forces were simulated for comparison. The three friction conditions analyzed were frictionless, 2.22 kN (500 lb), and 4.45 kN (1000 lb)[2]. The initial unstable crack propagation load was simulated by moving the crack-tip location to 25.4 mm (1.0 inch) ahead of the fastener, while setting the stiffness of the fastener axial and joint shear springs to zero. Separately, an analysis was added for each of the four panels using the fatigue fastener flexibility values instead of the estimated static fastener flexibility. This was done only for the case with 4.45 kN (1000 lb) friction and is meant to demonstrate the potential difference between static and fatigue fastener flexibility. Last, a set of analyses simulating the "no-tab" tests were performed for the short panel quasi-isotropic layup specimens. This was achieved by applying an out-of-plane deflection of 2.286 mm (0.09 inches), which is half of the thickness of the tab, to the boundary condition of the lower plate at the crack tip end.

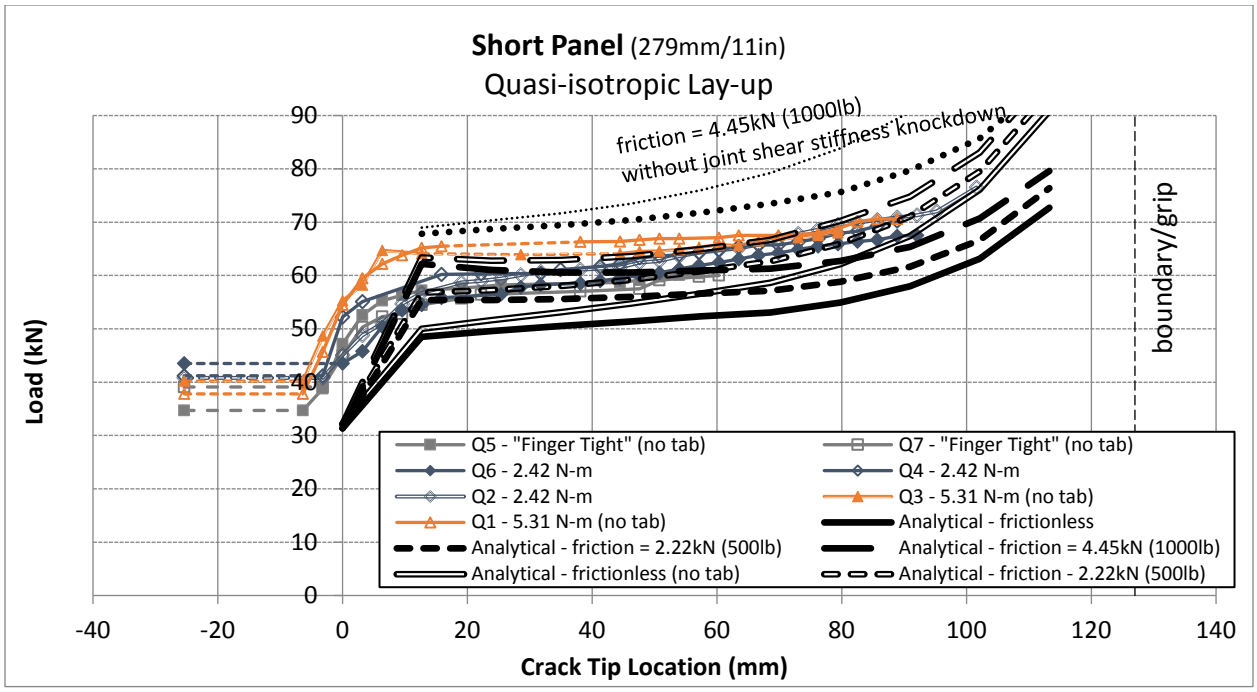

Figure 27. Analytical method vs. test results—short panel quasi-isotropic layup [3]

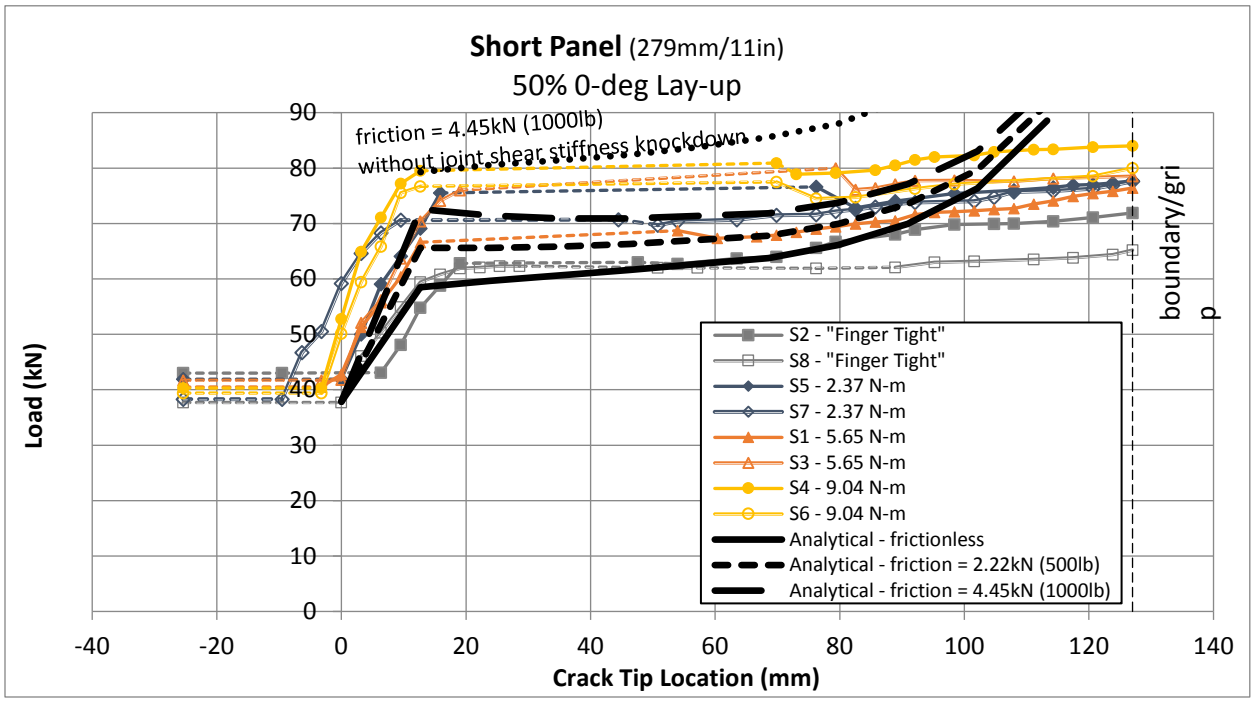

Figure 28. Analytical method vs. test results—short-panel 50% 0º layup [3]

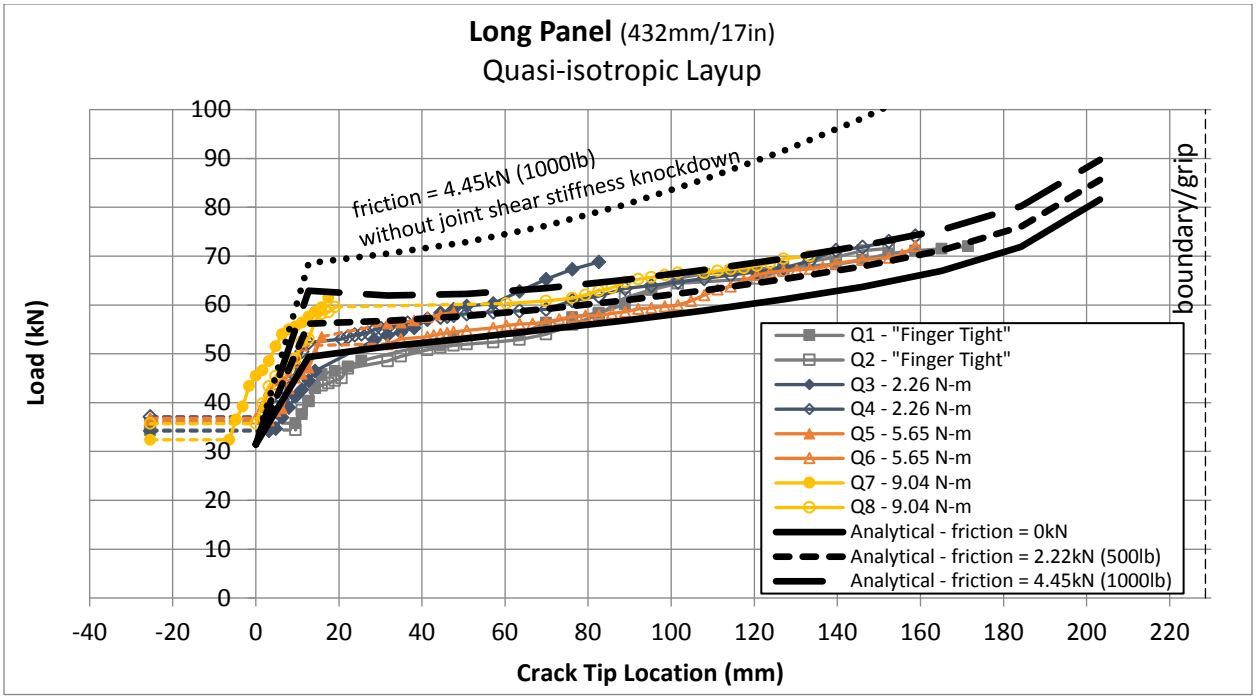

Figure 29. Analytical method vs. test results—long-panel quasi-isotropic layup [3]

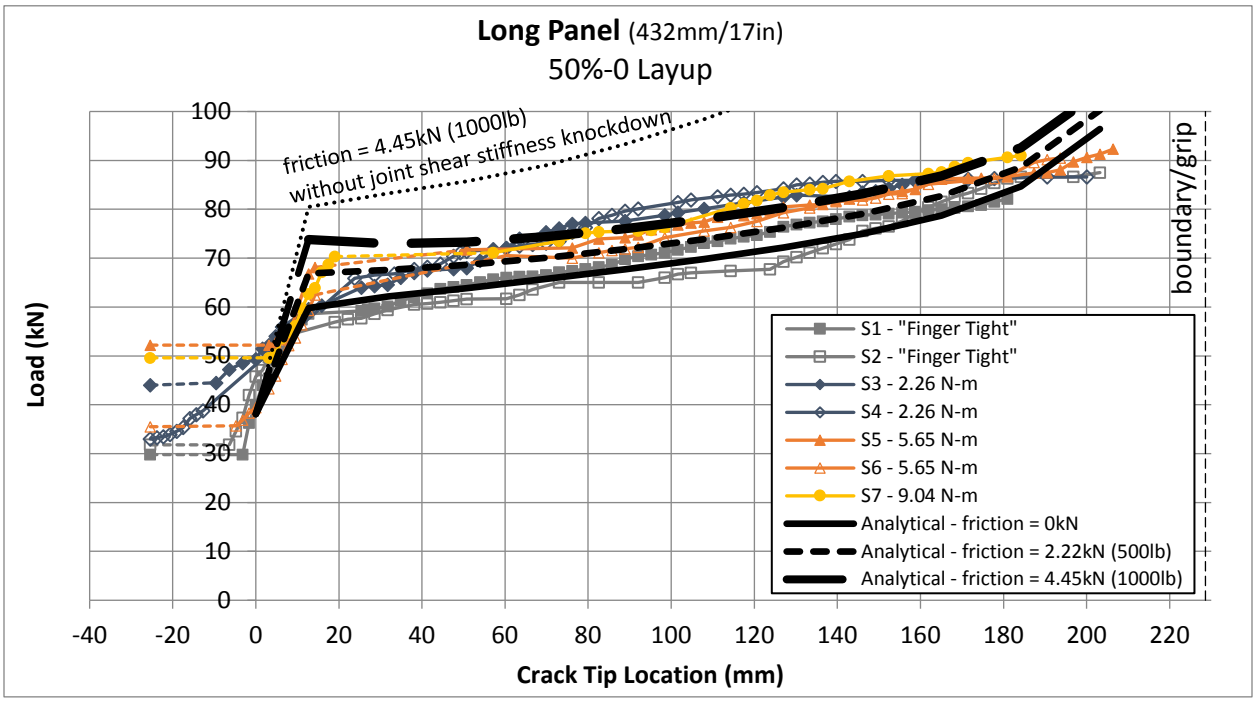

Figure 30. Analytical method vs. test results—long-panel 50% 0-deg layup [3]

The analytical model demonstrated good correlation to the test data from two panel lengths, two laminate layups, over a range of fastener installation torque (and therefore a range of preload and friction forces). The model predicted the crack propagation loads in all specimens with good

accuracy. In addition, the model also accurately captured key behavioral trends of crack propagation in a split-beam with a fastener arrest feature. First, the analytical model accurately predicted the step increase in propagation load by suppressing the mode I fracture component. The unstable propagation load that defined the bottom of the step and the continued propagation load that defined the top of the step correlated well with test data. The effect of friction on the increase in propagation load also correlated well with the test data with different fastener installation torque. The initial unstable propagation loads measured in the test had large scatter and were often higher than the model prediction, primarily because of the fact that the specimens were not pre-cracked before testing. Second, the model accurately predicted the unstable crack propagation behaviors when the crack tip exited the fastener area (as flat or downward curing segments in the analytical simulations). The model had apparent success in capturing the two parameters that have the most significant effect on increasing the length of the unstable propagation, the fastener installation torque (friction force), and the length between the fastener and the boundary on the intact side (i.e., shorter specimens had longer unstable crack propagation). Last, the model accurately predicted the stable crack propagation after the crack tip exited the fastener area, except when the crack tip approached the boundary.

However, the analytical model was not without inadequacies. The most obvious discrepancy was observed for the stable crack propagation behavior when the crack tip was within 50 mm (~1.0 inch) from the boundary. The propagation load predicted by the analytical model increased quickly and diverged from the test results because of boundary effect. The divergence was most prominent in figure 28 and figure 30, in which the high stiffness specimens provided crack propagation data points all the way to the boundary (test-machine grip). This was because in the analytical model, the grip represented a perfectly clamped boundary condition. However, the segment of the test specimens inside the grip was able to shear, therefore softening the boundary effect on crack-tip forces and moments. As a result, the test specimens had longer effective lengths that extended into the grip. This discrepancy was less observable in the quasi-isotropic layup specimens, simply because the laminate failed (either in bending near the grip or in filled-hole tension) before more crack propagation data could be collected near the grip.

Another observation that was not modeled in the analysis was the change in delamination interface. In the tests, the crack interface had a tendency to jump into the loaded sublaminate. The crack interface was often observed to dive into the loaded sublaminate by one to two plies (figure 21). This had the effect of increasing the crack-tip forces and moments as the load transfer between the thinner loaded sublaminate and the other thicker sublaminate increased. As a result, the crack-propagation load would be lower. The analytical model did not take this into account. This could also explain why the model predicted sharp increases in propagation loads near the boundary, whereas the test data did not exhibit this behavior (except the Q2 specimen in figure 27).

3. SINGLE FASTENER MODELING

The purpose of FEA was to provide insights into the underlying mechanics of mixed-mode crack propagation and using fasteners as a crack-arrest mechanism. The understandings provided by the FEA were instrumental in the final design of the test specimen and the interpretation of the test results. The FEA model was also used to verify the analytical methods previously described.

A simplified two-dimensional model of the fastener crack arrest mechanism, shown in figure 31, was used to evaluate the effectiveness of the fastener as a crack arrest mechanism. The model was similar to that of a composite DCB, but with general applied loads and moments. A fastener was added in front of the crack tip in the DCB. The change in crack-propagation behavior before and after the crack encountered the fastener was investigated.

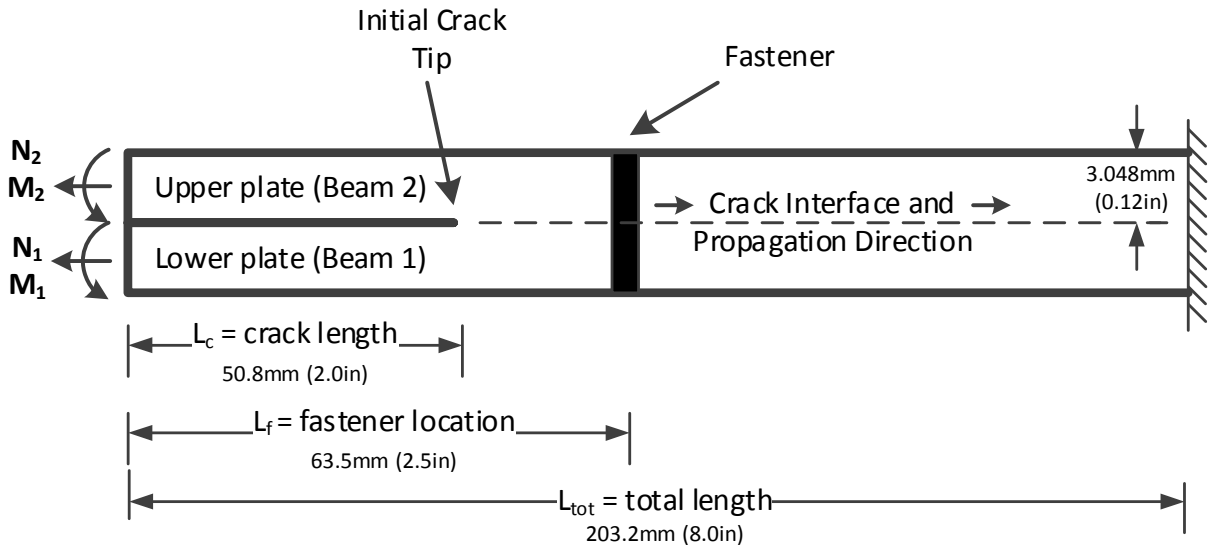

Figure 31. Diagram of the crack arrest finite element model [3]

The DCB with fastener was modeled with finite elements and the crack propagation behavior was numerically simulated in commercial FEA software, ABAQUS. Crack propagation was analyzed using VCCT. VCCT is a finite element approximation of the modified crack closure technique [12], which calculates the mode-decomposed crack-tip strain energy-release rates based on linear elastic fracture mechanics. The fastener was modeled by two independent spring elements: one captured the axial stiffness of the fastener, and the other captured the shear stiffness of the fastener shear joint. The stiffness of the shear joint was calculated using the fastener flexibility approach by Huth [11].

The capability of the crack arrest fastener was measured in terms of the crack-propagation load. For unstable cracks, the crack-propagation load would either decrease or remain the same as crack length increased. This implied that the structure would fail catastrophically as soon as the critical propagation load was reached. For stable cracks, the crack-propagation load would increase as crack length increased. This increase in crack-propagation load due to the crack arrest fastener was the subject of this study.

3.1 FEA MODELING

ABAQUS FEA was utilized because the program was the first to implement VCCT elements developed by Mabson et al. into a subroutine [13]. This allowed for the virtual propagation of the crack via repeated static finite element simulations, greatly simplifying the modeling of crack growth and arrest compared to other techniques.

H. Huth's fastener flexibility solution was employed to find the shear stiffness of the fastener. Because this closed-form solution was developed with coefficients for carbon/epoxy adherends, it was chosen from among various competing formulae. Cheung [3] identified a key shortcoming for static design, as this equation was devised using fatigue testing, which resulted in a requisite knockdown factor of 0.4.

3.1.1 Model Design

The finite element model used in this study was comprised of a lower plate, an upper plate, and a fastener (figure 31). Identical 16-ply symmetric, balanced laminate layups were used for both upper and lower plates. Identical, symmetric balanced layups were used to eliminate any crack-tip loading caused by thermal expansion and tension bending coupling. The layups used were $(45/0/-45/90/45/0/-45/90)_s$ and $(45/0_2/-45/0_2/90_2)_s$, representing 25% 0° plies (quasi-isotropic layup) and 50% 0° plies (high-stiffness layup), respectively. It was assumed that the crack was located at and confined to an infinitesimally thin matrix interface between the upper and lower plates. Fiber bridging and crack interface switching were not considered in the analysis. It was assumed that crack propagation occurred when the critical strain energy rate was reached, regardless of bond type at the interface (co-cured, co-bonded, or secondary bonded) or fracture failure type (cohesive failure or adhesive failure). The effects of bond type and fracture failure type on the value of the critical strain energy release rate were beyond the scope of this study. The same model type was used for both the three-plate and two-plate FEA models, with the exception being the inclusion of a third plate for the pure mode II specimen.

The model was 203.2 mm (8 inches) in length and 31.75 mm (1.25 inches) in width. The initial crack length was 50.8 mm (2 inches). The fastener springs were located 63.5 mm (2.5 inches) from the cracked end. There was 12.7 mm (0.5 inches) space between the initial crack tip and the fastener. The crack propagation between the initial crack tip and the fastener was not influenced by the fastener springs and was only driven by the external loads. That is, the fastener was completely inactive between the crack-tip location of 50.8 mm and 63.5 mm. As the crack propagated past the fastener, the springs reacted to the crack opening and sliding displacements and provided resistance to propagation. Contact friction between the cracked surfaces was modeled as part of this study.

In general, the loading condition in a fastener joint involves complex contact interactions and contact forces on various joint components (figure 32). In this study, the modeling of the fastener was simplified as two independent springs: one representing the axial stiffness of the fastener and one representing the shear stiffness of a composite bolted joint. This composite joint shear stiffness was assumed to encompass all the effects of fastener joint, such as fastener shear, fastener bending, fastener-laminate bearing, laminate stiffness, etc. Therefore, these individual joint mechanisms were not explicitly modeled. Also, the individual features of the fastener, such as the head/collar

and shank, were not explicitly modeled. The shear stiffness of the bolted joint was obtained using the fastener flexibility approach. Considering the simplified free-body diagram of the fastener shown in figure 33, the in-plane forces (N) applied by the upper and lower plates generate a total moment (M) that must be reacted by the fastener head/collar and shank. For static equilibrium, $M = N \times (h_1+h_2)/2$, in which h_1 and h_2 are the thicknesses of the lower and upper plates, respectively. This was modeled by attaching the shear spring to the two plates at the crack interface instead of their neutral plane, resulting in a moment with the correct sense and magnitude when the joint was loaded in shear. The distribution of moment between the upper and lower plates was of lesser importance, because the mechanically fastened plates were constrained to rotate together by the clamping force of the fastener.

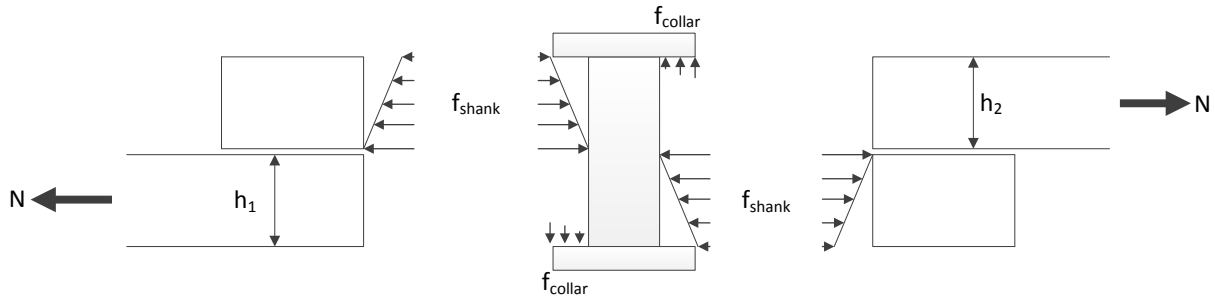

Figure 32. Contact forces in the fastener and plates in single shear [3]

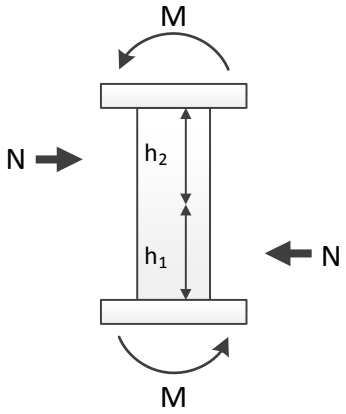

Figure 33. Net forces and moments in the fastener in single shear [3]

Loads were applied to the free end of the plates, whereas the intact end was attached to a fixed boundary. In this finite element study, only two load cases were considered. The first load case applied symmetric opening moments to the two plates, resulting in pure mode I loading at the crack tip. The second load case applied tension only to the lower plate, resulting in mixed-mode I/II loading at the crack tip. The second load case was representative of a skin-stringer flange termination, in which the skin was loaded in tension and the flange termination was not loaded. These load cases were chosen because they demonstrated the effectiveness of fasteners in arresting propagation and represented configurations that could be tested at a coupon level. The axial compression load case was not considered because it would result in pure mode II crack tip loading

(i.e., closing crack tip moment), which is less severe than mixed-mode I/II loading from the tension load case.

3.1.2 Material Properties

The laminar properties used were those of the AS4/3501-6 material system (table 9) [18]. The mixed-mode fracture criterion, B-K law as shown by equation 1, was used to determine crack-tip fracture. In general, the critical strain energy release rates for individual fracture modes and the mode-mix parameters were interface properties and not material constants for composite materials. The fracture parameters could depend on a multitude of factors, such as the ply orientations bounding the crack interface, manufacturing process, interface additives, and the type of bond failure if a bonded structure was considered (i.e., cohesive versus adhesive failure). However, only a single set of parameters was used in this study.

$$G_{equivC} = G_{IC} + \left(G_{IIC} - G_{IC}\right)\left(\frac{G_{II}}{G_I + G_{II}}\right)^{\eta} \tag{1}$$

Table 9. Carbon fiber reinforced plastic laminar material properties (AS4/3501-6) [18]

	English Units	SI Units
Ply thickness	0.0075 in	0.1905 mm
E_1	18.5 Msi	127.5 GPa
$E_2 = E_3$	1.64 Msi	11.3 GPa
$G_{12} = G_{13}$	0.871 Msi	6.0 GPa
G_{23}	0.522 Msi	3.6 GPa
$\nu_{12} = \nu_{13}$	0.3	
ν_{23}	0.4	
G_{IC}	1.5 in-lb/in^2	262.7 J/m^2
G_{IIC}	7.0 in-lb/in^2	1226 J/m^2
η	1.75	

A titanium fastener (typically of the material Ti-Al6-V4) with an elastic modulus of 113.8 GPa (16.5 Msi) was used. The stiffness of the fastener axial spring was calculated as a constant diameter rod, $k = A \times E/(t_1+t_2)$. The stiffness of the fastener shear spring was calculated using the fastener flexibility approach. The flexibility of the unbonded bolted joint in the shear direction, C, is given by equation 2. The parameters used are: t_i = laminate thickness, d = fastener diameter, n = single or double shear joint, $E_1 = E_2$ = laminate stiffness, E_f = fastener elastic modulus, constants a = 2/3 and b = 4.2 for bolted graphite/epoxy joints. Step nonlinearity was added to the fastener axial spring to simulate fastener preload (figure 34). The effect of the contact coefficient of friction was also studied.

$$C = \left(\frac{t_1 + t_2}{2d} \right)^a \frac{b}{n} \left(\frac{1}{t_1 E_1} + \frac{1}{n t_2 E_2} + \frac{1}{2 t_1 E_f} + \frac{1}{2 n t_2 E_f} \right) \quad (2)$$

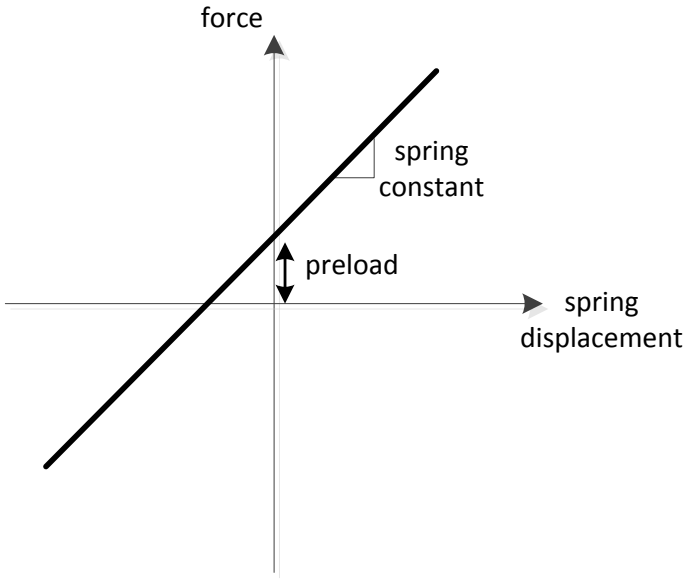

Figure 34. Nonlinear spring load-displacement curve for fastener with preload [3]

The properties of the materials and structural members were assumed to be linear elastic. The only failure considered in the FEA was crack-tip fracture and propagation. Alternate failure modes such as laminate failure, fastener failure, and bearing failure were not considered in this study. These competing failure modes would provide realistic constraints for the design and optimization of the crack-arrest feature.

3.1.3 Finite Element Model Details

The two-dimensional finite element model was constructed using ABAQUS CAE FEA software (Version 6.12-1), as shown in figures 35 and 36. The mesh was identical to that of a DCB except for the addition of the two fastener springs and load cases. The upper and lower beams were identical separate parts. The CPEG4 two-dimensional four-node bilinear quadrilateral plane strain element with reduced integration and the same mesh geometry was used in the plates. Each ply had one element mesh through the thickness (0.1905 mm or 0.0075 inches). The width of the elements in the beam-length direction was approximately 0.1905 mm (0.0075 inches), which yielded element aspect ratios close to one. The element size was kept constant to maintain the self-similar condition required for VCCT. When element sizes in front of and behind the crack tip were not the same, the energy release rate calculation for that particular crack tip node could be inaccurate.

The fastener axial spring element (ABAQUS “spring2” element) was connected to top and bottom surfaces of the DCB. Fastener preload was modeled by providing the spring element with nonlinear

properties, such that the spring was in tension at zero displacement. This was used to model the effect of fastener preload on crack propagation.

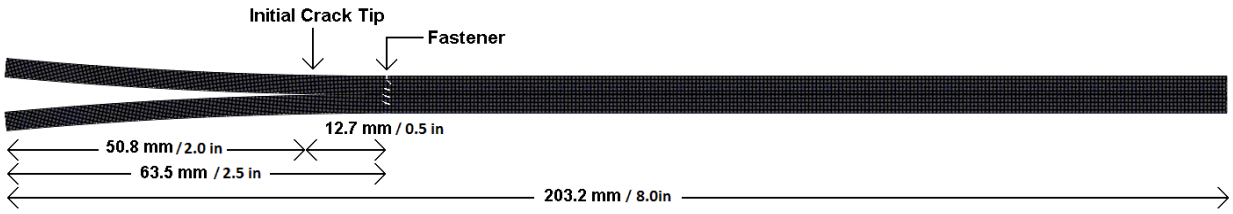

Figure 35. Finite element mesh of the split-beam model (deformed under mode I loading) [3]

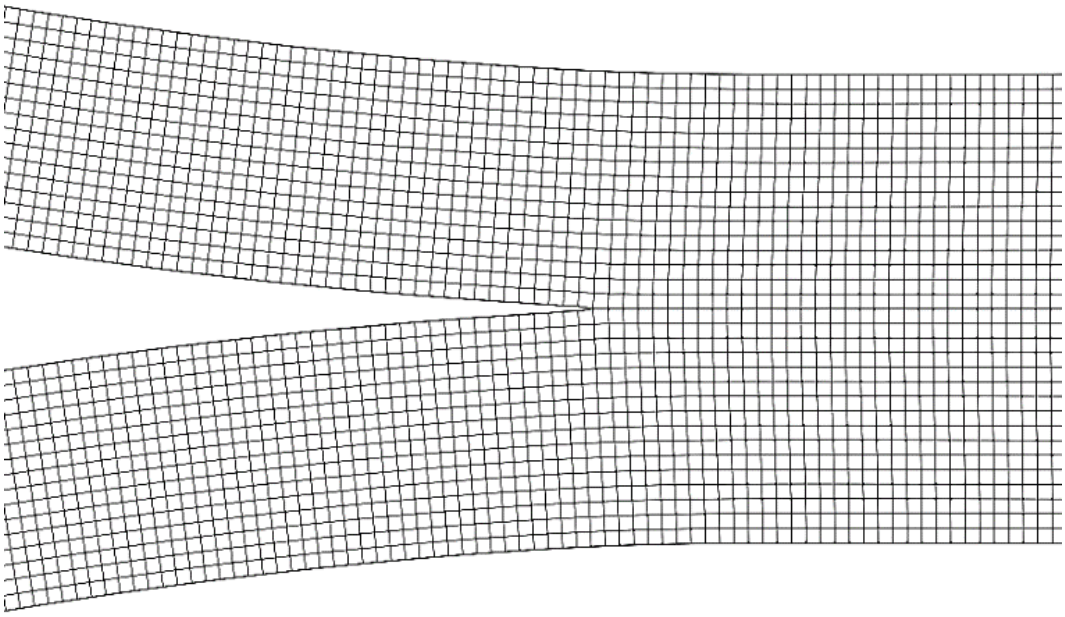

Figure 36. Finite element mesh of the split-beam model (enlarged near the crack tip) [3]

The upper and lower beams were bonded to each other along their interface using VCCT surface interaction definition in ABAQUS. The nodes along the intact portion of the beam were tied together, while the cracked surfaces behaved as free surfaces with contact and friction resolution. At the crack tip, the mode-decomposed SERRs were evaluated using the ABAQUS VCCT algorithm. The SERR for each mode was calculated separately using the nodal forces and the opening/sliding displacements behind the crack tip. The tie condition applied to the crack tip nodes was released when the mixed-mode fracture failure criterion was met, and the crack tip propagated to the next node. As the node at the crack tip was released, a new cracked surface was created. Crack face contact friction was modeled by providing coefficients of friction to the VCCT surface interaction definition. The crack propagated in the FEA in a node-to-node fashion regardless of the stability of the propagation. For example, if crack propagation was unstable with respect to the load/boundary applied, multiple nodes would sequentially release while the applied load/boundary remained constant.

The analysis was solved considering the effects of nonlinear geometry. The crack-propagation analysis consisted of many individual static equilibrium steps, one for each crack-tip node release. Essentially, each time the crack propagated forward, a new structure was created and the static analysis was repeated. Additional sources of nonlinearity included the contact conditions and friction forces on the cracked surfaces. Solution convergence was difficult given the amount of nonlinearities and instabilities in the fracturing structure. Automatic damping was used in ABAQUS to aid convergence. The amount of damping was minimized such that it made no significant impact on the solution. Thermal contraction due to curing was not simulated because the two plates were identical with symmetric and balanced layup. Therefore, strain energy release rates were not induced by changing temperature.

3.1.4 Pure Mode II Modeling Results

The modeling results for the pure mode II specimen are shown in figure 37. As hoped, the two different modeling methods agree reasonably well, but they cannot be compared to experiments because the cracks failed to propagate for these specimens. Unsurprisingly, the results show that as the fastener engaged in shear, it provided arrestment to the crack and, therefore, a constantly increasing load was required to propagate the crack. Additionally, it should be noted that increasing the value of G_{IIC} increased the propagation load. The fastener had no influence on this aspect. This was instead a material property change providing benefit.

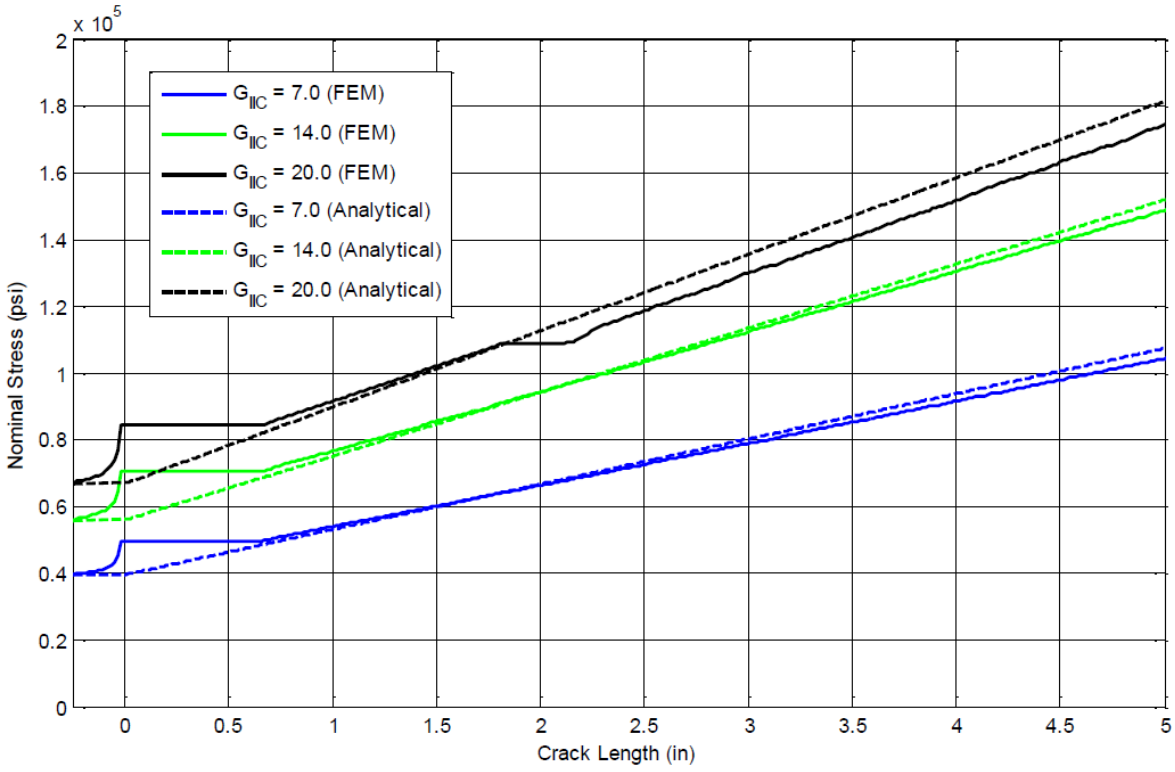

Figure 37. Pure mode II FEM vs. analytical results [2]

3.1.5 Effect of Fastener Under Mode I Loading

Mode I interlaminar fracture in composites is generally the most critical fracture mode because G_{IC} is much lower than G_{IIC} (and G_{IIIC}). The opening mode also allows moisture and contaminants to seep into the cracked surface, exacerbating the damage over cycling mechanical and thermal loading. The mechanics of crack arrest with a fastener under mode I loading is well understood. The FEA of pure mode I loading and crack arrestment are discussed here as one of the most important parts of the fastener arrest mechanism.

Figure 38 shows the applied load versus crack tip location for the 25%-0° and 50%-0° lay-ups with and without an arrest fastener. The fastener was positioned at crack location zero. Without the fastener, the crack propagation was unstable, as shown by the dotted lines in the figure. This occurred because the applied moments produced a constant G_I at the crack tip that was independent of crack length. Crack propagation was therefore catastrophic once the critical load was reached. When a fastener was included in the model, it was clear that the crack was extremely well arrested, as shown by the solid lines in the figure. This was expected because the axial stiffness of the fastener mechanically prevented the crack tip from opening, completely eliminating any mode I propagation. The crack stopped well within the diameter of the fastener. The crack was completely arrested because the pivot provided by the fastener resulted in a closing moment at the crack tip as the applied opening moment increased. The change in the axial stiffness of the lay-up did not have any noticeable impact on the arrest effectiveness of the fastener. It was also observed that the required moment increased slightly (~1 mm) before the crack tip reached the centerline of the fastener. This was because the beam bending caused deflection at the fastener even before the crack tip reached the fastener. For a real fastener, crack propagation would be arrested at the edge of the fastener head/collar and washer. Although not modeled in the FEA, the ultimate failure mode under mode I loading would likely be laminate failure in bending, fastener failure in tension (e.g., net section failure, head/collar failure), or fastener pull-through.

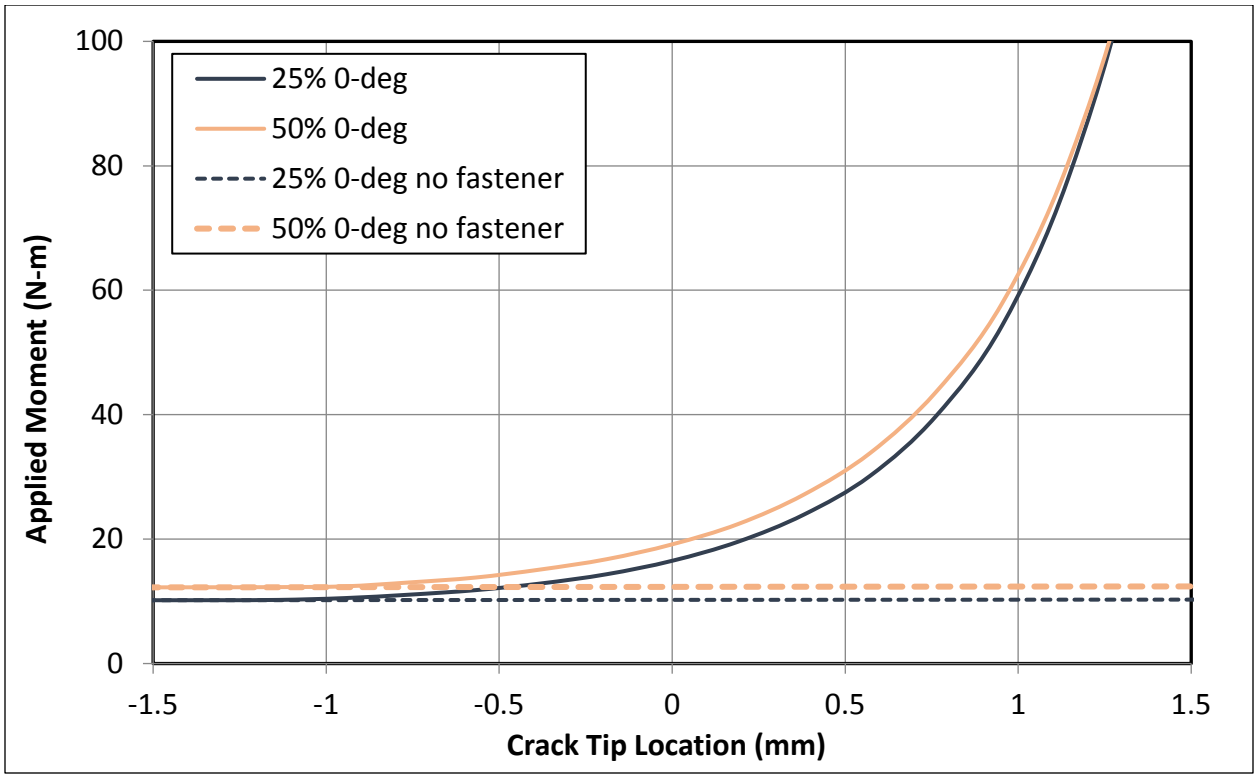

Figure 38. Propagation load vs. crack-tip location in mode I [3]

3.1.6 Effect of Fastener Under Mixed-Mode Loading

In general, composite structures experience mixed-mode I and II loading conditions at the delamination/disbond interface. Under tension, load-path eccentricity produces a secondary moment, which opens the crack tip. Such a configuration could be found when a stringer flange terminates on a skin under tension. Under compression, the secondary moment would be in the closing direction. However, local buckling could occur because the delamination could reduce the thickness and increase the effective length of the cracked sublaminates. In addition, post-buckling shapes under compression and shear could also result in mode I opening of a crack tip. The presence of even a small amount of G_I could greatly reduce the capability of the structure to resist crack propagation.

The effectiveness of the fastener under mixed-mode load case was investigated. The mixed-mode load condition was created by applying axial tension to only one of the two beams (figure 39). It should be noted that because of the finite dimensions of the finite element model and large beam-column deformations, while the external load case remained the same, the fracture mode-mixity would change slightly as the crack propagated across the model. Figure 40 shows the applied tension load versus crack-tip location for the 25%-0° and 50%-0° lay-ups with and without a fastener. The crack propagation was only marginally stable without a fastener, as shown by the dotted lines (the lines terminated because the solver failed to converge when crack propagation became unstable). The critical loads for the 25%-0° and 50%-0° lay-ups were approximately 25kN (5.6 kips) and 29kN (6.5 kips), respectively. With the fastener, the propagation load increased

drastically, as shown by the solid lines. The propagation loads for the 25%-0° and 50%-0° lay-ups jumped to 35.6kN (8.0 kips) and 42.0kN (9.4 kips), respectively, at the crack-tip location of 5 mm (0.2 inches). This represented a 42% and 45% increase over the critical loads without a fastener. After the crack tip left the fastener location, crack propagation continued in a stable fashion. In the mixed-mode load case, the propagation load increased in two different stages: a step jump in the immediate vicinity of the fastener and a gradual increase after the crack tip had propagated past the fastener. It is crucial to note that the crack tip was no longer completely arrested under this load case (i.e., the crack could continue to propagate indefinitely as the applied load was increased).

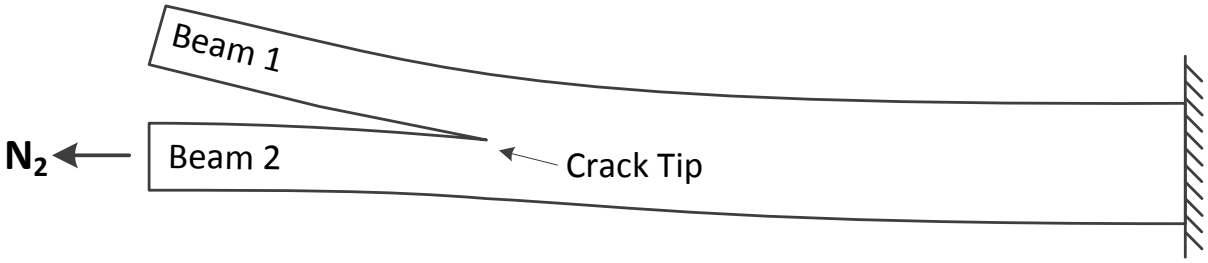

Figure 39. Deformation of a DCB with applied tension on the lower beam [3]

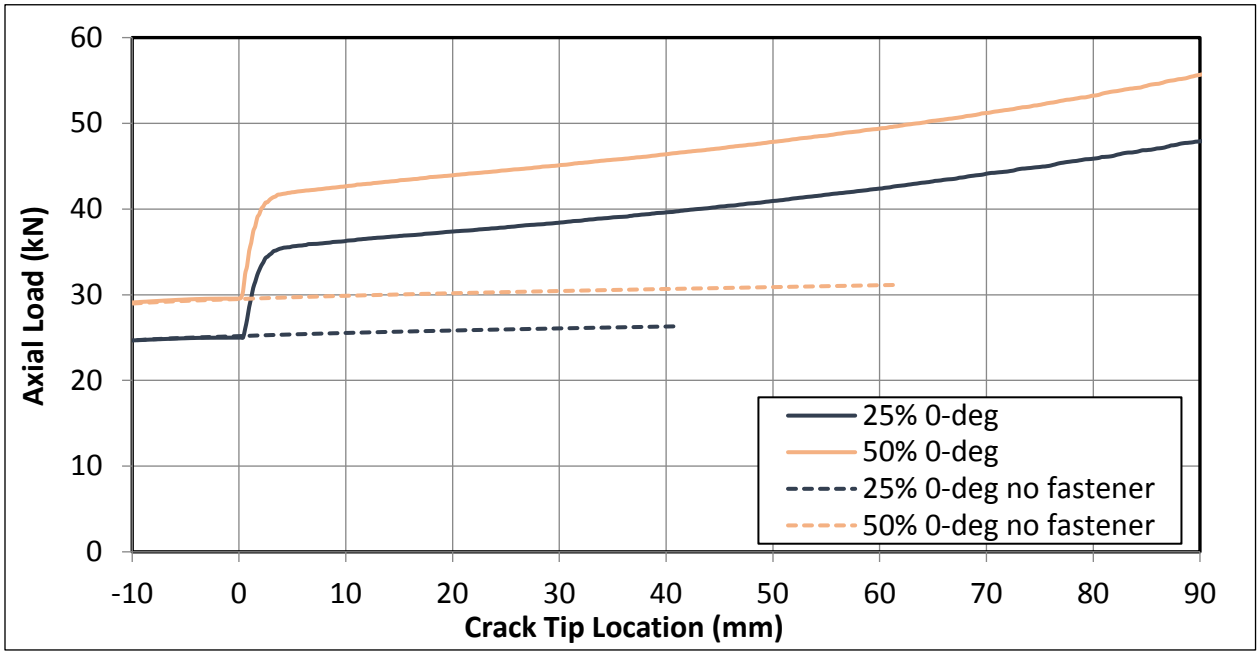

Figure 40. Propagation load vs. crack tip location in mixed-mode [3]

The behavior of the load versus crack-tip location curves in figure 40 implies that two different mechanisms are acting together to provide the overall arrest capability. Figure 41, which shows the SERR components required for propagation versus crack-tip location, effectively illustrates the first mechanism at work—mode I suppression. As the crack propagated past the fastener, the fastener axial stiffness prevented the crack tip from opening. As a result, the mode I strain energy

release rate, G_I, dropped to zero. This forced the crack to propagate in pure mode II. This could be achieved only by increasing the applied load significantly (as shown by the step jumps in propagation loads in figure 41), driving the mode II strain energy release rate, G_{II}, up to G_{IIC} to make up for the loss in G_I. Mode I suppression was effective in providing a large step increase in the propagation load as the crack reached the fastener. The crack appeared to be temporarily arrested. The benefit of suppression was also dependent on the amount of G_I present before the crack tip reached the fastener. If crack propagation was in pure mode II, this mechanism would provide no benefit to crack arrestment, and no step increase in propagation load would be observed.

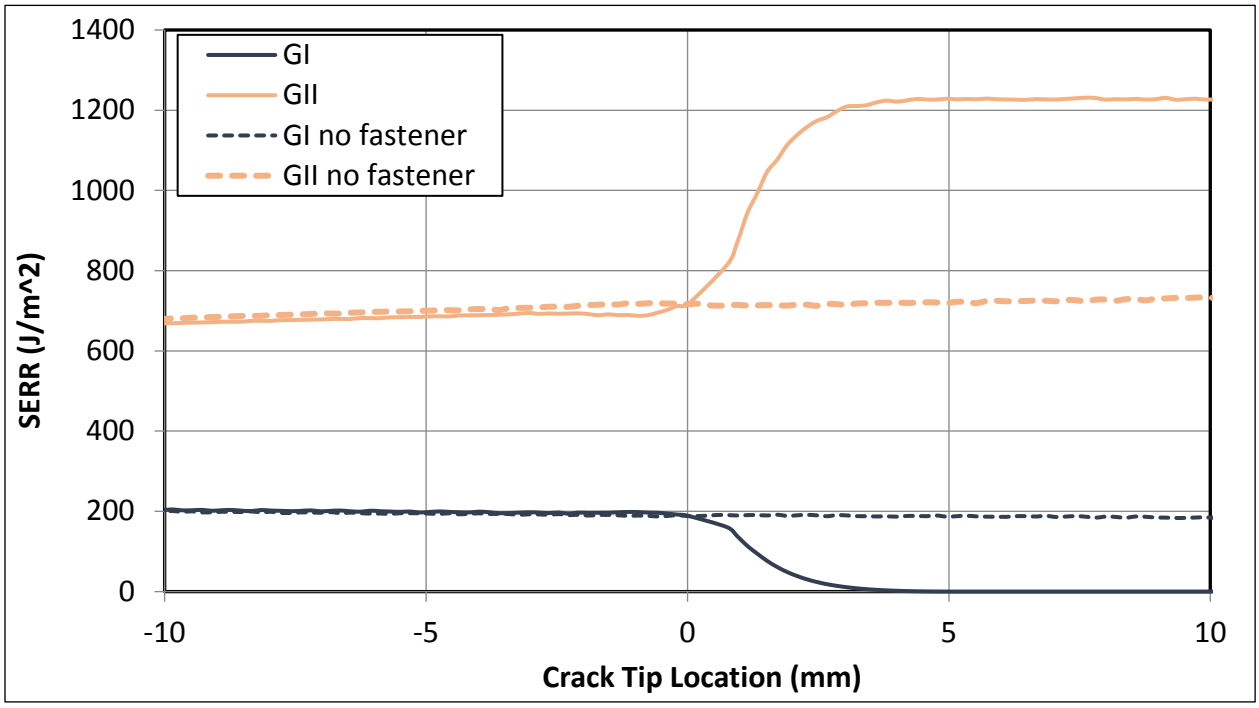

Figure 41. SERR components required for propagation vs. crack-tip location in mixed mode [3]

The second mechanism was the resistance provided by the fastener joint shear stiffness (i.e., fastener flexibility). As the crack separated the intact portion of the beam, the newly formed sublaminates and the fastener formed a fastener joint. The fastener transferred some of the axial load and reduced the loading at the crack tip. The percentage of load transferred by the fastener increased as the crack tip advanced, providing increasing resistance to crack propagation. As a result, crack propagation beyond the fastener remained stable, requiring higher load for further crack growth. The propagation stability provided by the fastener was primarily driven by factors that impacted the fastener flexibility, such as laminate stiffness, laminate thickness, fastener stiffness, and fastener diameter. In general, the stiffer the fastener joint, the more stability was added, and the slope of the load-versus-crack-tip location curve was increased. Although crack propagation was stable, the arresting effect was greatly diminished compared to mode I suppression. Crack propagation was retarded, not arrested, in this regime. Once the crack propagated past the fastener, a relatively small increase in apply load would cause significant crack growth.

3.1.7 Effect of Contact Friction and Fastener Preload Under Mixed-Mode Loading

Crack-face friction has been a persistent issue in specimens designed to measure the mode II critical strain energy release rate (G_{IIC}), such as the ENF specimen. The contact friction behind the crack tip artificially inflates the load required to cause crack propagation, leading to inaccurate measurements of G_{IIC}. However, crack-face friction plays an important and beneficial role in the crack-arrest fastener. The friction of interest is generated by the fastener preload (clamp up), and therefore only acts in the vicinity of the fastener. Fastener preloads in structural assemblies often approach the tensile-yield strength of the fastener, resulting in friction forces orders of magnitude greater than that of unfastened surfaces (e.g., ENF). Therefore, the analysis model must include a realistic portrayal of fastener preload and friction.

To study the effect of friction, the mixed-mode load case was applied to the DCB with 25% 0-deg layup. A constant fastener preload of 16.37kN (3680 lb; 50% of 0.25-inch fastener tensile yield strength) was applied. Typically, a newly installed fastener would have preload of approximately 80% of its tensile yield strength. A lower value of 50% was used to simulate the through-thickness visco-elastic relaxation of the composite laminate. The crack-face static coefficient of friction (μ) was varied from 0–0.75.

Figure 42 shows the applied tension load versus crack-tip location under the above conditions. The curve for the frictionless case (solid dark line) is almost the same as the corresponding curve in figure 40. The jump in propagation load due to fracture mode transition occurred more than 2 mm (0.08 inches) before the crack tip reached the fastener. This was because of the extended influence of the fastener generated by the preload. The peak of the propagation load jump increased in proportion to the coefficient of friction. The load peaks reached 32.9kN, 46.3kN, 55.2kN, and 63.2kN (7.4 kips, 10.4 kips, 12.4 kips, and 14.2 kips) for μ of 0, 0.25, 0.5, and 0.75, respectively. As the crack tip propagated toward the fastener, new cracked surfaces were created and crack-face friction built up behind the crack tip. The friction reduced the force available at the crack tip, leading to the step increases in the propagation load. After the initial jump, the propagation load did not increase smoothly for the cases with non-zero friction. Instead, there were large segments of unstable crack propagations as the crack tip exited the fastener region. For example, in the case in which μ=0.25, the crack tip remained at 1 mm (0.04 inches) up to 46kN (10.3 kips), but propagated to 60 mm (2.4 inches) as soon as the load exceeded 46kN (10.3 kips). The length of the unstable propagation increased with the coefficient of friction. A displacement control analysis was repeated for the μ=0.5 case. The result showed that the propagation load decreased steadily during the unstable propagation despite the stabilizing effect of the fastener shear joint. The propagation load began to recover after the crack tip reached a location of 60 mm (2.4 inches). This implied that the crack-tip driving force was increasing as the crack tip exited the fastener area, whereas the applied load was still the same. This particular observation is discussed in the following section.

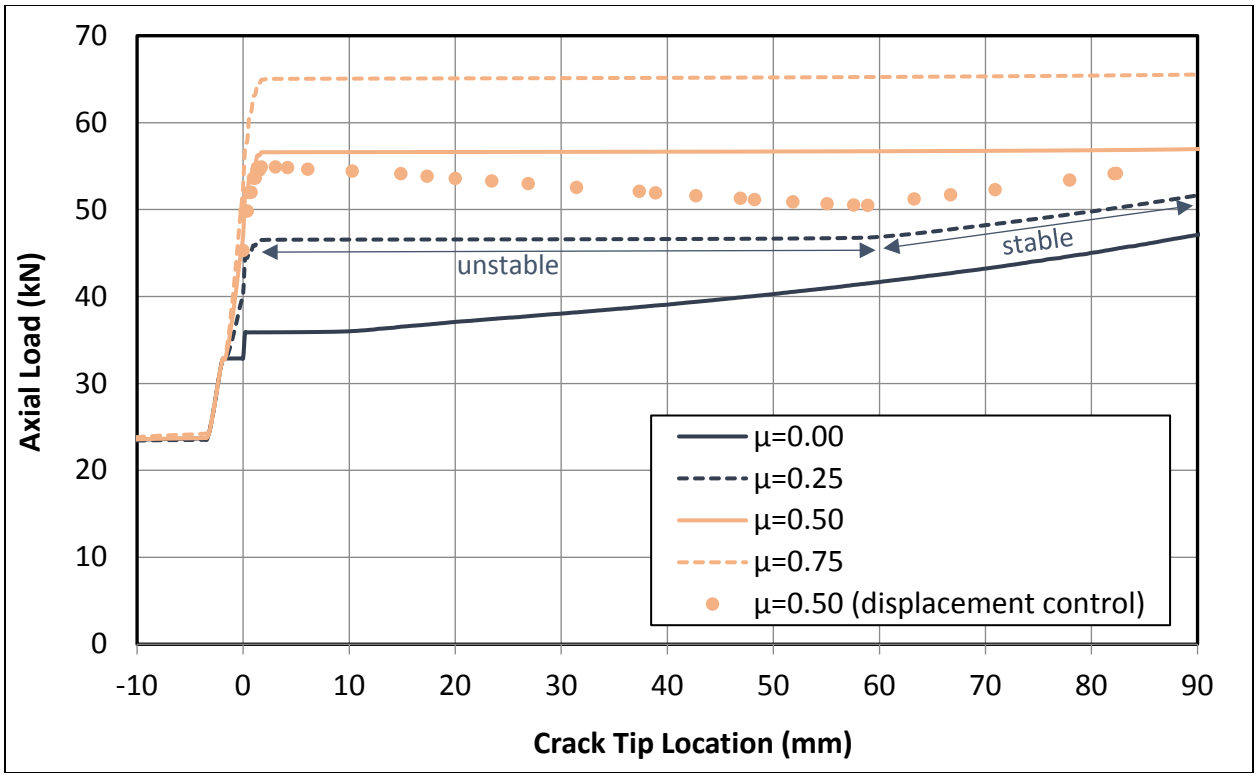

Figure 42. Propagation load vs. crack-tip location in mixed-mode with preload and contact friction [3]

It was expected that the increase in propagation load should simply be twice the friction force, which was the product of the fastener preload and the coefficient of friction. The contact friction subtracted from the axial load of the lower beam while adding the same amount to the upper beam. Therefore, the mode II shearing force at the crack tip (axial force in the lower beam minus the axial force in the upper beam) was reduced by twice the magnitude of the friction force. However, the FEA results indicated that the increase in propagation load was greater than expected. A couple of possible explanations could be offered based on the interaction between the crack-face friction and the crack tip. The crack-face friction due to preload, which could be quite large relative to the axial loads in the beam, caused significant local shear deformation around the cracked surfaces immediately behind the crack tip. This local shearing shielded the crack tip from some of the far-field applied load, providing additional crack-arresting capability. An alternative explanation was that the shear stresses on the cracked surfaces interacted with the crack-tip stress field and reduced its stress intensity, providing protection against crack propagation. However, the shear zone was allowed to interact only with the crack tip when the crack tip was near the fastener. When the crack tip exited the shear zone under the fastener, the interaction effect was lost. The reversal of this temporary arresting effect resulted in the unstable propagations immediately after the crack tip exited the fastener area, as shown in figure 40. Higher crack-face friction resulted in a greater temporary arresting effect, which subsequently led to longer unstable crack propagation. These observations based on FEA were similar to the test observations.

Contact friction and fastener preload played an important role in arresting crack propagation in mode II. The friction provided by this mechanism was significant relative to the applied load

because the fastener preload was very high with the addition of the temporary arresting effect previously described and provided an appreciable crack-arresting capability. It was effective in arresting mode II propagation at the fastener, whereas the fastener joint shear stiffness could only retard crack propagation. Increasing the fastener size would have a direct effect on the ability to apply friction to the crack face. More friction could also be achieved by having multiple fasteners in an array if some delamination between the crack-arrest fasteners could be tolerated.

It is important to note that a fastener with preload could apply large friction forces on the cracked surfaces, whereas other arrest features, such as stitches and z-pins, could not deliver through-thickness compression to generate friction. This effect was significant because a mechanical fastener with high preload could generate friction force comparable to the in-plane loads in the laminates. A significant portion of the total crack arrest capability could be attributed to friction.

3.1.8 Discussion of Main Crack Arrest Mechanisms

The analysis results discussed in this report illustrate three key mechanisms with which a fastener provides crack-arrestment capability. The three mechanisms are identified as 1) mode I suppression by fastener axial stiffness, 2) crack-face friction from fastener preload, and 3) fastener-joint shear stiffness.

Mode I suppression works by mechanically closing the crack tip, thus eliminating the mode I component of a normally mixed-mode crack and forcing the crack to propagate in pure mode II. This requires additional loads to drive up G_{II} to make up for the loss in G_I, arresting the crack propagation in the meantime. This mechanism is effective specifically for laminated composites because of their very low mode I critical energy release rates (G_{IC}) and much higher mode II critical energy release rates (G_{IIC}). In addition, the crack tip is effectively arrested at the fastener location without overrunning the feature. However, the apparent arrest capability depends on the mode mixity of the crack tip and the load case. If crack propagation is pure mode I, the fastener can completely stop the crack. If crack propagation is pure mode II, then no benefit can be realized from eliminating the mode I fracture component. Alternate delamination arrestment features, such as z-pin and stitching, operate under the same principle, but in a more distributed fashion.

Crack face friction from fastener preload works by generating a large amount of friction under the fastener, thus resisting mode II crack propagation. The amount of friction is very high because the fastener preload can be greater than 50% of the fastener tensile yield strength, even after viscoelastic relaxation of the laminate. In addition, the apparent effect of friction is greater when the surface traction interacts with the crack tip. However, this effect reverts itself when the crack tip leaves the fastener, leading to unstable crack propagations. Similar to mode I suppression, most of the benefits from crack-face friction are realized when the crack tip is directly underneath the fastener, effectively arresting the propagation without allowing the crack to overrun the feature. Fasteners have the greatest advantage because of their high preload. Such alternatives as pre-stressed stitches can provide smaller and distributed through-thickness compression, whereas z-pins provide no benefit. However, the coefficient of friction of the cracked surfaces is difficult to quantify and can decrease if the surfaces are allowed to wear out under cyclic loading. Also, the magnitude of fastener preload has high variability and is highly dependent on the installation process.

Fastener-joint shear stiffness works by providing elastic resistance to mode II propagation that retards crack propagation. The retarding effect of joint stiffness is weak, but it stabilizes crack propagation beyond the fastener and prevents catastrophic breakup of the part. Unlike mode I suppression and crack-face friction, which are effective in arresting the crack at the fastener location, fastener joint stiffness can only provide resistance to propagation after the crack tip is past the fastener. Therefore, this is only a crack retardation mechanism. In addition, composite fastener joints tend to be more flexible and are installed with positive fit clearance, making them less effective in resisting crack propagation.

3.1.9 Alternate Failure Modes Not Considered in the Current Analysis

The FEA discussed in this section focuses primarily on the interlaminar fracture of the composite laminate and the behavior of the crack-arrest fastener. Alternate failure modes were not simulated. These alternate failure modes include in-plane (e.g., filled/open-hole tension) and bending failure of the laminate, fastener shear and tension failure (e.g., tensile/shear yield, head pop-off), laminate bearing failure, and fastener head pull-through.

Typically, the interlaminar failure load is much lower than the laminate in-plane failure modes. The crack-arrest fastener should be designed such that its capability meets or exceeds the failure load of the most critical laminate failure mode. This way, the strength capability of the laminate can be efficiently used. Here, the capability of the crack-arrest fastener is loosely defined because it also depends on the acceptable crack propagation beyond the fastener. However, allowing crack propagation beyond the arrest feature adds a lot of difficulties in design and analysis. Once the crack tip overruns a fastener, a new bolted joint is created. Analysis must be conducted on this new detail, which requires developing new loads and performing margin checks for all pertinent failure modes and load cases. Also, allowing the crack to overrun an arrest feature also jeopardizes substantiation to the Title 14 Code of Federal Regulations (CFR) Part 23.573 bonded joint requirement. Therefore, one possible approach is to define the arrest capability as the peak load before the crack tip exits the fastener area. This definition ensures that the crack is arrested at the fastener location, simplifying the analysis of the structure in all other failure modes.

3.2 ANALYTICAL MODELING

The analytical models for three-plate and two-plate specimens both used a beam/bar idealization of each subcomponent. Just as in the FEA, Huth's fastener flexibility was used to calculate the shear spring stiffness, while a constant diameter bar was assumed for the tensile stiffness. Each piece of the laminate was modeled separately and was assumed to behave as a constant area bar/beam to calculate the spring constant of that section.

3.2.1 Mode II Model Design

Figure 43 shows the full analytical model of the three-beam specimen. The origin of the model is located at the center of the fastener. The total load, P, is divided equally to the outer laminates in the free region at $x = -L_2$; for the free region: $x \in [-L_2, 0]$. The crack tip is located at $x = a$; for the cracked region: $x \in [0, a]$. The specimen is fixed at $x = L_1$, at the end of the intact region; for the intact region: $x \in [a, L_1]$.

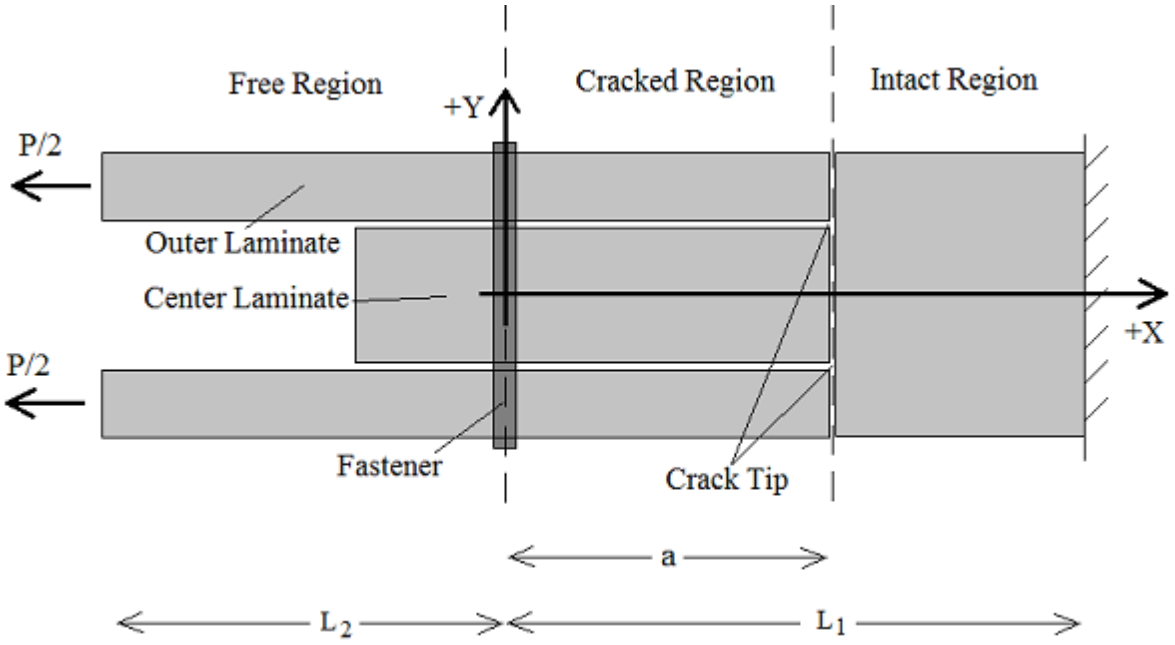

Figure 43. Full analytical model of three-beam specimen [2]

The analytical model is simplified to an idealized model that replaces beams and the fastener with springs. In doing so, the curvatures of the beams are assumed to be zero, the stress/strain distribution at the hole is ignored, and SERR mode decomposition is not considered. Friction within the crack interface is neglected. The idealized model is further simplified into the reduced-idealized model. This is done by considering the symmetry of the model about the *x*-axis. Figure 44 shows the full-idealized and the reduced-idealized analytical models.

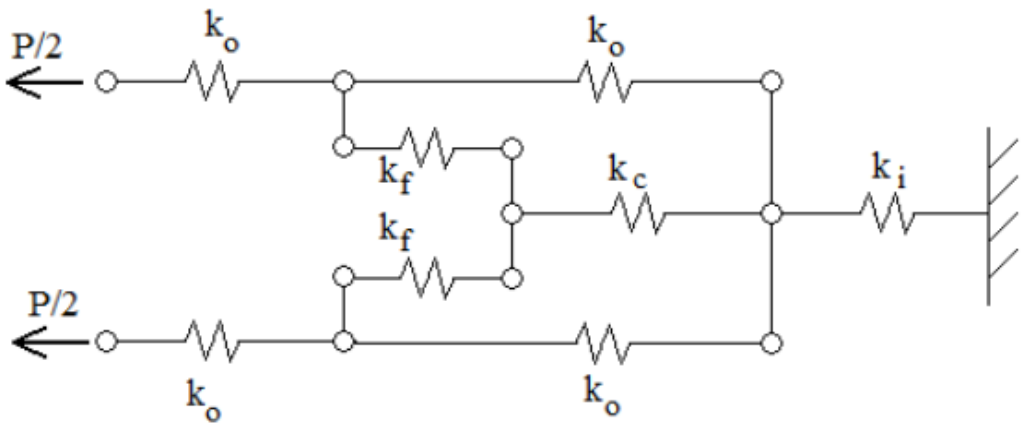

(a) Full idealized model

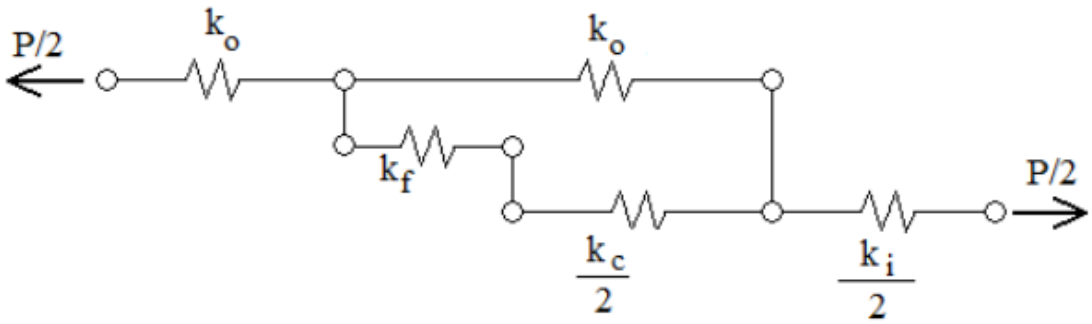

(b) Reduced idealized model

Figure 44. (a) Full three-plate model and (b) reduction [2]

Using the above representation of the model, a closed form solution is derived that solves for the load at which cracks propagate, P_C, for an arbitrary crack length, a, as a function of laminate and fastener properties. For the derivation, first the fastener compliance, C_f, is determined, then the load transferred by the fastener, P_f, is solved; last, the solution to P_C is derived.

The fastener compliance, C_f, is determined as described in [11]. From compliance, the stiffness is simply obtained from equation 3:

$$k_f = \frac{1}{C_f} \tag{3}$$

The total fastener compliance is determined by considering the sum of the individual effects of fastener shearing, C_{fs}, fastener bending, C_{fb}, fastener bearing, C_{fbr}, and plate bearing, C_{pbr}, during

the fastener load transfer. Equations 4–7 show the expressions for C_{fs}, C_{fb}, C_{fbr}, and C_{pbr}, respectively.

$$C_{f_s} = \frac{2t_0 + t_c}{2G_f A_f} \tag{4}$$

$$C_{f_b} = \frac{8t_0^3 + 16t_0^2 t_c + 8t_0 t_c^2 + t_c^3}{192E_f I_f} \tag{5}$$

$$C_{fbr} = \frac{2t_0 + t_c}{t_0 t_c E_f} \tag{6}$$

$$C_{pbr} = \frac{1}{t_0 E_{x_0}} + \frac{2}{t_c E_{x_c}} \tag{7}$$

The total fastener compliance C_f is the sum of the four individual compliance components, as shown in equation 8:

$$C_f = C_{fs} + C_{fb} + C_{fbr} + C_{pbr} \tag{8}$$

Substituting equations 4–7 into equation 8 results in the full expression for the fastener compliance, shown in equation 9. It can be seen that the fastener compliance is a function of geometric and material properties of the fastener, outer laminate, and center laminate.

$$C_f = \frac{2t_0 + t_c}{2G_f A_f} + \frac{8t_0^3 + 16t_0^2 t_c + 8t_0 t_c^2 + t_c^3}{192E_f I_f} + \frac{2t_0 + t_c}{t_0 t_c E_f} + \frac{1}{t_0 E_{x_0}} + \frac{2}{t_c E_{x_c}} \tag{9}$$

For the solution to the fastener transfer load, P_f, refer to the reduced analytical model that is shown in figure 44. The first step is to solve for the equivalent stiffness of the center laminate and fastener, $k_{eq\ cf}$, and the equivalent stiffness of the outer laminate, center laminate, and fastener, $k_{eq\ ocf}$, as shown in equations 10 and 11, respectively.

$$K_{eq\ cf} = \left[\frac{1}{K_{cc}} + \frac{1}{K_f} \right]^{-1} \tag{10}$$

$$K_{eq\ ocf} = K_{oc} + \left[\frac{1}{K_{cc}} + \frac{1}{k_f} \right]^{-1} \tag{11}$$

Next, Hooke's Law, for a spring, is used to solve for the displacement, x, of the equivalent spring due to the applied load, P/2. This is shown in equation 12:

$$x = \frac{\frac{P}{2}}{K_{eq\ ocf}} \tag{12}$$

The fastener transfer load, P_f, can be determined by substituting equations 10–12 into the expression for Hooke's Law for a spring.

The analytical solution is then derived directly from the definition of the strain energy release rate, G, as shown in equation 13:

$$G = \frac{\partial U_{total}}{\partial a} \tag{13}$$

in which U_{total} is the total energy of the reduced idealized model and is determined from the summation of the energies of the individual components that make up the model. Because each component of the model is analyzed as a spring, the energy of each component can be solved from the definition of the potential energy of a linear spring with a constant applied load, as described in equation 14:

$$U_{spring} = \frac{1}{2} kP^2 \tag{14}$$

The total potential energy of the system is the sum of the potential energies of each component, which is treated as a spring. It is necessary to determine the stiffness, k, of each laminate component. The stiffness can be easily determined from the stiffness expression for a bar or truss member.

$$k_j = E_{x_j} A_j / L_j \tag{15}$$

Substituting the stiffness expressions into the corresponding energy expression, summing, and taking the derivative of the total energy with respect to the crack length, *a*, results in an expression for the mode II SERR, G_{II}, as shown in equation 16:

$$G_{II} = P^2 \left[-\frac{2\left(aA_c E_c + 2aA_0 E_0 + A_c A_0 C_f E_C E_0\right)^2}{8A_i \left(aA_c E_c + 2aA_0 E_0 + A_c A_0 C_f E_c E_0\right)^2 E_i} + \frac{A_i \left(2a^2 A_c E_c + A_0 \left(2a + A_c C_f E_C^2 E_0\right) E_i\right)}{8A_i \left(aA_c E_c + 2aA_0 E_0 + A_c A_o C_f E_C E_0\right)^2 E_i} \right] \tag{16}$$

Substituting the critical mode II SERR, G_{IIC}, into equation 16 and solving for *P* gives an expression for the critical load, P_C, at which crack propagation will occur in the three-beam model with an arbitrary crack length. Equation 17 shows this final expression:

$$P_c = \sqrt{G_{IIC}}\left[-\frac{2\left(aA_cE_c + 2aA_0E_0 + A_cA_0C_fE_cE_0\right)^2}{8A_i\left(aA_cE_c + 2aA_0E_0 + A_cA_0C_fE_cE_0\right)^2E_i} + \ldots + \frac{A_i\left(2a^2A_cE_c + A_0\left(2a + A_cC_fE_c\right)^2E_0\right)E_i}{8A_i\left(aA_cE_c + 2aA_0E_0 + A_cA_0C_fE_cE_0\right)^2E_i}\right]^{-\frac{1}{2}} \quad (17)$$

3.2.2 Mode II Modeling Results

The analytical solution was verified by using the finite element model that was previously described for various G_{IIC} values. The lamina properties and fastener properties that were used in the finite element model are listed in table 9. These are the same properties used in the analytical model. G_{IIC} was varied from 7.0 to 20 lb/in. Classical lamination theory was used to calculate laminate stiffness values for the analytical model.

The analytical solution was run in MATLAB®. The curves were produced by solving for P_C at a given crack length, a, then allowing the crack length to increase by a small amount (simulation of growing crack) and solving for the new load, P_C, for which the crack propagated again. Figure 45 shows the comparison of the analytical model and finite element model for critical SERR values of 7.0, 14.0, and 20.0 in-lb/in^2. In the plot, the crack starts at x = -0.25 inches, which is where unstable crack growth occurs, characterized by a horizontal slope. Cracks reach the fastener at x = 0 and are stabilized. A more positive slope indicates greater crack stability. The crack-growth simulation is taken to 5.0 inches past the fastener. The FEM was run using plane-strain elements, whereas the analytical model was formulated using a plane-stress approach. The analytical model was modified, as described in equation 18, to convert it from plane-stress to plane-strain:

$$E_{x\ plane-strain} = \frac{E_{x\ plane-stress}}{1-\nu_{xy}\nu_{yx}} \quad (18)$$

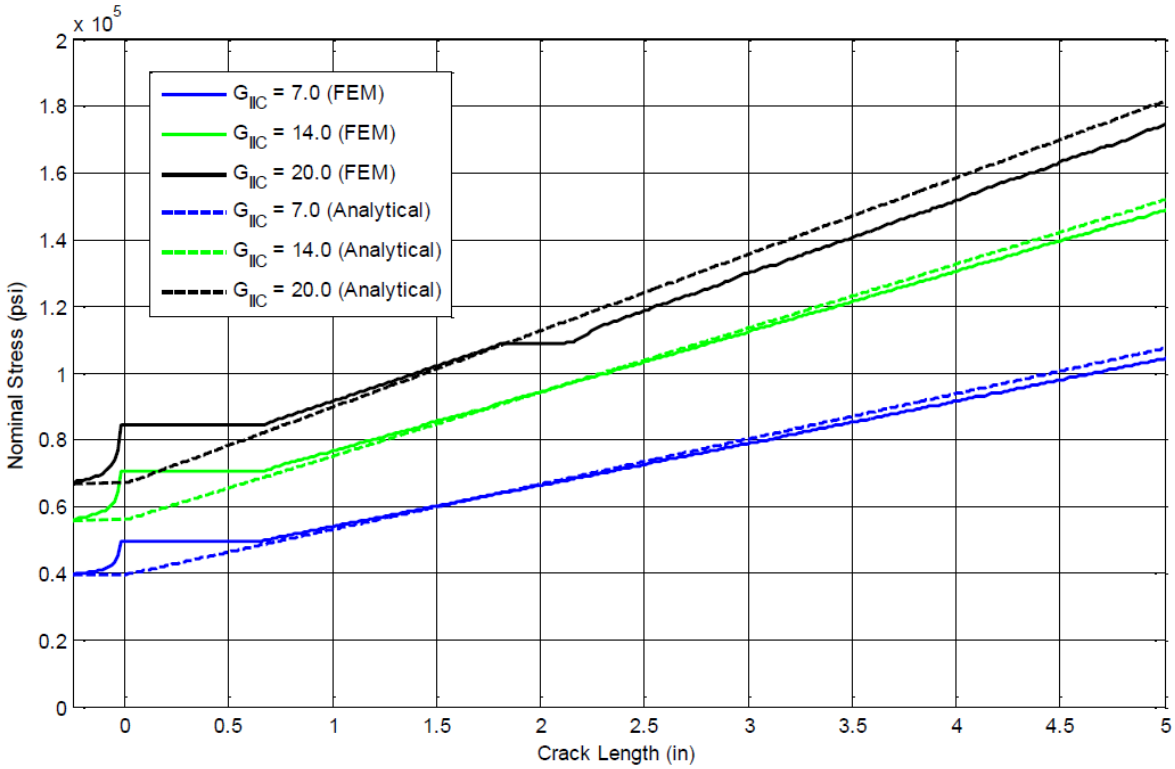

Figure 45. Pure mode II analytical vs. FEM results [2]

In figure 45, the analytical model and FEM agree very well. For the simulations, no failure modes other than crack propagation were considered. The graph shows the applied nominal stress (*y*-axis) versus crack length (*x*-axis). A steeper curve indicates more stable crack growth, and a horizontal curve indicates unstable crack growth. The slopes of the curves are very close, but the FEM curves are slightly less steep. The reason for this was the FEM used two-dimensional elements, while the analytical model was one-dimensional. This allowed shear deformation of the FEM near the crack tip, which slightly relaxed the load applied to the crack tip.

Some important notes on the FEM results follow. The portion of the FEM plots from $x \in$ [-0.25 inches, 0.5 inches] that curve up then go horizontal are a byproduct of the FEM numerical solver and should actually follow a continuous path similar to the analytical model. For the case of G_{IIC} = 20 in-lb/in^2, the short horizontal jump was caused by unsymmetrical crack propagation, in which one crack jumped ahead of the other, then both continued in unsymmetrical propagation.

3.2.3 Mixed-Mode Model Development

The analytical model resembles the split-beam configuration of the FE model (figure 46). The model simulated the crack-propagation behavior in a split beam by dividing it into cracked and non-cracked segments. The non-cracked beam between the fixed boundary and the crack tip was referred to as the intact segment. The cracked beams between the crack tip and the fastener were referred to as the cracked segments. Crack length of interest was defined as the distance from the crack tip to the fastener only, or the crack-tip location with respect to the fastener. The cracked

beams between the fastener and the far-field, where loads and moments were applied, were referred to as the freed segments. Segmentation of the model was necessary because the crack tip and the fastener represented discontinuities in the structure. Therefore, the behavior of each beam could not be described using a single displacement function. For identification purposes in figure 46, the upper beam is referred as Beam 1 and the lower beam is Beam 2.

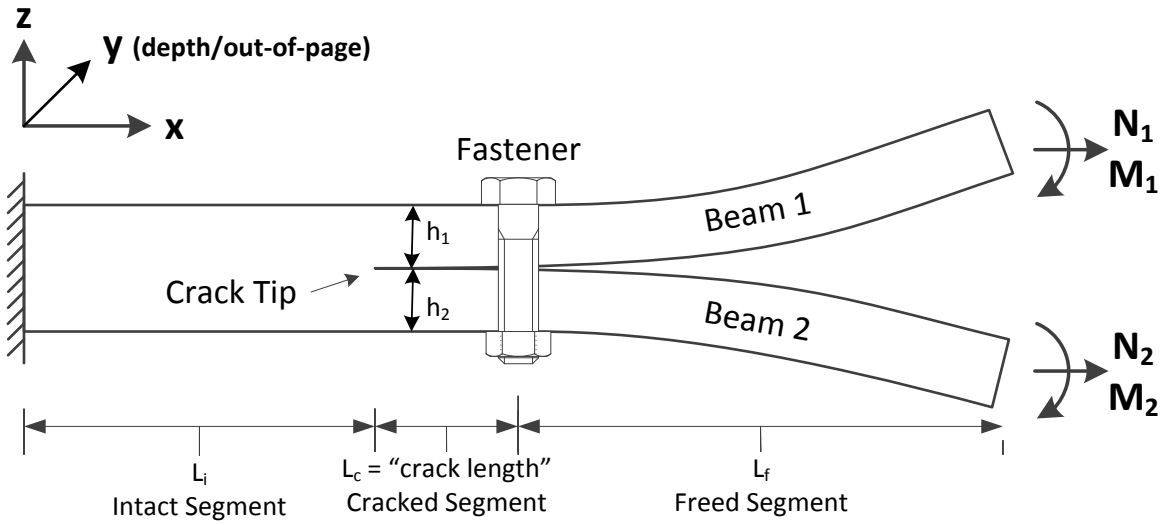

Figure 46. Schematic of analytical model [3]

The model was decomposed into a total of five beam-column elements. Two springs, representing the fastener axial stiffness and the joint shear stiffness, were attached to the junctions between the cracked beam segments and the freed beam segments. Figures 47 and 48 provide a simplified depiction of the connection and interaction between these beam-column elements and springs in deflection and axial displacement. The orientation used is such that positive *x*-direction is to the right, and positive *z*-direction is to the top. The forces and moments sign convention were such that positive axial load (*N*) resulted in axial tension or positive *x*-displacement, and positive moment (*M*) created clockwise bending or deflection in the negative *z*-direction.

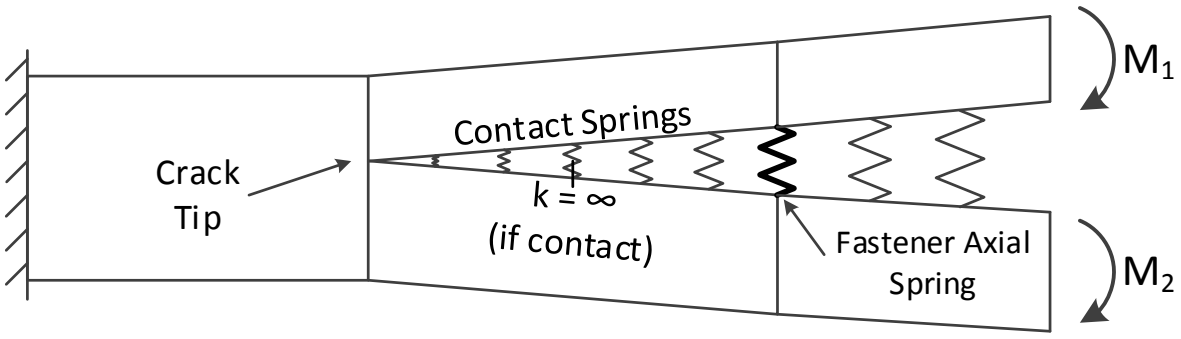

Figure 47. Beam-column model—deflection and interactions in the *z*-direction [3]

Make contact springs 0.75 pt thick.

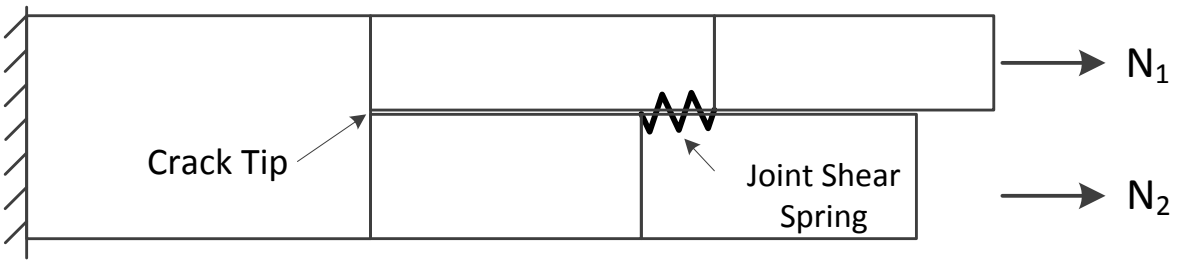

Figure 48. Beam-column model—deflection and interactions in the *x*-direction [3]

Details of the beam-column connectivity are discussed here. The intact beam, representing the full thickness of the laminate, was given fixed boundary conditions at the left end. Zero *x*-*z* displacements and slope were enforced. The left ends of the cracked segments of beam 1 and beam 2 were attached to the right end of the intact beam. The attachment was accomplished by using stiff springs ($k \rightarrow \infty$) that enforced equal *x*-*z* displacements and slope at the connection. The freed segments of beam 1 and beam 2 were attached to the cracked segments of beam 1 and beam 2, respectively, using stiff springs. Although the freed segments were not directly involved in the simulation of crack propagation, they were needed to resolve the beam-column effect between the fastener and the far-field boundary conditions. Contact springs in the *z*-direction were distributed along the length of the cracked and freed segments of the beams to resolve contact interactions and forces. The contact spring was either stiff or had zero stiffness, depending on its contact state. The individual contact spring was activated when local penetration between beam 1 and beam 2 was detected. The on/off states of the contact springs must be determined iteratively. Friction between the cracked beams due to contact normal forces was not modeled because it was negligible compared to the friction force generated by fastener preload. Friction generated by fastener preload, which is technically also a contact normal force but only occurs at the fastener location, was accounted for in the fastener joint modeling.

The fastener was modeled as two springs representing the fastener axial stiffness and the joint shear stiffness. The fastener axial stiffness was given by $AE/(h_1+h_2)$. The joint shear stiffness was obtained using the fastener flexibility approach. The sense and the magnitude of the joint moment could be correctly modeled by attaching the springs to the lower surface of beam 1 and the upper surface of beam 2. As such, the sliding displacement that determined the joint load was calculated at the crack interface, not at the midplane of the cracked beams.

Fastener preload was modeled by offsetting the force-displacement curve of the fastener axial spring by the amount of the preload, as shown in figure 49. Penetration due to preload pulling the beams through each other was prevented by the activation of the contact springs at the fastener location. Typical preload could be as much as 75%–90% of the fastener tensile yield strength at the time of installation. However, composite laminates' viscoelastically relaxed over time under high through-thickness compression. Therefore, 50% of tensile yield strength was a reasonable approximation for analysis purposes.

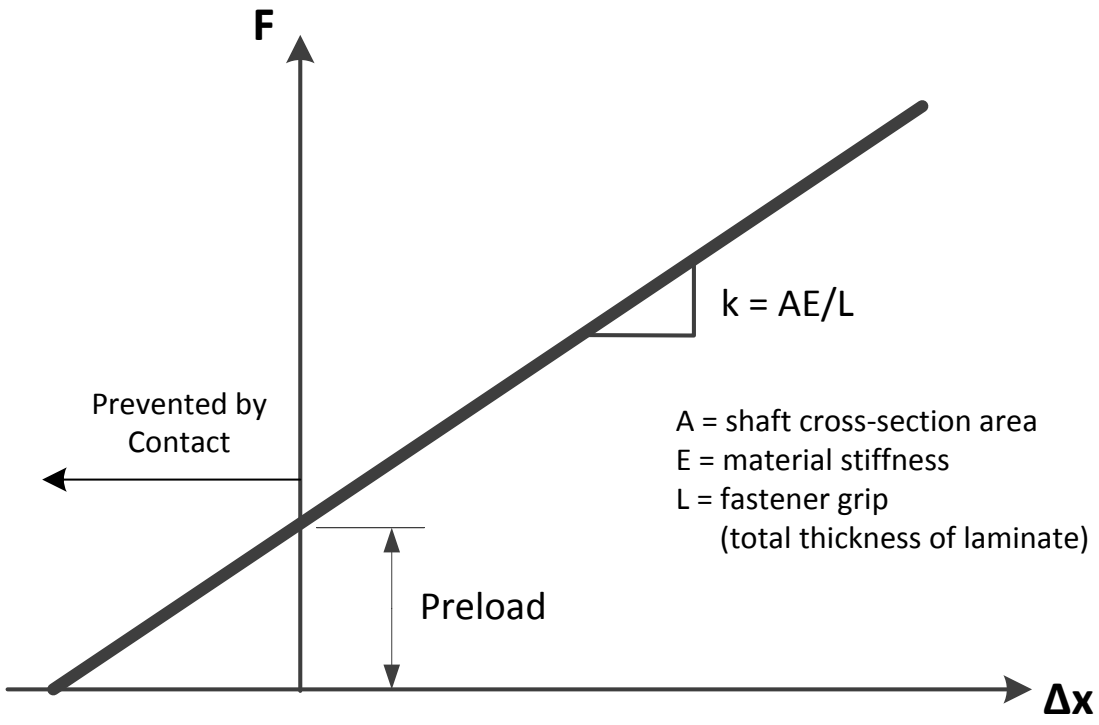

Figure 49. Fastener preload modeling [3]

The effects of crack-face friction generated by the fastener preload and the effect of fastener hole clearance (free-play) were modeled using a nonlinear force-displacement curve for the joint shear spring, as shown in figure 50. The nominal fastener joint stiffness was assumed linear and was calculated using fastener flexibility approach. The fastener hole clearance was given as a constant amount of displacement, usually as a manufacturing/assembly specification. The fastener joint did not transfer shear load through the fastener shaft unless the sliding displacement exceeded the hole clearance. The crack-face friction was calculated as the product of the fastener preload and a crack-face coefficient of friction. A pristine-interface coefficient of friction should be used to represent structures in static tests whereas a worn-out coefficient of friction should be used to simulate the effect of crack face wearing under cyclic loads. If the load transferred through the joint was at or below the friction limit, the cracked surfaces were locked. Joint total shear load and moment were non-zero, but the sliding displacement and the load transferred through the shaft was zero. In this regime, the joint shear stiffness was assumed to be infinite. When the load transferred through the joint exceeded the friction limit, the joint had to first slip for the amount equal to the fastener-hole clearance (e.g., the horizontal segment in figure 50) without additional resistance. The slip did not stop midway on the horizontal line because the joint would slide all the way to the knee of the curve as soon as slipping occurs. The slip was arrested when the fastener shaft engaged the hole and began to transfer load via fastener bolt shear, after which the joint behaved linearly. It should be noted that the static-friction limit was the minimum of the product of the coefficient of friction and preload, and the surface shear strength of the abrading crack faces. For simplicity, surface shear strength of the abrading material was not modeled.

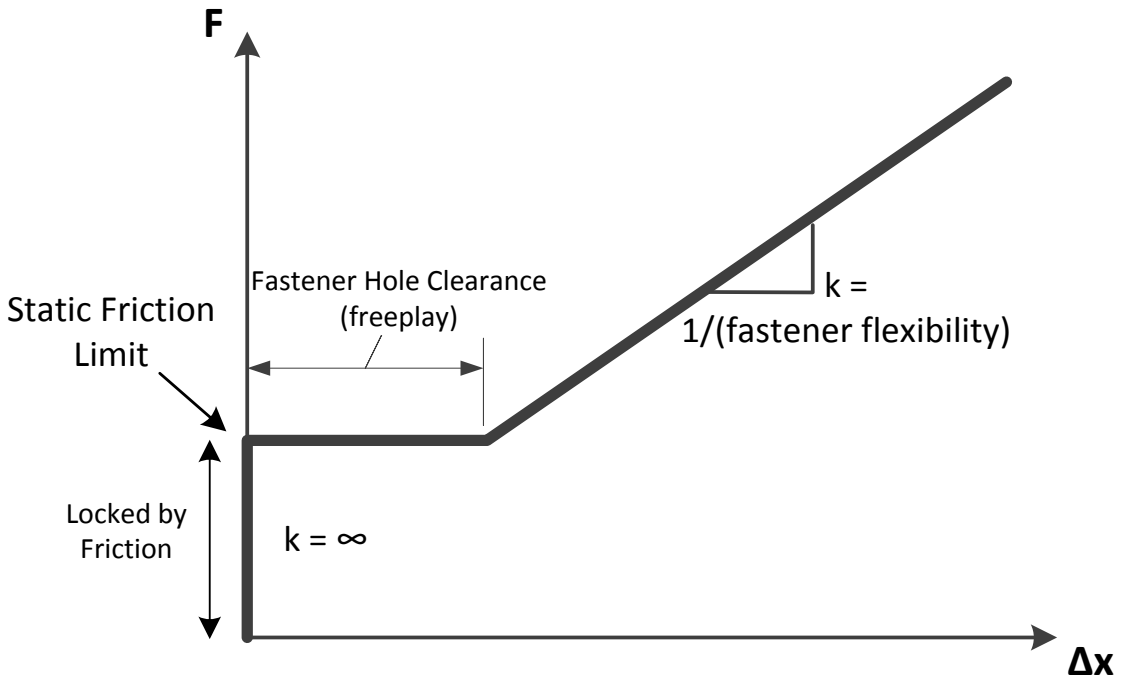

Figure 50. Fastener-preload friction and hole-clearance modeling [3]

A few simplifications, idealizations, and assumptions were made as part of the analytical model. A short summary follows:

- The use of the Rayleigh-Ritz method and predefined displacement functions meant that the solution obtained was an approximation of the actual solution. Similarly, the contact resolution algorithm could only provide an approximate solution of the contact state. It was possible to have chattering nonconvergence, partly because of the artificial stiffness assumed between the beams.
- The beam material and fastener material properties were assumed to be linear. The assumption that the laminate elastic properties were linear to failure was valid in most circumstances if there was no additional damage other than the primary delamination. The fastener-joint shear stiffness was assumed to be linear for simplicity (except for the modeling of friction and hole clearance). Although this assumption was generally good for low load/strain scenarios, it was reasonable to expect nonlinearities at high loads because of fastener-hole elongation and local bearing crushing. The nonlinear joint behavior was evident in the data presented in Huth's fastener flexibility study [11].
- The laminates were modeled using classical beam-column (i.e., zeroth order or shear non-deformable). Transverse shear deformation was neglected. Inaccuracies might arise in scenarios in which transverse shear and shear lag effects were large compared to beam bending deformation. In addition, local transverse shear could directly interact with the crack tip, which could not be captured in the current beam-column and crack-tip element model. The use of the plane strain formulation implied that the structure has no strain/curvature in the depth dimension (*y*-direction).

The principle of minimum potential energy (PMPE) was used to determine the static equilibrium of the beam-fastener system. The principle states that the total potential energy, Π, expressed as a function of the displacement, attains a minimum value at the correct displacement. At the minimum-energy state, the variation of Π with respect to displacement is zero, or $\delta\Pi=0$, in which δ is a small variation. The total potential energy of the system can be expressed as the strain energy, *U*, less the work potential, *W*. The PMPE can be written as in equation 19:

$$\delta\Pi = \delta U - \delta W = 0 \tag{19}$$

In practice, PMPE was used to obtain an approximation of the exact solution because the analytical description of the exact displacement field *w(x)* was unavailable a priori, or infeasible to compute. Therefore, the assumed function $\psi(x)$ for the displacement was used to approximate the exact displacements *w(x)* of the system, from which the best estimate solution for displacement was obtained. However, with a well-understood system, well-selected generic shape functions with enough higher order terms satisfying completeness could provide a solution with sufficient accuracy. In this study, sixth-degree polynomials and second-degree polynomials were used as shape functions for the out-of-plane displacement and axial displacement, respectively.

The Rayleigh-Ritz method was employed to determine the approximate solution of the system based on the PMPE. The displacements of the system $\psi(x)$ are expressed as a linear superposition of N unknown coefficients, β_i, multiplied by N known assumed shape functions, $\phi_i(x)$, which must satisfy the geometric boundary conditions, that is, $\psi(x)=\sum_{i=1}^{i=N}\phi_i(x)\beta_i$. Expressions for the strain energy and the work potential were obtained based on the assumed displacements. Finally, the total potential energy, Π, in the structure could be expressed in terms of the N coefficients, β_i. The solution could then be obtained by taking $\delta\Pi=0$ in equation 20 from which the unknown constants β_i were determined by solving *N* by *N* algebraic equations.

$$\frac{\partial\Pi}{\partial\beta_i}=0, \quad \text{where i} = 1,.....,N. \tag{20}$$

The model was nonlinear because of contact interactions, friction, and hole clearance, so a "guess solution" was obtained each time the set of linear equations was solved. The converged solution was found using an iterative process described below.

First, the displacement shape functions were established for the beam-column elements in the model. Simple polynomials were used because they satisfied the geometric boundary conditions and were well-behaved with localized contacts. (Trigonometric series were found to be not suitable with contact modeling because of the undulating nature of the functions.) The general form for out-of-plane deflection at the midplane of the beam-column is given in equation 21, in which the deflection of the i^{th} beam as a function of *x*, $w_i(x)$, is expressed as a polynomial of degree *j*. The unknown coefficients β are members of ψ in equation 20. For a classical beam, only a third-degree polynomial is required to capture the deformation under simple load cases. For a beam-column, the degree of polynomial required is at least 5 for combined axial-bending load cases. Higher

degree polynomials are recommended to accommodate contact interactions. A sensitivity study was conducted to determine the degree of polynomial needed to provide accurate solutions to the problem in this research. For the beam-column element attached to the fixed end at x=0, the corresponding $\beta_{i,0}$ and $\beta_{i,1}$ terms are set to zero to comply with the geometric boundary conditions.

$$w_i(x) = \sum_{j=0}^{n} \beta_{i,j} x^j \tag{21}$$

The general expressions for axial deformation at the midplane are given in equation 22, in which the displacement of the ith truss as a function of x, $u_i(x)$, is expressed as a polynomial of degree k. The unknown coefficients α are members of ψ in equation 20. Because the extension-bending coupling in a general composite laminate relates the strain (du_i/dx) and curvature (d^2w_i/dx^2), the axial displacement function should have a degree of $k = j - 1$. However, the effects of higher order terms (second and above) in the axial displacement function are negligible. For the truss element attached to the fixed boundary at x=0, the corresponding $\alpha_{i,0}$ term is set to zero to comply with the geometric boundary condition.

$$u_i(x) = \sum_{k=0}^{n} \alpha_{i,k} x^k \tag{22}$$

Using classical beam theory, the axial displacement field of any point in a beam element can be approximated in equation 23, in which $w(x)$ is the bending deflection, and z is the offset from the beam midplane.

$$u(x,z) = u(x) - z\frac{dw(x)}{dx} \tag{23}$$

It follows that the strain field can be given in equation 24, in which $\varepsilon(x)$ and $\kappa(x)$ are the strain and curvature at the midplane as a function of x, respectively.

$$\varepsilon(x,z) = \frac{du(x)}{dx} - z\frac{d^2w(x)}{dx^2} = \varepsilon(x) + z\kappa(x) \tag{24}$$

The strain energy of a 1-D beam from location L_1 to L_2 with width b can be determined by evaluating the area under the stress-strain curve, shown in equation 25.

$$U = \frac{1}{2} b \int_{L_1}^{L_2} \sigma\varepsilon \, dx \tag{25}$$

The stress-strain relations for a general composite laminate based on classical lamination theory can be written as equations 26 and 27. The A and D terms represent the in-plane and bending stiffness of the beam, and B is the coupling term between in-plane extension and bending. The thermal load/moment (N_T and M_T) terms are used to account for internal thermal stresses in the laminate because of the difference between curing and operating temperatures.

$$\begin{Bmatrix} N+N_T \\ M+M_T \end{Bmatrix} = \begin{bmatrix} A & B \\ B & D \end{bmatrix} \begin{Bmatrix} \varepsilon \\ \kappa \end{Bmatrix} \tag{26}$$

$$\begin{Bmatrix} \varepsilon \\ \kappa \end{Bmatrix} = \begin{bmatrix} a & b \\ b^T & d \end{bmatrix} \begin{Bmatrix} N+N_T \\ M+M_T \end{Bmatrix} \tag{27}$$

Substituting the stress-strain relations into equation 25 yields a coupled energy expression, shown in equation 28.

$$U = \frac{1}{2} b \int_{L_1}^{L_2} \begin{Bmatrix} \varepsilon & \kappa \end{Bmatrix} \begin{bmatrix} \mathrm{A} & \mathrm{B} \\ \mathrm{B} & \mathrm{D} \end{bmatrix} \begin{Bmatrix} \varepsilon \\ \kappa \end{Bmatrix} dx + b \int_{L_1}^{L_2} \begin{Bmatrix} \varepsilon & \kappa \end{Bmatrix} \begin{Bmatrix} N_T \\ M_T \end{Bmatrix} dx \tag{28}$$

Expanding the expression above yields the set of equations 29 accounting for the strain energies in extension and bending.

$$\begin{aligned} U_{extension} &= \frac{1}{2} b \int_{L_1}^{L_2} \left(\varepsilon^2 A + \varepsilon \kappa B \right) dx + b \int_{L_1}^{L_2} \varepsilon N_T \; dx \\ U_{bending} &= \frac{1}{2} b \int_{L_1}^{L_2} \left(\varepsilon \kappa B + \kappa^2 D \right) dx + b \int_{L_1}^{L_2} \kappa M_T \; dx \end{aligned} \tag{29}$$

The strain energy corresponding to the beam-column effect is given in equation 30, in which N is the axial force in the beam-column element. The axial forces in the cracked segment are modified by the fastener joint load. The joint-load value used in equation 30 is a guessed value because the joint load could only be determined iteratively. The solution is converged when the guess value is equal to the resultant joint load calculated from the displacement solution.

$$U_{beam-column} = \frac{1}{2} \left(N \pm total\ joint\ load \right) \int_{L_1}^{L_2} \left(\frac{dw}{dx} \right)^2 dx \tag{30}$$

The connection between the beam-column elements is approximated by connecting the beam-column elements with stiff springs that tie the deflections and slopes at the connecting ends. The energy terms corresponding to the springs are given in equations 31 and 32, in which k_∞ is the stiffness of the connecting springs and the beam-column elements, w_1 and w_2, are connected at location $x=L$. The stiffness of the stiff springs must be very high relative to the stiffness of the elements to approximate the tie conditions. In practice, k_∞ should be made as high as possible without causing numerical error. A secondary benefit of using springs as connecting elements, as opposed to exact analytical constraints, is that the forces and moments acting at the joints can be readily calculated. It should be noted that a real crack tip is flexible and is allowed to rotate. Therefore, using k_∞ at crack tip tie connections will make the joint slightly stiff.

$$U_{deflection\_tie} = \frac{1}{2} k_\infty \left(w_1 - w_2 \right)^2 \Big|_{x=L} \tag{31}$$

$$U_{slope\_tie} = \frac{1}{2} k_{\infty} \left(\frac{dw_1}{dx} - \frac{w_2}{dx} \right)^2 \Bigg|_{x=L} \tag{32}$$

Similarly, the truss elements are connected by applying equal displacement condition at the connecting ends, approximated by stiff springs. The energy expression for the connecting springs is given in equation 33.

$$U_{extension\_tie} = \frac{1}{2} k_{\infty} \left(u_1 - u_2 \right)^2 \Big|_{x=L} \tag{33}$$

As discussed previously, the beams in the cracked segment and the intact segment, connected at $x=L_i$, have relative offsets in their midplanes. To connect the elements accounting for the offset, the energy expressions are given in equations 34 and 35. The thickness of the upper and lower cracked beam are h_1 and h_2, respectively. This offset does not affect the bending expressions.

$$U_{extension\_tie,upper-to-intact} = \frac{1}{2} k_{\infty} \left[\left(u_{intact} - \frac{h_2}{2} \frac{dw_{intact}}{dx} \right) - u_1 \right]^2 \Bigg|_{x=L_i} \tag{34}$$

$$U_{extension\_tie,lower-to-intact} = \frac{1}{2} k_{\infty} \left[\left(u_{intact} - \frac{h_1}{2} \frac{dw_{intact}}{dx} \right) - u_2 \right]^2 \Bigg|_{x=L_i} \tag{35}$$

The model consisted of a pair of split beams and their interactions were resolved using contact springs. Under certain load cases, partial or complete penetration of the beam-columns could occur. While such a condition was physically inadmissible, the PMPE approach indiscriminately provided a solution. Therefore, a contact algorithm was incorporated to resolve the contact interactions between the surfaces of the beam-columns. The contact was approximated by an array of stiff springs that were placed along the lengths of the interacting beam-column elements. Each spring was interference activated (i.e., they had very high stiffness only when penetration was detected and zero stiffness when there was no penetration). The high stiffness of the springs limited the penetration to a very small magnitude. Because the exact location(s) of contact could not be determined ahead of time, the resolution of contact state must be performed iteratively for each configuration and load case. It was assumed that at any location L, the contact closure was the same as the difference between the beam deflections at their midplanes at $x=L$. The energy term corresponding to each contact spring is given in equation 36, in which the variable $\delta_{contact}$ is either 0 or 1, depending on the contact condition of the given location.

$$U_{contact} = \frac{1}{2} k_{\infty} \left(w_1 - w_2 \right)^2 \Big|_{x=L} \cdot \delta_{contact} \Big|_{x=L} \qquad \text{,where } \delta_{contact} = \begin{cases} 1 & \text{if } \left(w_1 - w_2 \right) \geq 0 \\ 0 & \text{if } \left(w_1 - w_2 \right) < 0 \end{cases} \tag{36}$$

The fastener is modeled with two springs, and their energy expressions are given below as equations 37 and 38. The fastener is located at $x=L_i+L_c$, according to figure 46. Both equations capture the area under the force-displacement curves shown in figures 49 and 50. For fastener

tension, the spring stiffness is calculated by AE/L, in which A is the shaft cross-section area and L is the fastener grip length, or (h_1+h_2). For fastener shear, the spring stiffness is calculated using the fastener flexibility approach. However, if the fastener joint load is less than the friction limit, the shear spring stiffness is set to k_∞ to simulate frictionally locked surfaces. In addition, $\delta_{hole\ clearance}$ and the friction term are omitted.

$$U_{fastener\_tension} = \left\{ \frac{1}{2} \frac{AE}{(h_1 + h_2)} (w_1 - w_2)^2 + preload \cdot (w_1 - w_2) \right\} \Bigg|_{x=L_i+L_c} \tag{37}$$

$$\begin{aligned} U_{fastener\_shear} &= \left\{ \frac{1}{2} k_{fastener\_shear} \cdot \Delta_{fastener\_slide}{}^2 + friction \cdot \Delta_{fastener\_slide} \right\} \Bigg|_{x=L_i+L_c} \\ \Delta_{fastener\_slide} &= \left[\left(u_1 + \frac{h_1}{2} \frac{dw_1}{dx} \right) - \left(u_2 - \frac{h_2}{2} \frac{dw_2}{dx} \right) \right] - \delta_{hole\_clearance} \end{aligned} \tag{38}$$

The energy expressions for the work potentials from applied moments and axial forces are given in equations 39 and 40. These loads are applied at the freed end of the model at $x=L_i+L_c+L_f$, as shown in figure 47. If fixed deflection and slope conditions were applied to the freed end (e.g., to simulate a specimen in the grip of a test machine), stiff springs similar to those used in equations 31 and 32 could be used.

$$W_N = N \cdot u \Big|_{x=L_i+L_c+L_f} \tag{39}$$

$$W_M = M \frac{dw}{dx} \Bigg|_{x=L_i+L_c+L_f} \tag{40}$$

The total energy of the system is written as equation 23. The expression has unknowns that are the polynomial coefficients α in equation 22 and β in equation 21. Taking the partial derivatives of Π with respect to the unknowns (equation 20) yields a system of linear equations that can be solved by matrix operations.

$$\begin{aligned} \Pi = {} & U_{extension} + U_{bending} + U_{beam\text{-}column} \\ & + U_{extension\_tie} + U_{deflection\_tie} + U_{slope\_tie} + U_{contact} \\ & + U_{fastener\_tension} + U_{fastener\_shear} \\ & - W_N - W_M \end{aligned} \tag{41}$$

The result is a displacement solution of the structure given the iterative variables discussed in the equations in this section (contact state and fastener joint load). Crack-tip forces and moments can be derived from the displacement solution, which are used as inputs in the crack-tip element to calculate the strain energy release rates at the crack tip.

3.3 NUMERICAL IMPLEMENTATION

The solution method was implemented in MATLAB®. A flow diagram is shown in figure 51 to illustrate the implementation of the solution method.

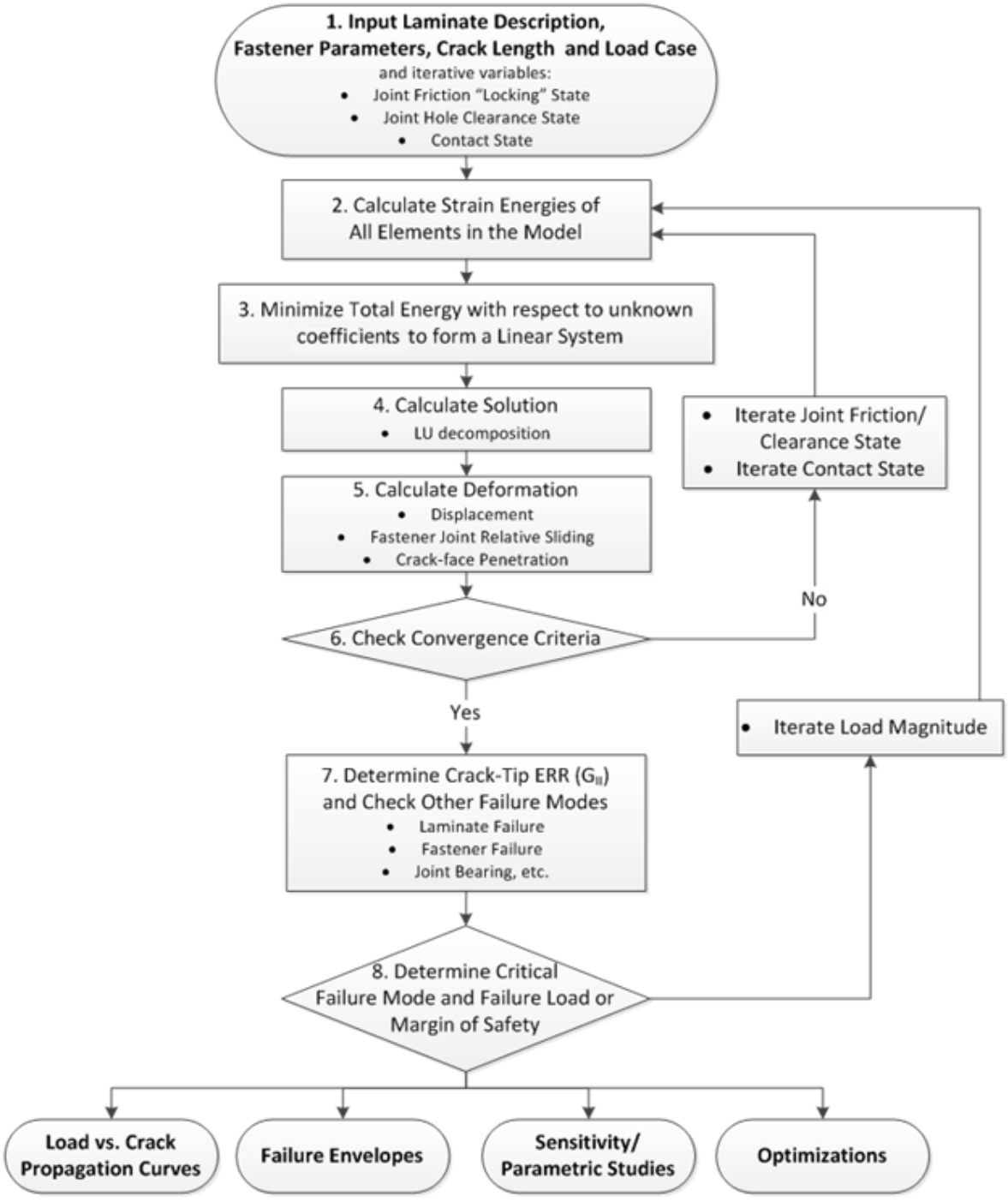

Figure 51. Flow diagram of the analytical solution [3]

The details of the steps are described as follows:

1. The analysis inputs were defined. Input properties included the composite laminar properties, the layup of each laminate/sublaminate, cure-to-room temperature change, fastener material, fastener size, fastener preload, fastener-hole clearance, crack-face coefficient of friction, the loads/boundary conditions, and dimensions such as crack length, total length, and width. Strength properties such as critical energy release rates, mixed-mode fracture law parameters, and laminate surface strain to failure were also defined for each failure mode considered. Derived properties, such as the effective laminate properties, fastener axial stiffness, fastener flexibility, and friction limit, were calculated. The iterative parameters were also initialized. For the beginning of each analysis, the fastener shear joint was set to be friction locked (i.e., infinite joint shear stiffness) and the joint has not slipped (i.e., hole clearance not subtracted from the joint sliding displacement). Also, all contact springs were turned off, except for those at the fastener location. These iterative parameters changed as the nonlinear analysis progressed.
2. The strain energies of each beam-column and spring element in the model, and the work associated with the applied loads/boundary conditions, were computed. The total energy was expressed as a function of shape functions of the beam-column elements.
3. The expression for the total energy was differentiated with respect to each unknown coefficient to be solved. This yielded a set of n linear equations with n unknowns. The set of equations was assembled into a matrix and a vector in the form of $Ax=b$, in which the vector x is the n unknowns, A is an $n \times n$ matrix, and b is an $n \times 1$ vector. The calculations in steps 2 and 3 were computationally onerous (integration and partial differentiation). All the terms in the A-matrix and the b-vector could be pre-calculated as explicit algebraic expressions ahead of time. This approach worked as long as the underlying structure of the analytical model (e.g., the number of beam-column elements, and the connections between the beam-column elements and springs) did not change the number of contact springs. The pre-calculation, however, still left a lot of customizable parameters in the model (e.g., model geometries, laminate properties, applied loads and displacements boundary conditions, fastener-joint properties, joint shear friction, fastener-hole clearance, and contact-spring states).
4. The linear system was solved using LU decomposition. The LU decomposition method was faster and numerically more stable than Gaussian elimination. This was particularly important because the matrix was very close to singular. The displacement solution represented one with minimum energy. However, this solution did not represent a converged solution with the correct fastener friction load, hole-clearance state, and contact-spring states. These parameters were iterated outside the linear system.
5. The displacements of the beam-column elements were calculated as the raw solution. From the displacement solution, various structural quantities were also calculated (e.g., slopes and strains in the beam-column elements, fastener joint relative displacements/forces, and local contact penetration). The deformed shape of the cracked beams determined the areas where contact springs needed to be activated. The iterative parameter and fastener joint load, was updated.
6. Iteration convergence criteria were checked. For the fastener joint, the initial state was friction locked and the joint had not slipped. If the solutions in step 5 indicated that the shear load transferred through the joint via friction was greater than the friction limit, the joint would be unlocked (joint shear spring changed from infinite stiffness to actual joint

shear stiffness) and the hole clearance would interact with the joint relative shear displacement. For the contact resolution, all the contact springs with local penetration were turned on, whereas those with positive contact clearance were turned off. These parameters were returned to step 2 to calculate a solution for the next iteration. In rare cases, convergence could not be achieved because of contact chattering.

7. Solution parameters pertinent to failure checks were computed. The column-beam displacements were related to the loads and moments at the crack tip. The mixed-mode strain energy release rates (G_I and G_{II}) were calculated using the Davidson crack-tip element. Laminate surface strains were also calculated from the displacement solutions. Fastener tension and bolt shear were also calculated.
8. The failure measures were compared against the allowables for their corresponding failure modes, and margins of safety were calculated. If the failure load and critical failure mode were sought, the applied load magnitude was iterated until the minimum margin of safety reached 1.0. All margins for all failure modes were recorded. This was important because competing failure modes could result in scenarios in which the observed failure mode in tests was different from the expected/designed failure mode.

The computational efficiency of the above approach relied on the ability to arrange the main part of the problem as a linear system that could be solved using linear algebra, while leaving the nonlinear part of the problem in an outer-iteration loop. The linear and nonlinear aspects of the problem were carefully separated out. For example, the on/off logic governing contact resolution was handled by an iteration loop. However, the connections and the stiffness of the contact springs were always present in the pre-calculated linear system. They were simply turned on or off using a 0/1 multiplier in the energy expressions.

3.3.1 Mixed-Mode Modeling Results

The analytical method developed is capable of analyzing any general configuration that is a split-beam with a single crack arrest fastener. The purpose of this section is to demonstrate the application of the analysis method and further investigate the behavior of the arrest fastener.

The failure modes considered in the following analysis are discussed in the context of engineering design. The first failure mode, crack propagation, is the failure mode suppressed by the fastener feature. The use of a fastener can effectively reduce crack propagation. However, propagation past the fastener can continue at higher loads. The failure load for crack-propagation failure mode is defined as the critical load for a permissible crack length. The selection of this crack length can be a function of the design requirements or the behavior of the structure itself. Although crack propagation is stable past the fastener, allowing continuous growth eventually leads to other failure modes, such as panel buckling due to reduction in stiffness, and increased susceptibility to environmental effects such as fluid ingression. The inability to demonstrate crack arrestment might also hinder the substantiation of the FAA's bonded joint requirements.

In addition to the crack-propagation failure criterion, the laminate in-plane failure due to high surface strain was also considered. Laminate failure was the only alternate failure mode observed in the testing, and it was the ultimate failure mode of the structure. In test results, the strain gauges installed at 50.8 mm (2.0 inches) from the fastener indicated that laminate failure (filled-hole tension) occurred when the surface strain reached 9000με. This was the case for both the quasi-isotropic and 50% 0° layup specimens. Using the analytical model, it was determined that the surface strain at the fastener location would have been approximately 10000με. Therefore, ε_{ult}=10000με was used as the surface strain at laminate failure (filled-hole tension) in the following analyses.

Fastener yielding was also considered as an alternate failure mode for analysis. However, the strength of titanium (σ_{yield} = 1034 MPa / 150 ksi) is too high to compete with the interlaminar and laminate modes of failure. Additional failure modes, such as joint-bearing failure and fastener pull-through, can be considered using the same analytical framework presented.

From an optimized structure perspective, a well-designed fastener arrest feature effectively arrests the delamination until laminate failure (i.e., the arrest feature allows the in-plane strength of the laminate to be fully utilized without the designer/stress analyst having to worry about delamination propagation). The following parametric and sensitivity studies show how different failure modes might interact, in addition to studying the general behavior of the arrest fastener.

The crack-propagation parametric studies replicated the long-panel configuration as tested. The split-beam had a total length of 317.5 mm (12.5 inches) between the boundaries (figure 52). The width was 31.75 mm (1.25 inches). The fastener was located at 228.6 mm (9.0 inches) from the boundary on the intact side. The tension load was applied to the lower sublaminate, zero deflection, and slope boundary conditions. This type of configuration simulated a termination structural detail, such as skin-stringer edge/termination. Two fastener parameters that were not included in the testing, diameter and hole clearance, were studied here.

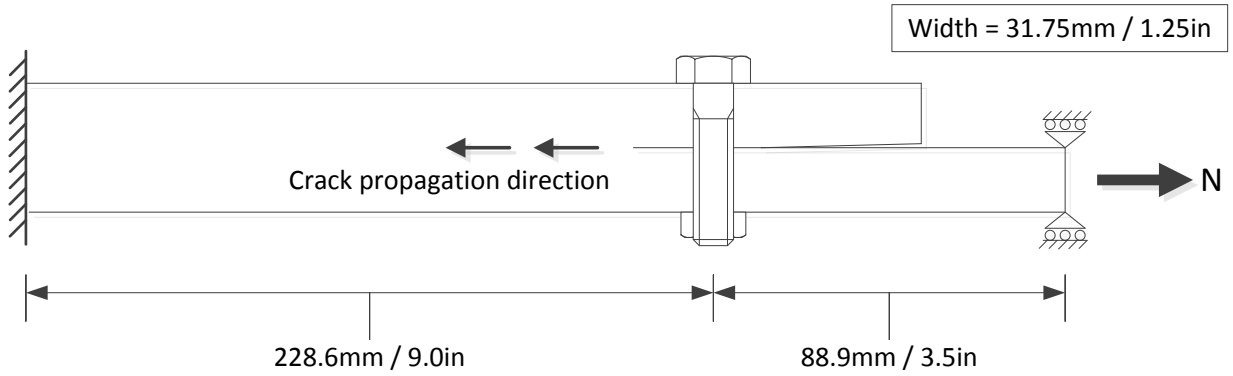

Figure 52. Schematic of analytical model used in parametric and probabilistic [3]

The lamina material used was the same as that used previously—BMS8-276 (Toray T800S/3900-2) unidirectional tape. Each sublaminate has a 24-ply quasi-isotropic layup. A constant laminate surface strain to failure at the fastener-hole location, 10000με, was assumed for the laminate failure mode. It was assumed for simplicity that the strain to failure was constant regardless of layup and fastener diameter. Crack-face friction is calculated using equation 42, which is shown to be a reasonable estimate in the correlation results. The input properties used in the follow studies are summarized in table 10.

$$friction = \sigma_{yield} \cdot A_{fastener} \cdot (\mu = 0.25) \cdot 50\% \tag{42}$$

Table 10. Properties used in parametric studies [3]

	SI Units	English Units
E_1	142.0 GPa	20.6 Msi
E_2	7.8 GPa	1.13 Msi
v_{12}	0.34	
G_{12}	4.0 GPa	0.58 Msi
G_{IC}	280 J/m^2	1.6 in-lb/in^2
G_{IIC}	1751 J/m^2	10 in-lb/in^2
Fastener Diameter	6.35 mm	0.25 inches
Fastener Elastic Modulus	113.8 GPa	16.5 Msi
Fastener $\sigma_{yield,tension}$	1034 MPa	150 ksi
E_x (quasi-isotropic)	59.2 GPa	8.59 Msi
Joint Shear Stiffness, d = 3.06 mm (0.125 inches)	8021 N/mm	45803 lb/in
Joint Shear Stiffness, d = 4.59 mm (0.1875 inches)	10511 N/mm	60019 lb/in
Joint Shear Stiffness, d = 6.35 mm (0.25 inches)	12733 N/mm	72708 lb/in
Joint Shear Stiffness, d = 7.66 mm (0.3125 inches)	84370 N/mm	84370 lb/in
Coefficient of Friction	0.25	
Fastener Preload (clamp-up)	0.5 × Area$_{fastener}$ × Fastener $\sigma_{yield,tension}$	
Friction Force, d = 3.06 mm (0.125 inches)	1.02 kN	230 lb
Friction Force, d = 4.59 mm (0.1875 inches)	2.30 kN	518 lb
Friction Force, d = 6.35 mm (0.25 inches)	4.09 kN	920 lb
Friction Force, d = 7.66 mm (0.3125 inches)	6.40 kN	1438 lb
Laminate Surface Strain to Failure at Fastener Hole	10000 με	

First, the effect of fastener diameter is presented. Figure 53 shows the analysis results using a constant width for the model, which also implies reduction in fastener pitch (Width/diameter, W/d) as the fastener diameter increases. When the frictionless assumption was used in the analysis, the initial step increase in propagation load due to mode I suppression was almost identical for all

fastener diameters, from 31 kN to 48 kN (7 to 11 kips). The high stiffness of the fastener made it effective at suppressing mode I propagation regardless of diameter. As the crack length increased, the models with larger fasteners experienced greater increase in propagation loads, benefiting from the higher joint shear stiffness. However, the benefit of using a larger fastener over a small one was relatively small because the joint shear stiffness increased slowly with fastener diameter. Finally, laminate surface strain failure occurred at approximately 70 kN (16 kips) (depicted as circle markers). The smaller fastener models saw marginally higher final failure loads because the lower joint shear load resulted in lower moment at the fastener, which led to lower laminate surface strains.

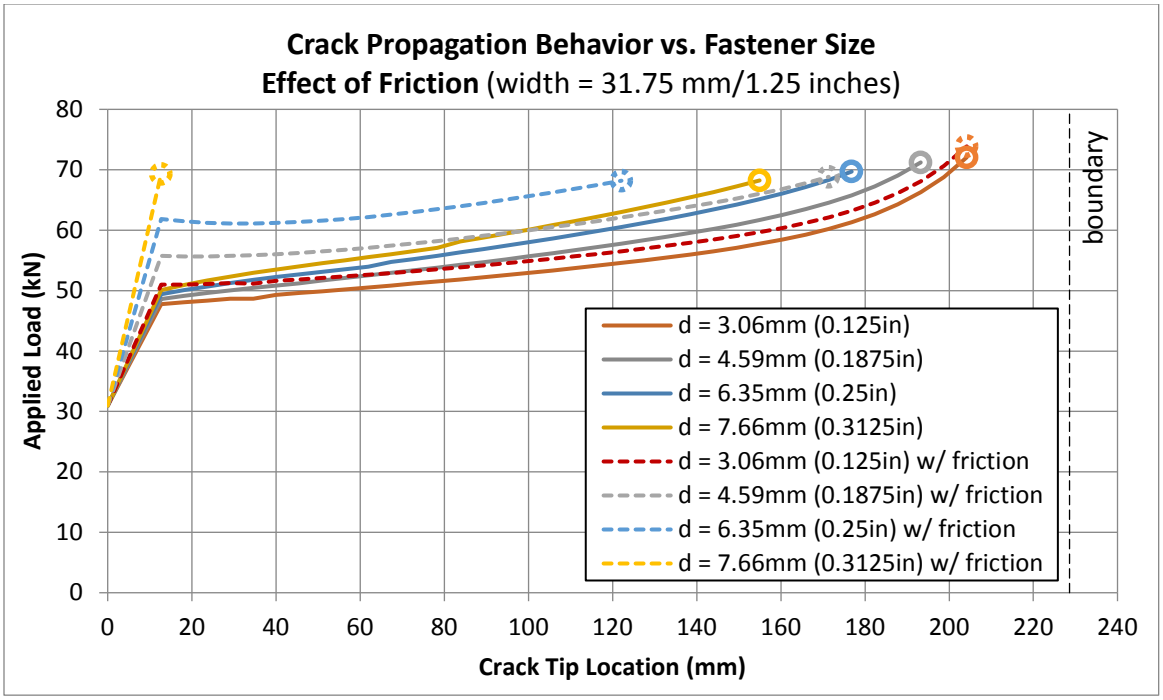

Figure 53. Crack propagation curves for varying fastener sizes – constant width [3]

When the friction force due to fastener preload was modeled, the initial step increase in propagation load was far greater with increasing fastener diameter. This increase in propagation load, in addition to the effect of mode I suppression, could be directly attributed to the higher friction generated using larger fasteners with higher preload. For the 7.66-mm (0.3125-inch) fastener, the propagation load exceeded the laminate failure load at 69 kN (16 kips), causing final failure before further propagation was possible.

However, it is impractical to use larger fasteners and lower the fastener pitch to take advantage of the higher friction in a real structure. The laminate surface strain to failure at the hole location decreases with fastener pitch and will lead to a heavy design limited by the in-plane failure mode. Figure 54 shows the analysis results using a constant fastener pitch in which the width of the model is always equal to five times the fastener diameter (5D). The propagation load is normalized by width to allow comparison between different fastener sizes. The overall trends are similar to the constant width analysis. A couple of different details are observed in figure 54. With the frictionless assumption, the model with a larger fastener has lower propagation load per unit width

than that of the smaller fastener. This is because the fastener joint shear stiffness increases less than linearly with fastener diameter, whereas the model width scales linearly with fastener diameter. Hence, the effective joint shear stiffness per unit width actually decreases slowly with increasing fastener size. When friction was modeled, the larger fastener diameter still benefited from the higher initial step increase in propagation per unit width, but the advantage over a smaller fastener was diminished. This was because the fastener preload was proportional to the diameter square but was shared by the model width, which is linearly proportional to the diameter. Therefore, some advantage could be exploited by using larger fasteners only if friction was considered. Similar to the constant width analysis, for the 7.66-mm (0.3125-inch) fastener, the propagation load exceeded the laminate failure load at 2k N/mm (11 kips/inch), causing final failure before further propagation was possible. Last, the propagation load per unit width appeared to converge after crack length of 100 mm (3.9 inches) for different fastener diameters when friction was modeled. The above observations suggest that the crack-propagation behavior with a delamination arrest fastener is very consistent if the fastener pitch is to remain constant.

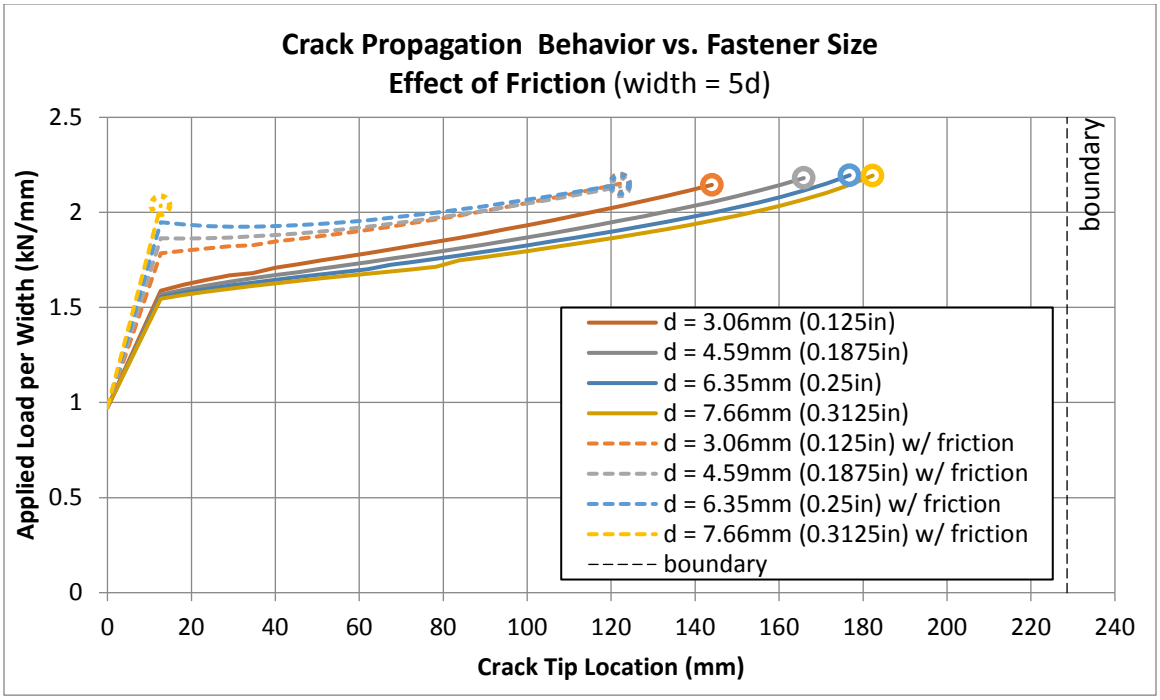

Figure 54. Crack propagation curves for varying fastener sizes - constant fastener pitch [3]

One parameter not studied in the tests was the effect of fastener clearance. All the test specimens were made to have zero hole clearance. Here, the effect of fastener hole clearance on delamination behavior was studied using the analytical model. The hole clearance analyzed ranges up to 0.152 mm (0.006 inches), which covered typical clearance fit manufacturing tolerances for composite structures. The hole clearance has the effect of shifting the load versus crack-tip location curves horizontal to the right. This was an expected outcome because the fastener joint must slide before load could begin to transfer via shaft-hole contact. A small slip in the joint resulted in a

large propagation distance. Figure 55 shows that for every 0.051-mm (0.002-inch) increase in hole clearance, the crack length becomes 10 mm to 20 mm (0.4 inches to 0.8 inches) at the same load.

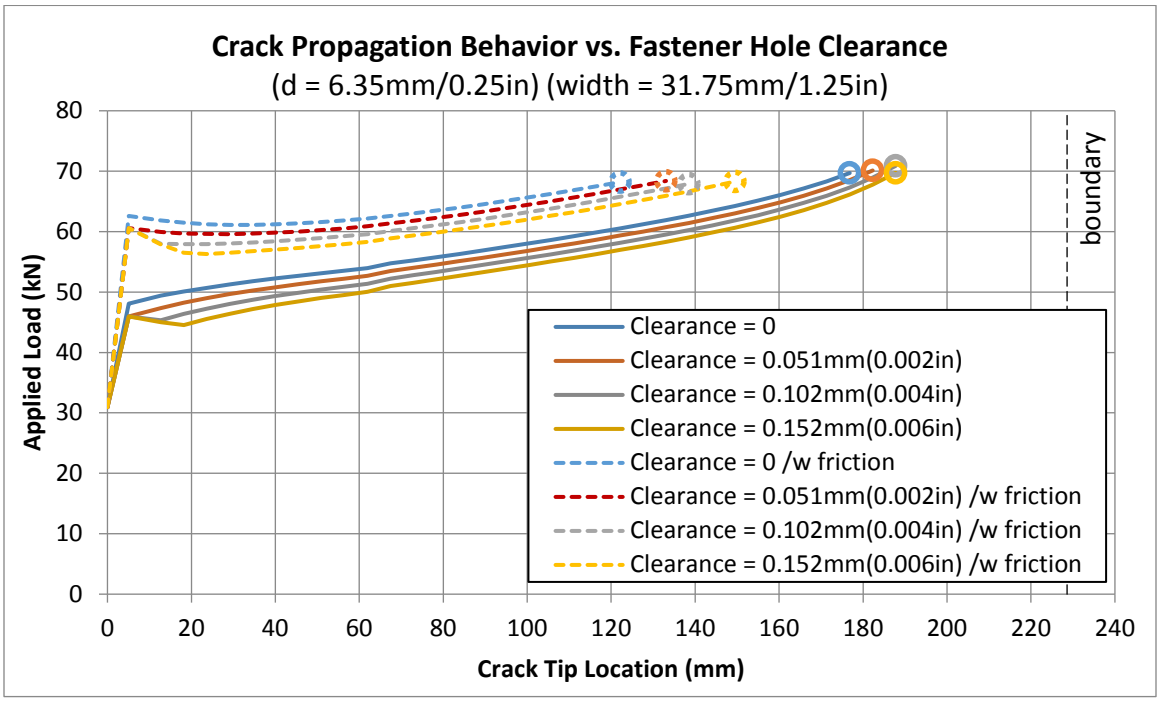

Figure 55. Crack propagation curves for varying fastener hole clearance [3]

Another observation associated with fastener hole clearance was the increased tendency for the crack tip to propagate unstably when exiting the fastener area. When the crack tip was at the center of the fastener, the joint was inactive and all models with varying hole clearance must behave identically. As soon as the crack tip exited the fastener, the joint had to slip until the clearance was consumed and the joint engaged. During this slide, the delamination was allowed to propagate unstably. The length of unstable propagation was drastically higher when friction was modeled. This was because the unstable propagation due to hole clearance was added to the unstable propagation that would normally occur when the crack tip exited the fastener area with preload.

This was an important issue if the design had to demonstrate arrestment/retardation at a permissible crack length because a small manufacturing deviation could result in large scatter in the test outcome. This detrimental effect could be worse in fatigue tests, in which a small hole clearance could cause very fast initial delamination growth over very few cycles, providing confusing evidence suggesting that the fastener was completely ineffective at retarding delamination growth. Fortunately, expansion sleeve fasteners were often used in composite primary structures, effectively eliminating hole clearance altogether.

One of the advantages of developing an analytical method is that it enables rapid iteration through the design space, the results of which can be used to identify configurations and design parameters that yield more capable structures. Sensitivity analysis is the study of how variations in the outcomes of a system can be statistically attributed to the variations in the inputs. This type of analysis is extremely valuable for determining the underlying forces that drive the behavior of the

system. This is especially useful for problems for which there are many inputs, and the relationship between inputs and outputs is not obvious.

In this study, the same model configuration was used. Instead of a propagation analysis, failure load was interrogated only at a crack-tip location of 12.7 mm (0.5 inches) (figure 56). That is, at this crack-tip location, the minimum of the crack-propagation load and laminate-failure load was recorded as the failure load of the analysis. This was to simulate the design criterion that crack propagation beyond the fastener be avoided. For comparison, the initial unstable crack-propagation load was also analyzed (figure 56).

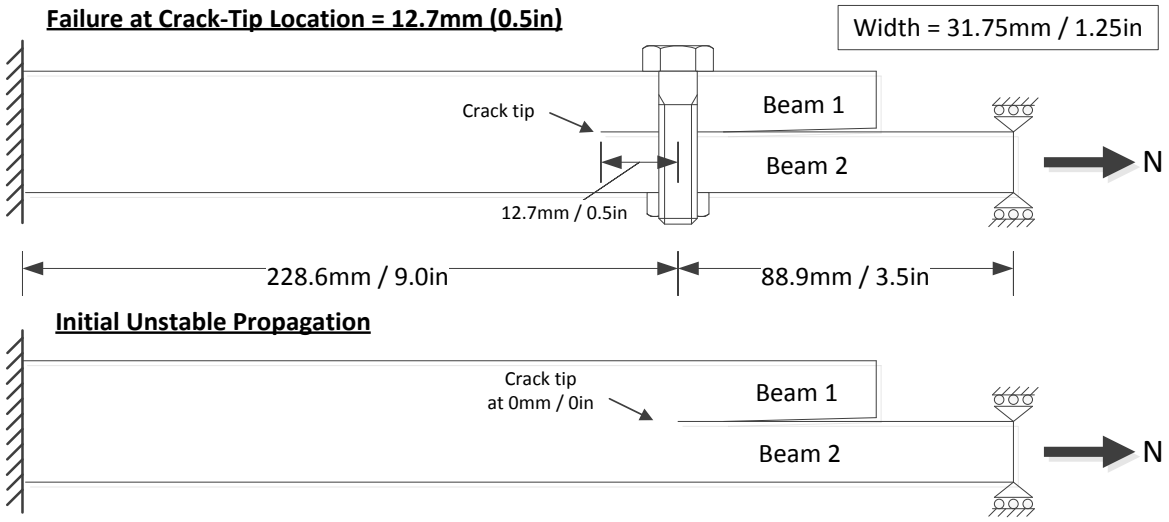

Figure 56. Configuration used in design space study [3]:

A random-number generator was used to occupy random points in the design space specified in table 11. The table includes typical design parameters within the control of engineers. Equivalent axial stiffness (E_x), instead of actual layups, was used to fill the design space as a continuous variable. The stiffness range used represents layups from the softer quasi-isotropic to the stiffer 50% 0° layups. The thickness ranges chosen cover layups from 16 plies to 64 plies. The diameter of the arrest fastener has a wide range from 3.175 mm (0.125 inches) to 12.7 mm (0.5 inches). All variables take on a continuous uniform distribution. (This brute force approach to covering the design space will include some unrealistic configurations, such as a 12.7-mm [0.5-inch] fastener being used with a 6.1-mm [0.24-inch] laminate.)

Table 11. Input parameters for design space study—uniform distribution [3]

	Lower Bound	Upper Bound
E_{x1}	59.3 GPa (8.6 msi)	86.9 GPa (12.6 msi)
E_{x2}	59.3 GPa (8.6 msi)	86.9 GPa (12.6 msi)
h_1	3.05 mm (0.12 inches)	12.2 mm (0.48 inches)
h_2	3.05 mm (0.12 inches)	12.2 mm (0.48 inches)
Fastener Diameter	3.175 mm (0.125 inches)	12.7 mm (0.5 inches)

The constant input parameters listed in table 12 include parameters typically not within the control of engineers, unless there is a complete change of material systems. The values for these parameters are the same as those used in the previous analyses.

Table 12. Input parameters for design space study—constants [3]

	SI Units	English Units
Fastener Elastic Modulus	113.8 GPa	16.5 msi
Fastener $\sigma_{yield,tension}$	1034 MPa	150 ksi
G_{IC}	280 J/m^2	1.6 in-lb/in^2
G_{IIC}	1751 J/m^2	10 in-lb/in^2
Coefficient of Friction	0.25	
Fastener Preload (clamp-up)	0.5 × Area$_{fastener}$ × Fastener $\sigma_{yield,tension}$	
Laminate-Surface Strain to Failure at Fastener Hole	10,000 με	

Monte-Carlo simulation was used to analyze random points in the design space. For each group, 30,000 points were analyzed, for a total of 60,000 runs. Using a single central processing unit on a desktop computer, the analyses took less than 2 hours to complete. The results are post-processed using simple statistical methods.

The analysis covers many unique configurations randomly scattered in the design space; therefore, the specific values of the failure load averages in table 13 carry little meaning in terms of understanding the structural capability of a particular design. However, they are useful in providing a general comparison between the “With Fastener” and the “Without Fastener” group analyses shown in figure 56. The first observation is that the “With Fastener” group has an average failure load more than 90% higher than the “Without Fastener” group. The “Without Fastener” group experiences only one failure mode—delamination propagation—which leads to the catastrophic splitting of the laminate. This means that the higher structural capability offered by the laminate in-plane strength is never used. In the “With Fastener” group, the delamination-propagation failure mode and the laminate surface strain failure mode begin to compete with each other, and at much higher loads. The in-plane strength capability of the laminate is better utilized, and the structure is

generally more capable and efficient. (The fastener yield failure mode did not occur in the Monte-Carlo simulation.)

Table 13. Summary of design space study—failure loads [3]

	Propagation Failure	Laminate Surface Strain Failure	Combined
With Fastener			
Average Failure Load	86.2kN (19.4 kips)	78.1kN (17.6 kips)	85.0kN (19.0 kips)
% Occurrence	85.8%	14.2%	100%
Without Fastener			
Average Failure Load	43.8kN (9.8 kips)	N/A	43.8kN (9.8 kips)
% Occurrence	100%	0%	100%

The correlation coefficient between each input parameter and the failure load is computed to determine the effect of each parameter on the outcome. The correlation coefficient can be calculated using equation 43, in which μ and σ are the mean and the standard deviation of a parameter, respectively. The value ρ ranges between -1 and +1. A positive ρ means the two parameters have positive correlation (i.e., the increase in one parameter is met by the increase of the other). If $\rho = +1$, the correlation is perfect, and any increase in one parameter is matched exactly by the same proportional increase in another. The argument for negative ρ is the same. If $\rho = 0$, then there is no correlation, and any change in one parameter has no statistical influence on the other parameter. In the current analysis, the configuration and structural properties are inputs, and the failure loads are outputs, so it is reasonable to add cause and effect to the context of correlation. The change in an input parameter leads to a systematic change in the output, quantified by the correlation coefficient.

$$\rho(X,Y) = Correlation(X,Y) = \frac{Covariance(X,Y)}{\sigma_X \sigma_Y} = \frac{E\left[(X-\mu_X)(Y-\mu_Y)\right]}{\sigma_X \sigma_Y} \tag{43}$$

Figure 57 shows the side-by-side comparison of the coefficients of correlation to input parameters (i.e., the sensitivity of failure load to the corresponding design parameters between the two groups analyzed). The last three parameters (E_{x1}/E_{x2}, h_1/h_2, and EA_1/EA_2) are derived from the first four parameters (E_{x1}, E_{x2}, h_1, and h_2). The correlation coefficients between the two groups are surprisingly similar despite the differences in failure loads. The only exception is that the "Without Fastener" group has a more noticeable negative correlation to h_1. However, the structural behaviors of the two groups were markedly different despite the similar coefficients.

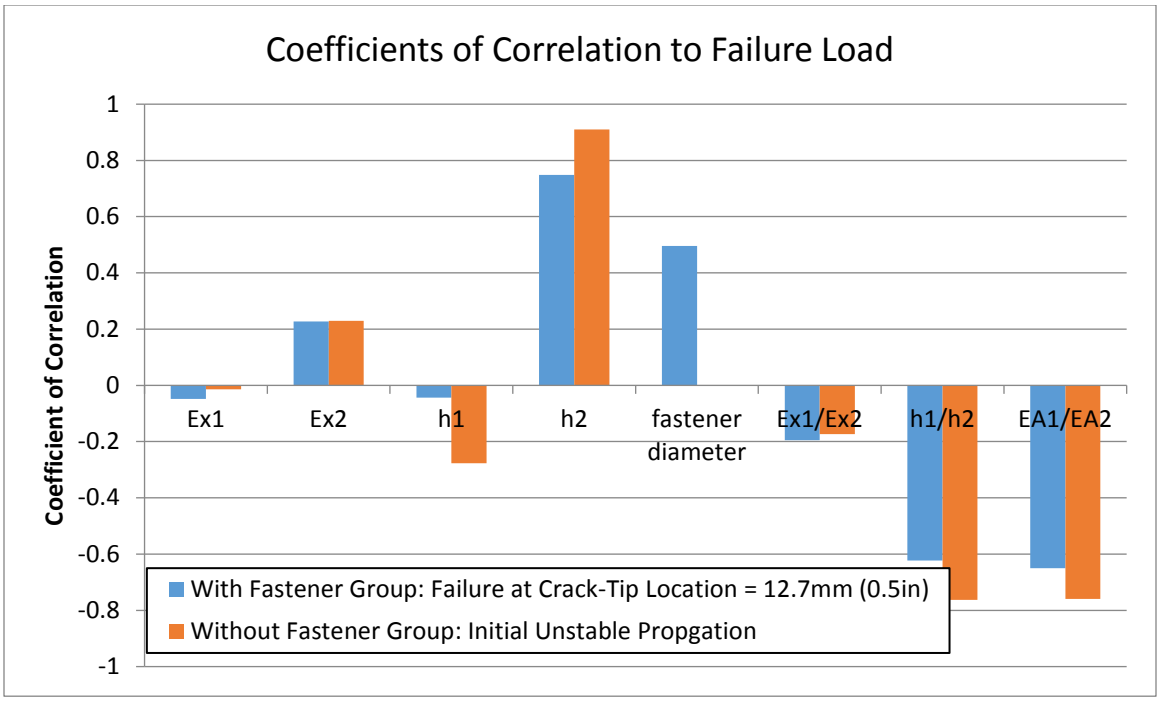

Figure 57. Coefficients of correlation—design space study [3]

In the "Without Fastener" group, failure is dominated by the mixed mode I and II delamination. The primary approach to increasing the delamination load is to configure the structure in such a way that minimizes crack tip mode I fracture component. This can be accomplished by bulking up the lower beam and thinning out the upper beam (figure 56). This design strategy is often used in areas such as the edge of a stringer flange, stringer runout, and stringer termination.

In the "With Fastener" group, the majority of the failure is in delamination, and a minority of the failure is in laminate surface strain failure. In the delamination-failure mode, the failure load responds to a reduction in the crack-tip mode II fracture component because mode I has been mechanically suppressed by the fastener. This explains the slight reduction in sensitivity to h_1. Also, increasing the fastener diameter helps to increase the propagation load by providing friction. The failure load of the laminate increases with the thickness and stiffness of the lower beam, which reinforces the correlation to E_{x2} and h_2.

The coefficients of correlation can be used to construct rules of thumb when designing features similar to those shown in figure 56. Conventional wisdom dictates that when designing a hardpoint-type termination, the laminate that is not loaded should be as soft and thin as possible. This minimizes the load transfer from the loaded laminate to the free laminate, and the shift in centroid (center of stiffness) before and after the crack tip. This in turn minimizes the opening moment at the crack tip (under tension) and minimizes the mode I energy release rate. This is fully consistent with the results shown in figure 57. However, in a real structure, designing to such rules will require well-managed ply dropoff over long distances and competing requirements from manufacturing and systems integration. If the arrest fastener is a part of the initial design, the constraint on thinning out the upper laminate can be eased. In addition, the effective footprint of

the fastener can be increased with radius filler or fitting features, increasing the area where mode I is suppressed.

3.3.2 Conclusions

Three key parameters contributing to the arrest capability of the fastener were identified through the modeling and testing: elimination of mode I, load transfer through friction, and load transfer through shear engagement of the fastener. The vertical separation of the analytical lines of crack growth versus load are due to varying levels of frictional load transfer assumed to occur. Meanwhile, the positive slope visible in figure 38 is caused by the shear engagement of the fastener providing load transfer from the loaded portion into the unloaded section. Finally, the spike visible in the figures is due to the elimination of mode I. The resulting combination accounts for the improved delamination resistance of bonded-bolted joints.

4. TWO FASTENER EXPERIMENTS

After the success of the single-fastener experimental work, the question of how useful a second fastener would be was left unanswered. Whereas mode I was eliminated, it was expected that additional fasteners would be effective in providing additional load transfer through friction and shear engagement, further increasing the arrest effectiveness of the system. As a result, two fastener test specimens were generated.

4.1 SPECIMEN CONFIGURATION

The initial specimen layup was chosen to be quasi-isotropic $(0/45/90/-45)_{3S}$. From previous experiments, it was found that propagation load was related to the layup stiffness, and a quasi-isotropic sample would provide a good baseline crack arrest effectiveness measurement. To aid in the comparison between multiple- and single-fastener tests, the ply count mirrored the single fastener specifications and the width was the same value—1.25 inches or 5 times the fastener diameter (5D) for a 0.25-inch fastener. The single-fastener testing showed this thickness and width were appropriate and representative of a standard thickness and fastener spacing. Finally, the fastener spacing was chosen to be 2 inches as finite element models suggested that this was a sufficient distance to avoid interplay between the fasteners. The layout is summarized in figure 58.

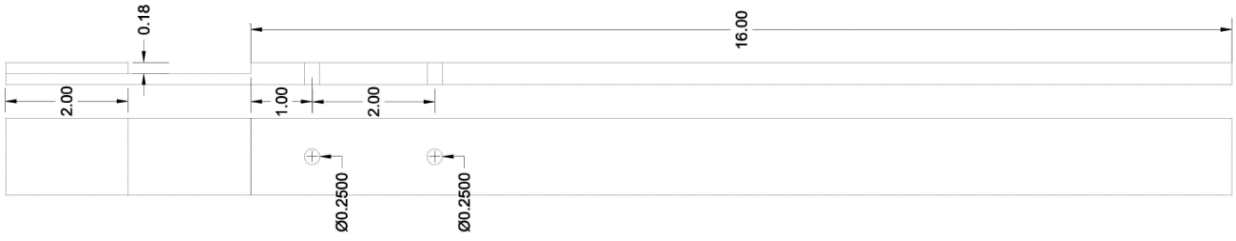

Figure 58. Two-fastener experimental specimen [19]

The samples were created using T800S/3900-2 prepreg tape and cured using a hot press at The University of Washington. The fasteners were installed initially at 40 in-lb, with subsequent tests varying this value between 0 and 40 in-lb. Additionally, careful drilling of the holes resulted in

transition fit fastener holes, referred to as zero-clearance holes, and clearance drilled holes with a defined level of clearance between the fastener shank and the hole wall. Because one of the key arrest mechanisms was shear engagement of the fastener, the clearance drilling was expected to reduce the fastener's capability.

4.2 EXPERIMENTAL RESULTS

Initial testing showed that the addition of a second fastener proved to be highly effective in arresting the crack. Significant growth past the second fastener did not occur for the initial round of testing (see figure 59). The data compared well with the single-fastener experimental work, with a noticeable spike in load near the second fastener. The obvious assumption was that the second fastener was providing load transfer, increasing the delamination resistance of the system further.

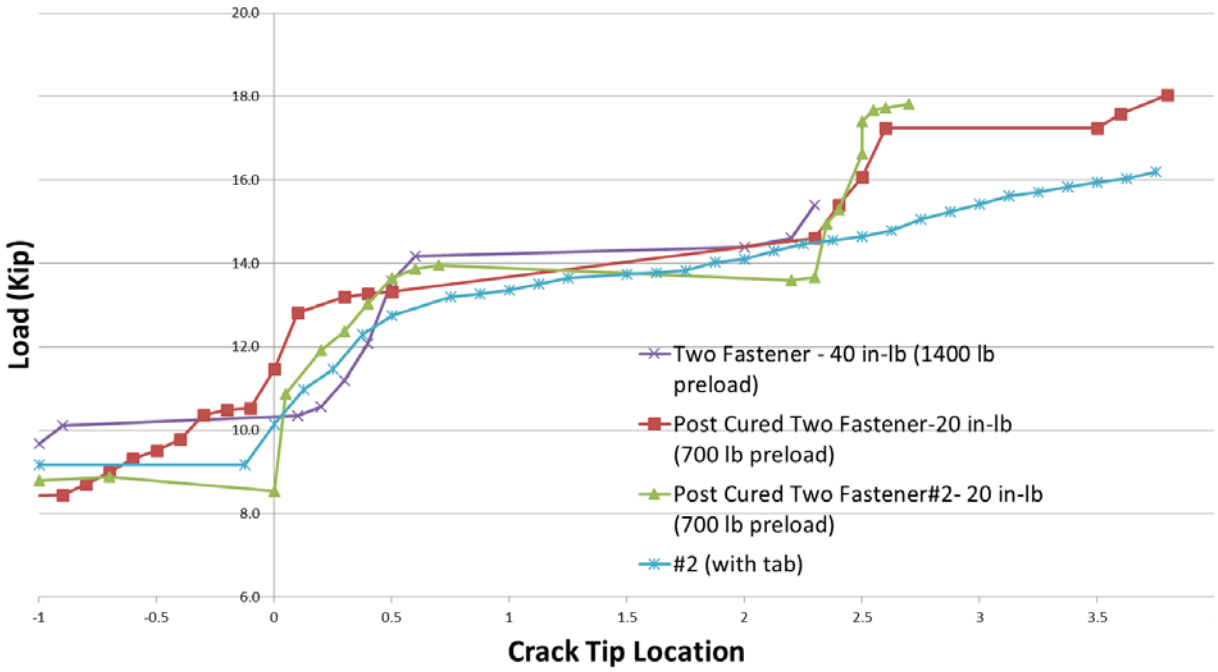

Figure 59. First round of two-fastener testing compared to single-fastener results [19]

Further testing commenced using clearance drilled fastener holes in addition to the transition fit, or zero clearance holes, utilized in the initial testing to generate greater crack growth. This succeeded, as greater crack growth was experienced by clearance drilled fasteners (see figure 60). The loss in arrest capability could be directly attributed to the delay in shear engagement of the fastener. As expected, the greater the value of clearance, the greater the drop in arrest effectiveness, until there was zero load transfer through shear prior to failure. Additionally, it was important to accurately measure the value of G_{IIC}. In figure 60, the highest curve is using the nominal G_{IIC} of 14 lb/in, and tends to overpredict the performance, whereas using a tested value of $G_{IIC} = 12$ lb/in provides much better agreement, with the dashed model line overlaying a set of experimental data very well.

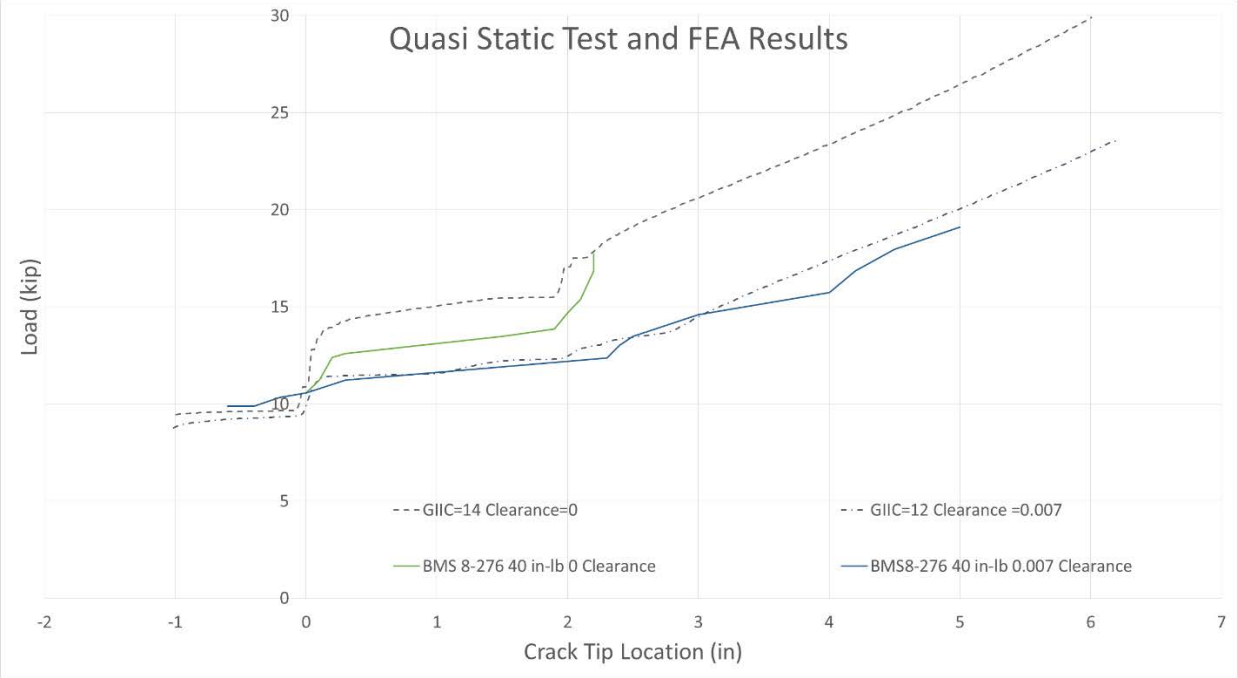

Figure 60. Representative test and analysis comparison of two-fastener results [20]

C-scans of the two-fastener samples (figure 61) were taken to compare to scans of the previous test articles, and good agreement was found. When the crack was near the fastener, the crack face showed extensive curvature, but as it departed the fastener region, it flattened out similar to previous test results.

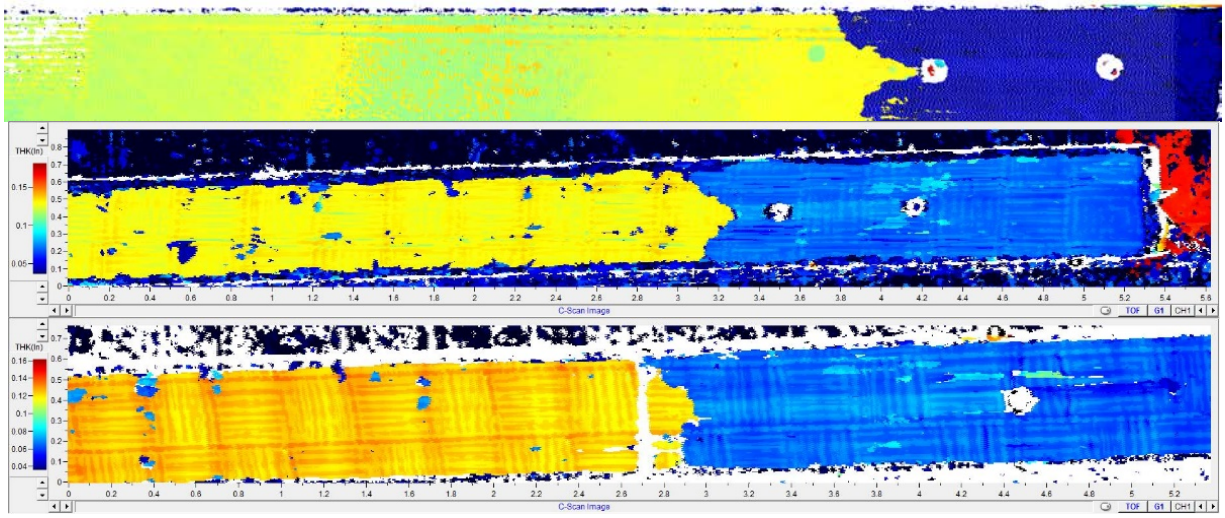

Figure 61. C-scans of samples (yellow is still bonded) [20]

5. TWO-FASTENER MODELING [20]

For the modeling of the two-fastener system, effort was focused on finite-element-based solutions because of the increasing complexity of analytical solutions proving to be unwieldy. The initial

two-dimensional model was based heavily on those developed by Cheung et al. [1–3], with subsequent reductions in complexity to improve model run times. Meanwhile, three-dimensional shell models were developed by Rodriguez [21] to try to capture the nonlinear crack front. Finally, one-dimensional models were developed by Richard [20] for future work in fatigue simulations and for rapid parametric studies.

5.1 TWO-DIMENSIONAL MODELING

Leveraging the success of prior model designs, a two-dimensional model was built in the finite-element software ABAQUS, which depicted a delaminating skin/stringer system similar to before. The same modeling processes and material properties used by Cheung were reapplied, with modifications necessary to include a second fastener.

5.1.1 FEA Model Design

Leveraging the success of prior model designs by Cheung et al. [1–3], a two-dimensional model was built in the finite element software ABAQUS, which depicted a delaminating skin/stringer system with parameters (summarized in table 14).

Table 14. Lamina and model properties [19]

Composite Lamina Material Properties (AS4/3501-6)		Model Properties	
Ply Thickness	.0075 inches	Layup	$(0/45/90/-45)_{3S}$
E1	$18.5*10^{6}$ psi	Element	CPE4R (2D) C3D8R
(3D)			
E2=E3	$1.64*10^{6}$ psi	Plate Thickness	0.18 in/plate
G12=G13	$0.871*10^{6}$ psi	Layup	(0/45/90/-45)3S
G23	$0.522*10^{6}$ psi	Width	1.25 inches
$\nu_{12} = \nu_{13}$	0.3	Length	12 inches
ν_{23}	0.4	Fastener Spacing	2 inches
GIC	1.5 in-lb./in^2	Fastener Stiffness	$1.6*10^{5}$ lb./in (shear)
GIIC	14.0 in-lb./in^2		$2.24*10^{6}$ lb./in (tension)
η	1.75	Preload	0 or 1000 lb
a=b=c	1	Friction Coefficient	0, 0.25 or 0.5

The model was built of two identical carbon/epoxy split beams joined together with titanium fasteners in a series, as shown in figure 62. Both plates are 12-inches long and 0.18-inches thick, which represents a 24-ply layup, in this case quasi-isotropic $(0/45/90/-45)_{3s}$. The grips were not modeled. Instead, both beams were fixed at one end while a load was applied to one beam at the other. The crack tip was initially 1 inch from the first fastener. This fastener was located 9 inches from the model end, which is fixed. The second fastener was typically located 7 inches from the

model's fixed end to present a 2-inch fastener spacing. However, this spacing was also varied to investigate the delamination response.

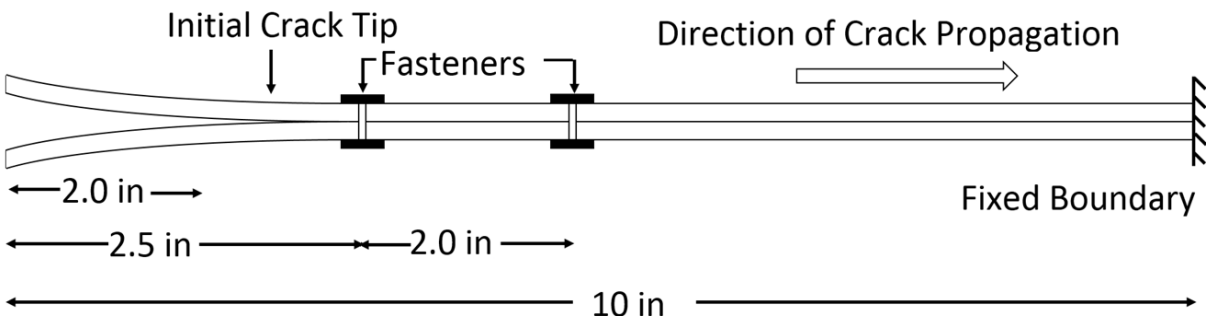

Figure 12. Two-fastener model [19]

To reduce the model complexity, each 0.25-inch diameter titanium fastener was represented by two springs, which enabled the decoupling of the tensile and joint stiffness. The extensional stiffness of the fastener was calculated as $2.24986*10^6$ lb./in., based on the fastener area and elastic modulus. Meanwhile, the joint stiffness was 160,883 lb./in, calculated using the fastener flexibility formula by Huth [10] with the 0.7 correction factor found by Cheung [3]. The springs were non-linear in their response to account for preload (tension spring) and clearance (shear spring). Preload was accomplished by establishing a non-zero load at zero extension. Similarly, as fastener clearance was assumed to simply delay the engagement of the fastener, the stiffness was set to zero for an extension range determined by the clearance and an assumption that the fastener was centered in the hole. For the rest of the spring's response it was assumed to behave in a linear manner.

The model was meshed with 4-node plane-strain quadrilateral elements (ABAQUS element CPE4R) of varying size. Initial modeling utilized one element per ply, resulting in an element size of 0.0075 inches high and 0.015 inches long. Subsequently, the elements were assigned anisotropic element properties based on the AS4/3501 material system, with properties modified to indicate the rotation of the plies. Modeling that combined plies had elements 0.0225 inches high and 0.045 inches long.

VCCT was used to calculate the crack-tip energy release rates [12]. The disbond/delamination was assumed to propagate in a self-similar fashion; therefore, the crack tip always remained at the prescribed interface between the two beams regardless of load conditions. The B-K law and the power law were used for the mixed-mode fracture with the parameter η shown in table 14. Finally, friction was modeled either as a constant value ranging from 0 to 0.5, or with stick-slip.

After the initial model was developed and refined to provide consistent convergence of the solution, further refinements were required to improve the accuracy of the predicted response because of the second fastener. Generally, the predicted crack-arrest capability of the second fastener obtained from the finite element model was significantly larger than what was expected. Because the mode I component had been eliminated, the load increase required to propagate the crack past the second fastener was expected to be equal to or less than the load step at the first fastener, but this was not the case. This inaccuracy was generated by singularities created by

methods of modeling the shear spring, which interestingly did not affect the results of single-fastener modeling. Prior to the refinement of the fastener modeling, the layup of the laminate was simplified to drastically reduce the simulation runtime without compromising accuracy.

5.1.2 Simplification of Model

When the model consisted of 48 plies, the same count as the experimental specimens, the simulations took approximately 1 day to complete when running on a desktop computer because of the complexity of the problem. Additionally, when a failure of the solution to converge occurred it was typically near the simulation conclusion as the crack tip reached the second fastener, resulting in a full day spent without useful data. A faster model was desired to reduce the time waiting for simulations to complete and allow a more efficient model to perform parametric analyses. Based on the modeling technique of having one element per ply, the driving factor of the model complexity was the limitation that the element thickness be equal to the ply thickness. The logical conclusion was to reduce the ply count, thereby increasing the element size for a model of the same dimensions. As simulations had indicated that there is minimal bending deformation of the specimen, as shown in figure 63, the stacking sequence of the laminate should not contribute significantly to the elastic response of the test. The resultant layup was simplified to two plates of eight plies each, the minimum number possible to still produce a symmetric quasi-isotropic layup. The results of the two simulations are shown in figure 63.

(a)

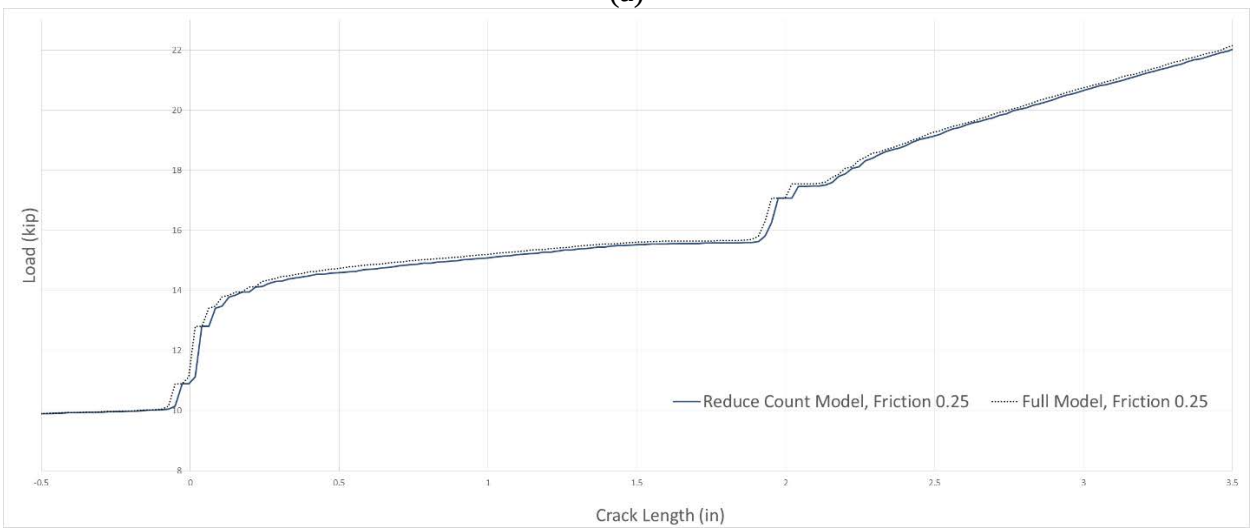

(b)

Figure 63. Bending response (a) and propagation comparison of (b) 48- and 16-ply models [19]

As shown in figure 63, the 48- and 16-ply models have good agreement. The small deviation between the two laminate configurations can be explained by the slightly different bending stiffness values of the laminates. Because the 8-ply plates have the 0^o lamina clustered on the

outside, the bending stiffness of the simplified model is larger, which results in slightly different propagation characteristics. The model runtime was reduced to approximately 1 hour because the number of degrees of freedom was reduced by an order of magnitude. Further research of quasi-isotropic laminates was conducted using the simplified model because it enhanced the rapidity with which results could be delivered. Finally, simulations were evaluated for large bending deformations, which could cause inaccuracies in the results.

5.1.3 Modification of Fastener Spring Location

Previous research in the propagation characteristics of delaminations in specimens with multiple arrest fasteners by W. Liu [22] indicated that the second fastener spring system was significantly more sensitive to the modeling methodology. In particular, while successful in single-fastener designs, the inclusion of a fastener wall designed to distribute the load generated by the shear fastener created an artificial spike in propagation load. This was caused by the fastener wall rod increasing the shear stiffness of the laminate at the point of the fastener, a phenomenon that does not actually occur. The removal of this wall subsequently reduced the load spike at the second fastener to a reasonable level. However, when running various models with zero friction, a jump in load remained present at the second fastener, as shown in figure 64, when examining the un-revised model's curve.

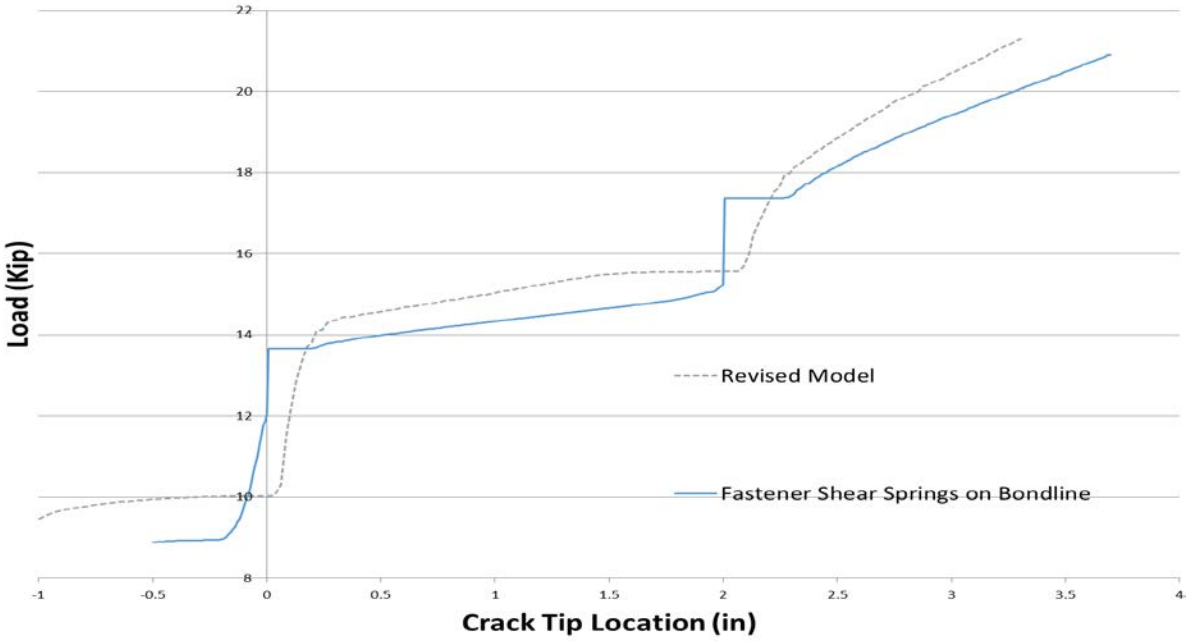

Figure 64. Comparison of model revision [19]

Considering that the only propagation mode occurring at the second fastener was mode II, when friction was not included, the only way the fastener should be resisting the delamination is through shear stiffness. However, this resistance should only occur after the crack has passed the fastener and the spring begins to extend, not prior to the crack reaching the fastener. Further investigation indicated that the application of the shear spring on the bond line of the specimen created a singularity at the node of interest. To account for this, the shear spring was moved one element off

the bond line, which resulted in more realistic predictions as seen in figure 65. Demonstrated with the inclusion of friction, the fastener was able to become effective prior to the crack tip reaching it. The distribution of the preload through the laminate allowed for the transfer of load through friction before the crack tip reached the fastener.

5.1.4 Modeling Results

Figure 66 shows that there was a consistent stabilization of the crack and superior arrest compared to a single fastener. Based on previous research by Cheung et al[2], it was expected that the crack would curve around the fastener, but C-scans showed some disagreement between crack-tip location for the model and as measured. Meanwhile, the material supplier listed the value of G_{IIC} as 14 lb/in, whereas the actual measured value in 3ENF specimens was 12 lb/in. As shown in figure 65, using the adjusted value results in an accurate model prediction, while using the supplier's value results in an approximately 20% overprediction in load required to propagate the crack, indicating the importance of this parameter.

Additionally, the effects of clearance are captured accurately here. Assuming a zero-stiffness fastener over the clearance range appears to represent the solution reasonably well. The effects of friction are also included in this model, with the frictional values found via testing.

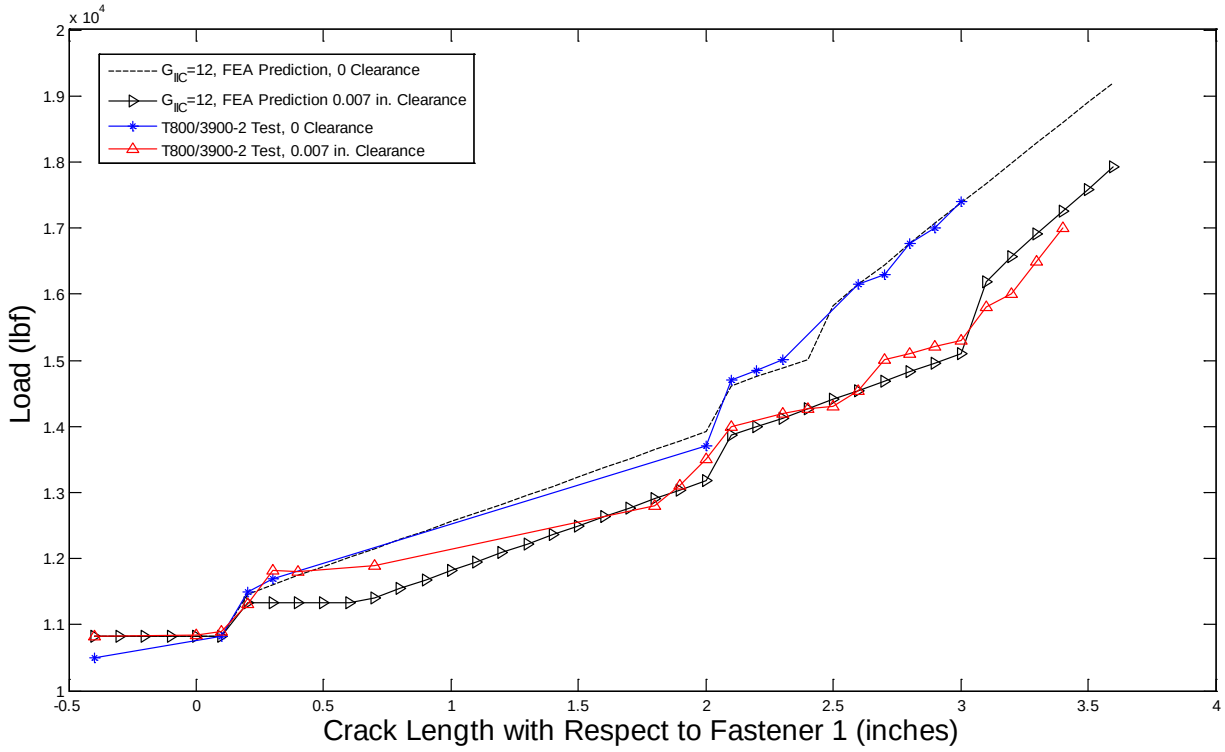

Figure 65. Comparison of test results and analysis

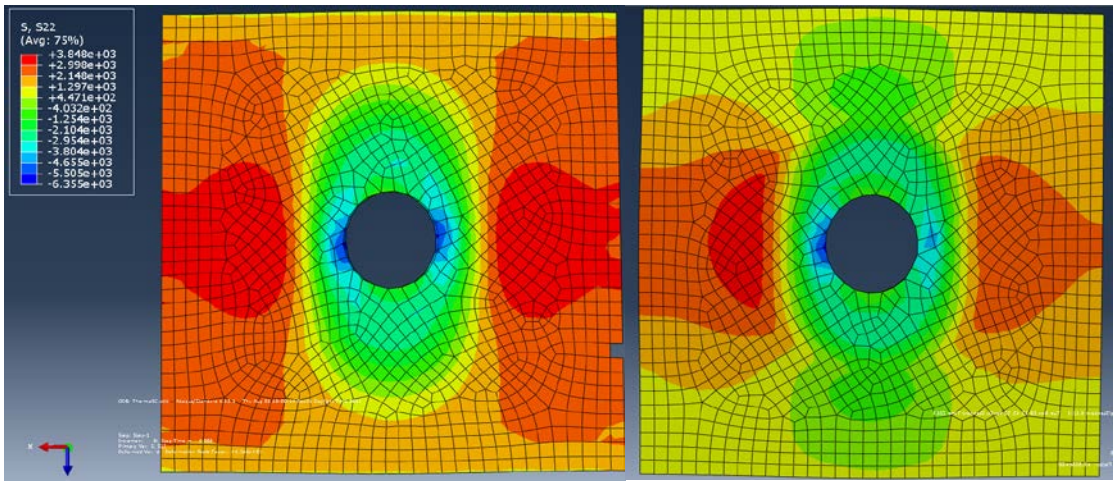

(a) (b)

Figure 66. Model preload, 0-degree interface (a) and 45-degree interface (b) [19]

Further testing was conducted on another typical laminate configuration, 50% 0 plies, which verified the general applicability of the modeling methodology. It was found that stiffer laminates benefited less from the installation of fasteners because the crack propagated at a lower overall strain. However, the fastener was still beneficial, particularly in forcing the crack to propagate in mode II, and did provide some load alleviation. Interestingly, for asymmetric laminates, in which one plate was 50% 0 plies and the other was quasi-isotropic, the crack propagation was sensitive to where the load was applied. Greater crack propagation was observed when the softer laminate was the loaded laminate. This discrepancy in stiffness created a greater strain energy release rate for an equivalent loading, lowering the crack-arrest effectiveness by reducing the differential displacement of the two parts, which leads to fastener load transfer. This result can be extended to off-centerline cracks. Depending on the location through the thickness of the laminate, the crack arrest effectiveness can be changed. Typically, when there is a larger unloaded section, relative to the loaded section, the crack arrest effectiveness is reduced.

5.2 ONE-DIMENSIONAL MODELING

Beam/bar and spring models were developed in ABAQUS and MATLAB® scripts. The benefit of one-dimensional modeling was the high speed at which results were generated. The MATLAB®-based model was designed to allow for use in parametric studies and eventually to allow for N fasteners to be simulated.

5.2.1 FEA Model Design

The material properties of the laminate needed to be calculated to create a one-dimensional model. For the simulations, classical lamination theory was employed to determine the axial and bending stiffness of the laminate. One potentially important detail was to use the laminate bending stiffness as calculated. For certain layups, the bending stiffness of the beam could vary significantly from the value predicted using isotropic theory and the axial stiffness. As with the two-dimensional models, Huth's fastener flexibility was used to model the shear stiffness of the fastener, whereas a constant diameter bar was employed to simulate the axial stiffness.

The model was subdivided in the same manner as that of the pure mode II model, with additional sections to represent the area between the fasteners. Additionally, it was assumed that the fasteners did not influence the delamination response prior to the crack reaching them. Although this was not entirely true because the fastener clamping force could provide some load transfer ahead of the fastener shank, this discrepancy was small enough to be negligible.

5.2.2 Modeling Results

The results of the one-dimensional modeling compared excellently with those of the two-dimensional models and experimental work. This boosted confidence in using the results of the one-dimensional models to perform parametric studies and in fatigue modeling. Additionally, in conjunction with the agreement between the reduced and fully detailed 2D model, the agreement suggested that using smeared material properties did not detrimentally affect the solutions.

5.3 THREE-DIMENSIONAL MODELING

Modeling in three dimensions was initiated to attempt to capture the crack tip curvature around the fastener as shown in previous C-scans. Initial attempts were made by Richard using solid elements [19] but were not successful in accurately capturing the solution. Rodriguez subsequently used shell elements to generate a finite element model that captured the crack shape across the width.

5.3.1 Initial FEA Model Design

The model was developed to mimic the design of the test article, which was originally comprised of 48 plies of AS4/3501-6 material, with the lamina properties summarized in table 1. The material system was subsequently changed to T800/3900-2 for further research, but the original material was used in the modeling because of the large number of existing experimental results that could be used for correlation. The layup used in most of the experiments and the FEM was quasi-isotropic, and each half was symmetric about its respective midplane and symmetric about the crack, with the total layup being $((0/45/90/45)_{3S}/\text{Crack})_S$ for a total of 48 plies. Of note, the nominal thickness of the specimen was 9.144 mm (0.36 inches) based on 48 plies of 0.19-mm (0.0075-inch) thick lamina. Although the measured thickness of the experimental specimens was 8.13 ± 0.254 mm (0.32 ± 0.01 inches), the nominal thickness was retained during the analytical work. Continuum shell elements (SC8R) were used in the model and VCCT was used to grow the crack [19].

5.3.2 Initial Modeling Results

To investigate the local distribution of the fastener preload in the layup of the specimen, a 1.25-inch square was modeled. This was determined to provide sufficient area for the preload distribution but minimized the computational cost of the model. All 48 individual lamina were modeled similar to the method used in the two-dimensional model. Each ply was one element thick, and the elements were assigned anisotropic properties, which corresponded to the direction of the layer in question. The model of the fastener was simplified because the intricacies of its response were not of interest. The bolt was modeled as three connected cylinders representing the shank, head, and nut. Thermal effects were included to account for stresses generated in the

laminate during the curing process by first solving the thermal problem in the plate and then using the solution as the initial conditions for the preload simulation. This was found to have a negligible effect on the final preload distribution. Finally, the preload was then applied using the ABAQUS "Bolt Load" utility, which adjusts the length of the bolt shank to generate the appropriate load in the fastener shank.

As seen in figure 66, the preload is asymmetrically distributed, with fiber direction of the laminate oriented vertically in (a), and at a 45^{o} angle in (b). This distribution is due to the anisotropic properties of lamina, which cause an asymmetric preload distribution, despite the layup being quasi-isotropic. This is of particular importance because the distribution of load transferred because of friction is affected by this distribution, changing the local strain energy release rates compared to an isotropic material. A comparison of the inclusion of thermal effects is not pictured, as there is minimal difference between the two cases. Whereas stress is induced through the curing process, this stress is generally in plane and is dwarfed by the stresses created by the preloading of the fastener.

Prior research has shown that the crack has significant curvature near the fastener. This is particularly important as the sample width becomes greater than 1.25 inches because the delamination could potentially steer entirely around the fastener instead of being forced to propagate through it, dramatically reducing the effectiveness of the arrest feature. Because of the computational requirements for a model incorporating 48 plies, only a simplified 16-ply model was generated. Otherwise, the modeling methodology remained the same as the local preload model. Although a mapped mesh was originally implemented to improve the crack-propagation characteristics, ultimately the mesh was generated using the ABAQUS default settings for the model to converge. As seen in figure 67, this results in an oddly shaped mesh. Further development of the model, in particular the mesh, did not occur because of a refocusing of efforts elsewhere.

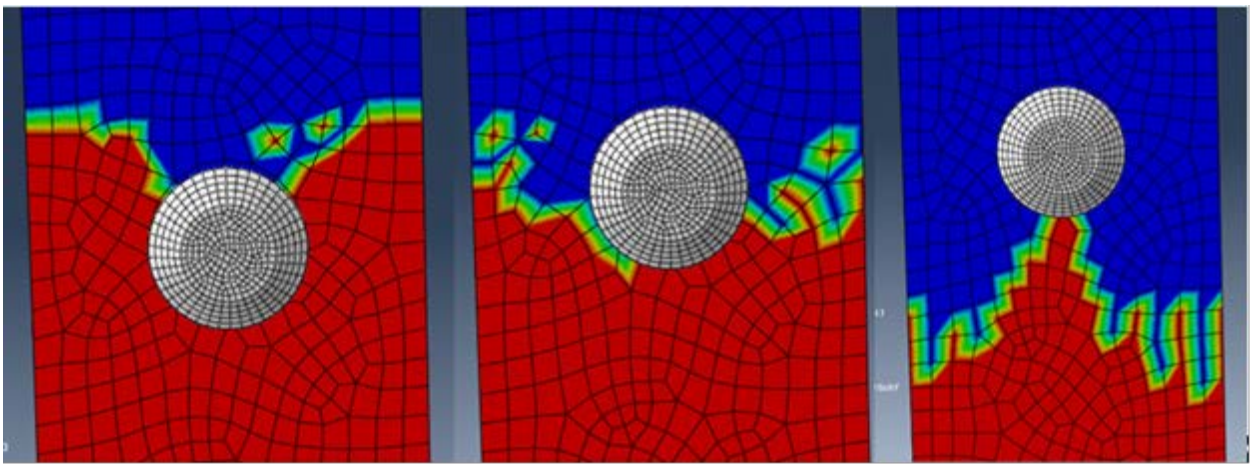

Figure 67. Crack curvature in three-dimensional model [19]

There is clear crack curvature shown in figure 68 as the crack propagates around the fasteners. The direction of propagation through the laminate is down as pictured. Interestingly, the crack initially curves in toward the fastener before reversing direction as the crack passes the fastener. The "islands" of bonded area visible in the figure are artifacts of the VCCT code interactions with the

free-form mesh and should be ignored. To investigate this curvature phenomenon, the fastener was removed and the simulation was again run both as a DCB and a two-point ENF specimen. In both cases, the crack front remained flat, which indicated that the fastener had significant influence on the propagation behavior while the simple inclusion of the hole did not. However, the exact mechanism by which the fastener increases the value of G nearby and in front of the hole is unknown. The curvature occurring as the crack passes the fastener can be explained by the engagement of the fastener. This reduces the stress in a localized area behind the fastener, causing it to remain bonded at a higher load compared to areas farther away. This has significant implications for crack-arrest arrays with spacing wider than the typical 5D. Obviously, as the bolt spacing becomes larger, a reduction in arrest control may be encountered because of crack propagation around, instead of through, the arrest features.

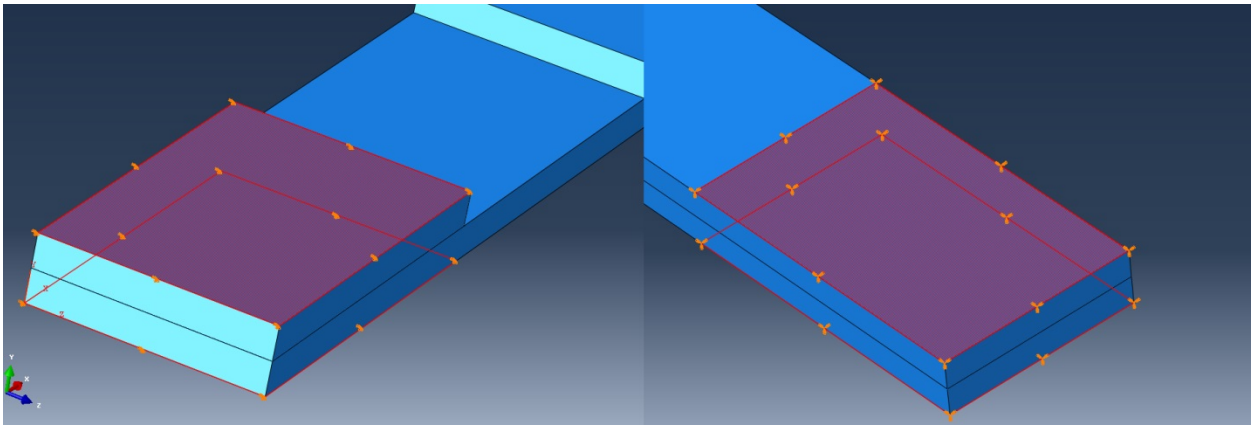

Figure 68. Model end constraints: (a) controlled displacement and (b) fixed [21]

A similar shape appears when comparing C-scans of the delaminated specimens in figure 61 with the simulations in figure 67. This indicates that the two-dimensional crack front simulated by VCCT can accurately capture the fastener-influenced zone. Subsequent development was carried out by Rodriguez [21] to improve the three-dimensional modeling because this was expected to be useful for more complex shapes in which the crack front may be a complex shape.

5.3.3 Revised Model Development

After initial simulations showed promise at capturing the curvature of the crack front, further work was carried out by Rodriguez [21]. As shown in figure 68, the finite element model replicates the experimental specimen but does not include the test fixture. Because the boundary conditions were not of particular interest, the grips were not modeled but instead approximated by fixed boundary conditions on one end and a controlled displacement that accurately approximated the tensile test machine without adding complexity to the finite element model. Whereas the eccentricity of the load due to the specimen design induced bending, the enforced displacements required the ends to remain horizontal, identical to the actual experimental situation (figure 69).

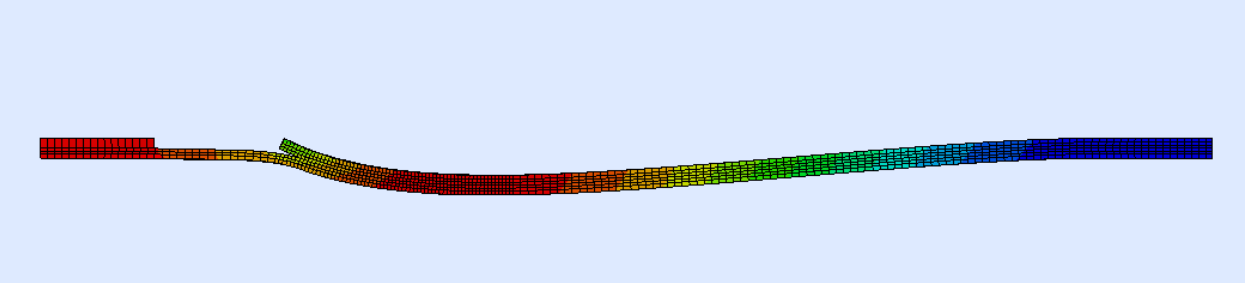

Figure 69. Displacement due to loading (exaggerated for visibilty) [21]

Within ABAQUS, the model was constructed of continuum shell elements (SC8R), which are eight-node quadrilateral shells with enhanced hourglass control. These elements were chosen because they better modeled the through the thickness behavior of composites when compared to conventional shells, and the enhanced hourglass control prevented unrealistic distortion, which would alter the strain energy of the system artificially. Finally, partitions in the model were utilized to ensure a uniform mesh despite the presence of the holes for the fasteners [21].

Avoiding artificial changes in the strain energy because of distortion was critical because the cracks were propagated via VCCT. This technique assumed that the force required to propagate a crack was equivalent to that required to close it, and the formulation allowed for the separation of the mode mix. This was subsequently implemented in ABAQUS FEA, allowing for the effective propagation of interlaminar cracks under mixed-mode loading [21].

When developing the model, it was decided to not include ply-level detail, but instead use smeared laminate-level properties, which were found utilizing classical lamination theory. This has the potential to reduce the accuracy of the simulation, but if all 48 plies were modeled individually, it would require more than 1.7 million elements. Even combining ply angle into a single thicker ply would only reduce the complexity to 500,000 elements, still a large number for VCCT simulations. This is because a VCCT simulation consists of individual static simulations as each node along the crack front is released. For the three-dimensional model, this was on the order of 25,000 nodes to be released, or up to 25,000 static simulations for one complete run. The ultimate solution was to use smeared properties and only three elements through the thickness, reducing the number of elements to 110,000 shells. Even with this number of elements, a full VCCT run typically took 24 hours to complete on a standard 4-core, 8-thread desktop computer with parallel processing enabled.

The ABAQUS preload feature was used to simulate the preloading of the fastener due to installation torque. When fasteners were installed, they were torqued to a specified value, which introduced a clamping load on the surfaces being joined, with the force known as the fastener preload. The actual value of preload was effectively unknown, however, as there was no general relation between installation torque and preload. Instead, the value was experimentally derived for this work. The average preload of 16 kN (3600 lb) was employed. Preloading was achieved automatically within ABAQUS by adjusting the length of the fastener elements so that there existed a traction force of the set magnitude at the specified plane.

After the preloading step was completed, the loading was applied to the model. The fully bonded end away from the crack tip was fully fixed, as discussed earlier. To minimize rotation, 50.8 mm (2 inches) of the length of the model was fixed in all degrees of freedom, as opposed to simply fixing the rear surfaces. The opposite end of the model was fixed in all degrees of freedom except for translation in *x* and, again, a 2-inch length of the model was restrained, replicating the test condition. A monotonically increasing tension load in the *x* direction was subsequently applied, and each time a node was released, indicating crack propagation, the load was recorded.

One minor detail in the implementation of VCCT in ABAQUS was that for three-dimensional structures, separating mode II and mode III was difficult. Mode III is defined as out-of-plane shearing, and in the formulation for ABAQUS mode II propagation out of the plane could be misidentified as mode III because it was shear out of the plane. To this end, it was decided to set $G_{IIC} = G_{IIIC}$. This was conservative as mode III was not found to arise in the tests performed. Additionally, mode III type delaminations in the plane were reported by the ABAQUS software as mode II delaminations occurring 90 degrees off the axis (defined to be the 2 direction). For a more general case in which true mode III propagation was a distinct possibility, additional modeling techniques in conjunction with accurate determination of G_{IIIC} must be used. .

5.3.4 Revised Modeling Results [21]

An immediately apparent result of the solution, shown in Figure 70, is the prevalence of mode III propagation near the edges of the specimen. This mode was greatest near the edges of the specimen, where the stress field tended to be nonuniform and the differential contraction of the loaded versus unloaded portions due to Poisson's ratio effects could contribute to the tearing mode.

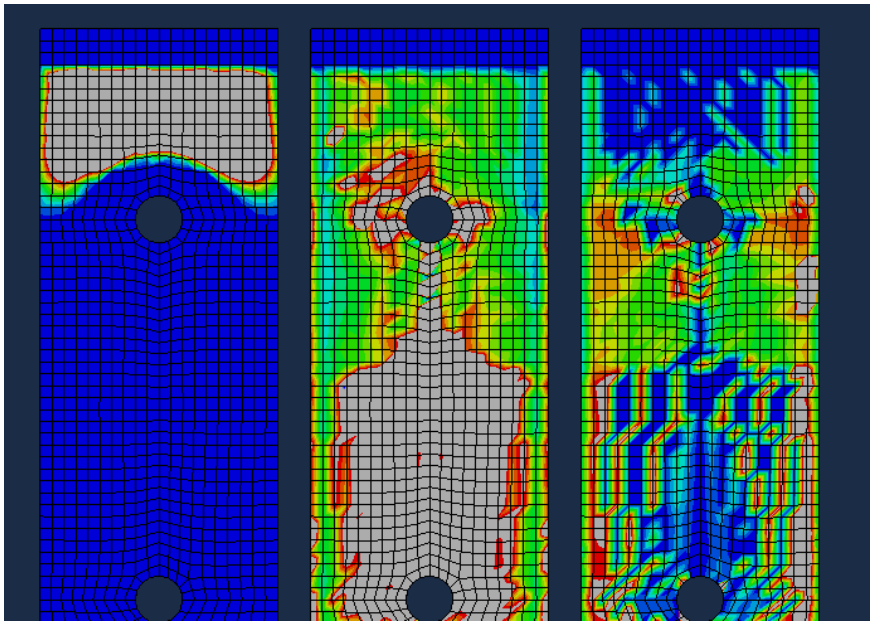

Figure 70. Decomposed SERR for delaminated face, (left to right, G_I, G_{II}, G_{III}) [21]

After the model was successfully created, the results were calibrated against the experimental and previously developed analytical models to determine the accuracy of the solution method. The crack length for the three-dimensional model was measured a quarter of the way across the specimen because this provided a reasonable average of the crack length when the crack tip was exhibiting significant curvature. Originally, zero preload and zero friction (marked 0/0) were run as a baseline model, and it can be clearly seen in figure 71 that this provided very bad agreement when compared to the two-dimensional models. Interestingly, two-dimensional models did not show nearly this level of disagreement when friction and preload were neglected. As a result, the same friction coefficient (0.25) and preload (16 kN or 3600 lb) were used, and agreement was significantly improved. Note, however, that the curve appears shifted compared to previous results. This can be explained by the location of measurement. As the measurement was shifted closer to the centerline, the horizontal shift was reduced.

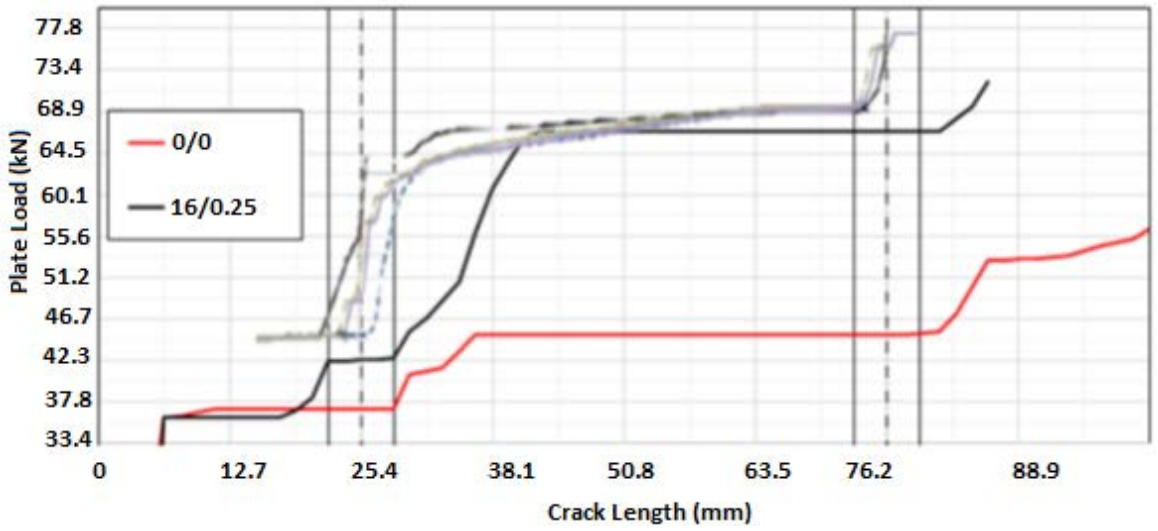

Figure 71. Two-dimensional vs. three-dimensional model correlation [21]

The importance of properly applying the friction and preload in a three-dimensional model is significantly greater than that of the two-dimensional model. As shown in figure 72, there is a significantly different response between a preloaded and a non-preloaded simulation. When the preload is introduced, mode I is suppressed significantly sooner than expected because the laminate is much more tightly clamped together. With zero preload, the fastener does not actually suppress mode I until it is actively being stretched. This is unrealistic for typical structures in which fasteners are installed with significant levels of preloading.

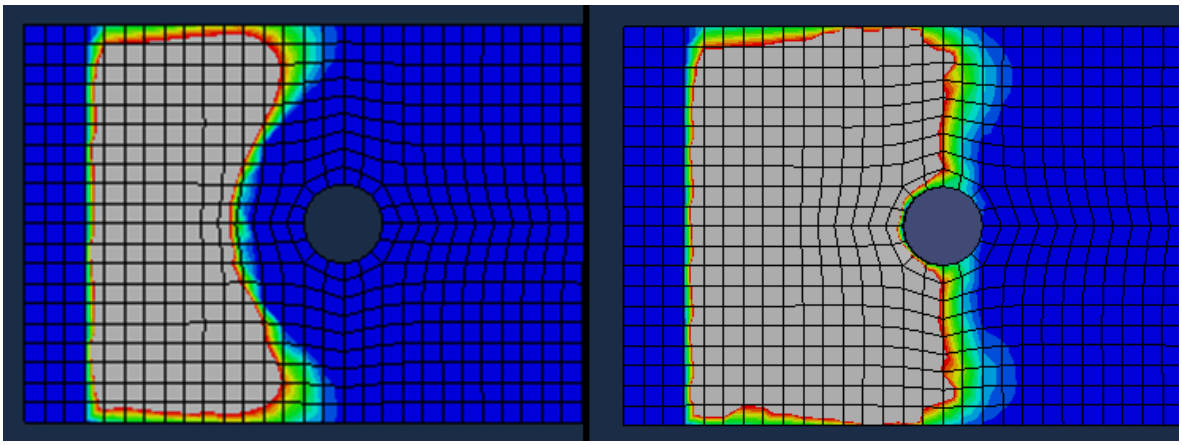

(a) (b)

Figure 72. Preloaded (a) vs. non-preloaded (b) G_I (16kN/0.25 a, 0/0 b) [21]

Additionally, this preload provides non-negligible load transfer through friction, which tends to generate the characteristic curvature around the fastener of the crack front. The load alleviation through friction is focused underneath the fastener head in a similar manner that mode I is suppressed most effectively below the fastener. As a result, the strain energy release rates are lowest near the fastener, where friction is providing load alleviation. Near the edges of the specimen, where the fastener influence is less, the crack continues to advance at a greater rate.

6. FASTENER ARRAYS

Throughout all previous work, the assumption was applicable for a strip model (i.e., a 2x2 fastener array would behave in the same manner as two 1x2 strips adjacent to one another). However, this was never previously tested. Samples were fabricated in the same manner as before but cut to a width of 2.5 inches, and fasteners were installed in a 2x2 pattern with a spacing of 1.25 inches across and 2 inches down the sample, mimicking two single strips butted together.

Testing of the samples was conducted in the same manner as before, and C-scans were taken during testing of the various samples. Figure 73 shows scans taken during initial propagation past the first fasteners and the full extent of delamination at the end of testing. The crack curvature of each strip looks similar to that of the previous samples, supporting the applicability of the strip-modeling technique.

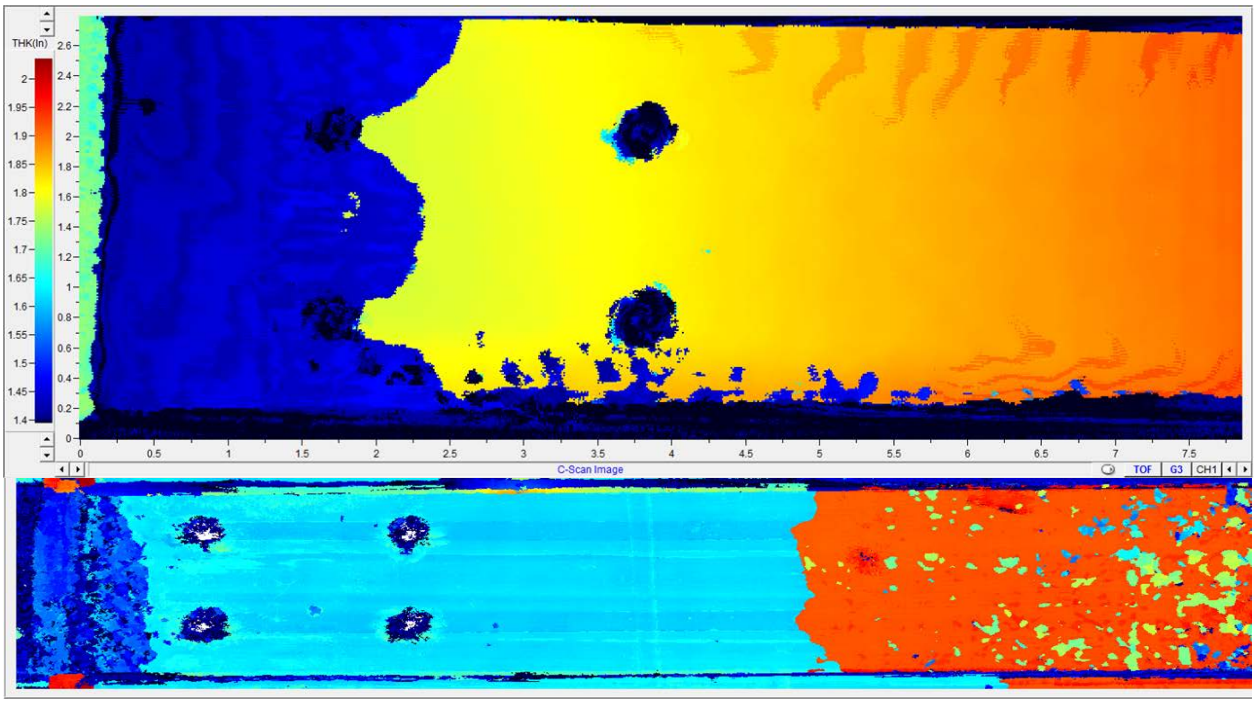

Figure 73. 2x2 array C-scans (yellow/red is bonded) [20]

7. PRACTICAL APPLICATIONS OF DELAMINATION ARREST FEATURES

In an ideal scenario, a structure can be designed such that it will not experience delamination or disbond propagation under fatigue and static loadings, even with the presence of manufacturing flaws. This can be achieved, for instance, by carefully ramping laminate thickness up or down, avoiding discrete transverse loading, or managing multiple-load path structures to reduce local moments to reduce the interlaminar tension and opening moment that are the most detrimental to delamination and the disbond mode of failure. In theory, a perfectly designed structure will not need any delamination-arrest fasteners.

In practice, the desired ply ramp up/down ratio cannot always be achieved because of engineering and other design constraints. Delaminations can initiate anywhere in the structure as manufacturing flaws or in-service damage. Orthogonal structural details, such as ribs and fittings, exert transverse loading and local moments on skins. One can easily realize the value of using arrest fasteners to provide an insurance policy for structural integrity.

In laminated composite structures, each matrix interface is a potential weak link for interlaminar failure. In thin and low-strain applications, the load going through each matrix interface is relatively small compared to the strength of the matrix. Such structures are generally tolerant of small delaminations. However, matrix-interface strength does not scale up with thickness or stress/strain. Structures become increasingly intolerant of delaminations as the structures get bigger and thicker, and the loadings get closer to the laminate in-plane strength. Aerospace vehicles are examples of such applications in which structural weight efficiency is paramount. In these cases, the use of arrest fasteners could become one of the few feasible ways to guarantee structural integrity. Lastly, the current 14 CFR 23.573 for damage tolerance and fatigue evaluation of

composite structures provides that an effective arrest mechanism is one way to substantiate a bonded joint (whereas the other two methods are either impractical or lack technological maturity). Therefore, it makes sense to have the delamination-arrest fastener in the engineers' standard toolbox.

From the test results shown, it is clear that delamination can propagate past the fastener when there is sufficient applied load. Therefore, the definition of arrest capability requires a narrower interpretation that depends on knowledge of the loads and growth assessments.

It is recommended that the arrest capability be measured as the highest load at which the crack front remains stuck under the fastener (i.e., that is, the top of the arrested phase, as shown in figure 23). The additional capability in the stable-propagation phase may be referred to as "retardation capability." From a practical perspective, it is undesirable to rely on the retardation capability demonstrated in the stable propagation phase. First, a small exceedance in load can result in large-crack propagation. Second, crack-face friction and fastener-hole clearance can lead to large unstable crack propagation when the crack tip exits the fastener area. Third, large-crack extension can result in structural nonlinearity by locally reducing the stiffness of the structure. This can distribute load into neighboring features and can cause cascading failures. Also, competing failure modes can be activated, drastically complicating residual strength analysis. Last, in the arrested phase, most of the benefit of the arrest fastener has already been realized, and crack location can be confidently controlled. Therefore, it is preferred to design for crack arrestment at the fastener but not past it.

The test results demonstrate appreciable improvements in load-carrying capability by the arrest fastener. However, it must be cautioned that the magnitude of improvement is dependent on the configuration of the structure and the load case. The magnitude of the improvements shown cannot be applied to a generic structure.

The delamination arrest fastener provides arrest capability via three main mechanisms: 1) mode I suppression, 2) crack-face friction, and 3) fastener-joint shear stiffness. Mechanisms 1 and 2 provide the benefit seen in the arrested phase, while mechanism 3 provides the additional retarding capability in the stable-propagation phase. The parameters that dictate the performance of mechanisms 2 and 3 are structural parameters (e.g., fastener size, install torque, laminate layups) and are generally fixed for a given structural design and manufacturing process. The benefit provided by mechanism 1 is primarily a result of the load case. That is, if the load case yields a lot of mode I opening at the crack tip, mode I suppression will yield a lot of benefit. Conversely, if the load case yields no mode I opening, the mode I suppression mechanism would yield no benefit. Therefore, the expected benefit in the arrested phase is not only dependent on the structural design parameters, but also the load cases, so it will be incorrect to simply coin a fixed load-capability improvement or percentage improvement for a given fastener and installation torque. The actual benefit realized by employing an arrest fastener must be determined by analyzing the structure with and without a fastener for the given load case. For example, if the load case is such that the crack tip is in pure mode II, and a conservative assumption of frictionless crack face is used, one can expect no benefit in the arrested phase at all. The designer/analyst must have a good understanding of the mechanics of mixed-mode fracture in laminated composites to have realistic expectations of the performance of crack-arrest fasteners.

Parametric analyses show that the G_{IIC} of the composite material system has the highest leverage in improving the load capability in conjunction with an arrest fastener. This is an interesting outcome because the majority of past efforts in material development primarily focused on G_{IC} and matrix tension strength. However, with an arrest fastener, both crack opening and matrix tension are suppressed, and crack propagation becomes primarily a mode II affair.

The second-most-important parameter is crack-face friction. However, factors affecting it, such as fastener preload and crack-face coefficient of friction (an interface property), are notoriously difficult to predict, measure, or control. Crack-face friction is dependent on the ply orientations bounding the interface, and it changes under fatigue loading. Fastener preload cannot be directly controlled. Fastener installation standards only specify installation torque, which is measurable during the installation process. However, the final preload also depends on hidden parameters, such as thread friction and head/washer/nut face friction. Only specially instrumented fasteners enable the tension preload to be determined. In addition, the preload decreases over the life of the structure because of viscoelastic relaxation of the laminate under compression. All these mean that the precise arrest capability is difficult to quantify with confidence.

Fastener flexibility, or joint shear stiffness, determines the propagation behavior in the stable propagation phase. However, large crack extensions must be accepted if the designer wants to take advantage of the retardation capability provided by the joint shear stiffness. In this study, with the split-beam configurations tested and analyzed, the joint shear stiffness appears to provide only limited retardation capability beyond the initial arrestment at the fastener.

8. FUTURE WORK

With the completion of the static testing and simulation, future work will look into fatigue delamination propagation and arrest. The interlaminar region is particularly susceptible to fatigue delaminations because it does not have the natural crack-arrest feature of the fibers. Additional work is suggested to explore the fastener design space and the response of fastener arrays in fatigue. The work here has shown that the current fasteners used are highly capable of arresting delaminations under static loading, but there has been no work on improving the efficiency of the design.

8.1 FATIGUE

Fatigue delaminations are of particular concern in aircraft structures, particularly because those propagating in mode II are difficult to detect, and it is possible that mode I could reappear because of a lack of clamping pressure should they grow a sufficient distance away from any fasteners. Additionally, under static loading, it is noted that the delayed engagement of the fastener in shear has negative consequences on the arrest capability. With fatigue loading, initial testing has shown that the lower loads result in small enough displacements that the fastener shanks do not engage in shear, eliminating one of the methods through which the fastener arrests cracks.

8.1.1 Tension

Initial work in tension-tension fatigue [20] has shown that fatigue delaminations are highly sensitive to the installation torque, in addition to the clearance of the fastener. For moderate

loading, the fasteners, particularly the second fastener, do not engage in shear, but are providing load transfer only through friction. Loosening of this fastener results in significantly greater crack propagation compared to a fastener tightened to 40 in-lb.

8.1.2 Compression

Mode II delaminations are theoretically independent of loading direction. Compression loading of the same amplitude should drive delaminations in an equivalent manner to tensile loading. As of publication, this has not been studied, and verification of this postulation is suggested. One particular obstacle is the prevention of buckling, both of the global laminate and the delaminated sublaminates. Buckling of the sublaminates will additionally reintroduce mode I, changing the propagation behavior significantly.

8.1.3 R Ratio Effects

The Paris law, along with its modified version to account for R ratio, was developed for metallic structures, but it has shown to be largely applicable for fatigue delaminations in composites. However, R ratio effects have not been studied as of yet. It is hoped that the same principles will hold true, allowing for continued use of these formulations.

8.2 FASTENER DESIGN SPACE EXPLORATION

Current work has not changed the fastener specifications, but suggests that the current specifications are significantly overdesigned for preventing delamination propagation under realistic load levels. Most of the propagation was occurring above 75% of the ultimate load of the sample, a level which is expected to very rarely, if ever, occur in actual structures. As a result, exploring the fastener design space could generate improved fastener systems.

8.3 FASTENER ARRAYS IN FATIGUE

A final area of interest is the response of fastener arrays in fatigue. Currently, only a square pattern has been used in the fastener arrays to validate the strip model. However, it is possible that more efficient patterns, such as a staggered one to take advantage of the crack curvature, may be better.

9. CONCLUSIONS

The effective arrest capability and limitations of fasteners has been demonstrated. Similar to common primary composite aircraft structures, the specimen initially generates a mixed-mode propagation state, which then demonstrates the ability of the fastener to eliminate mode I propagation. Variations in laminate layup and thickness have shown that the model retains reasonable predictive accuracy, and correlation between test and experimental results has shown which parameters must be understood to capture the process.

The clamping effect of the fasteners has been shown to eliminate mode I propagation for a significant linear distance, allowing for an increased spacing of the fasteners in a crack-arrest configuration compared to what is typical for load transfer. Meanwhile, the analysis has indicated

that the fastener joint stiffness is the primary force resisting propagation, with friction providing a noticeable benefit.

As a result, the number of fasteners and their pitch are primarily driven by the maximum allowable crack length. Because fasteners are generally only effective once the crack has reached or passed them, reducing the fastener spacing will cause more fasteners to engage at a shorter crack length, reducing the maximum crack length. Additionally, more fasteners will tend to arrest the crack in a shorter distance, as visible when comparing the results shown here compared to previous single-fastener results in which zero clearance fasteners required approximately 5 inches to arrest a crack versus approximately 2 inches when two fasteners are used.

10. REFERENCES

1. Bruun, E.D., Cheung, C.H., Gray, P.M., Lin, K.Y. (2012). *Design and Experimental Validation of a Mixed-Mode Crack Arrest Specimen*. Proceedings from the 53rd AIAA/ASME/ASCE/AHS/ASC Structures, Structural Dynamics, and Materials Conference. Honolulu, HI.

2. Gray, P. (2012). *Experimental and Analytical Study of Mode II Interlaminar Failure of Bolted and Bonded Composite Structures* (M.S. Thesis). Department of Aeronautics and Astronautics, University of Washington, Seattle, WA.

3. Cheung, C.H. (2016). *Delamination Arrestment in Bonded-Bolted Composite Structures by Fasteners* (Ph.D. Dissertation). Department of Aeronautics and Astronautics, University of Washington, Seattle, WA.

4. Jen, M-H. R., Lin, W.H. (2000). Innovative Fracture Tests of Single-Lapped Bolted and Bonded Composite Joints. *Journal of Reinforced Plastics and Composites, 19*(18), 1444–1473.

5. Jen, M-H. R., Lin, W.H. (1999). Strength of Bolted and Bonded Single-Lapped Composite Joints in Tension. *Journal of Composite Materials, 33*(7), 640–666.

6. Lee, Y.H., Lim, D.W., Choi, J.H., Kweon, J.H., Yoon, M.K., (2010). Failure Load Evaluation and Prediction of Hybrid Composite Double Lap Joints. *Composite Structures*, *92*(12), 2916–2926.

7. ASTM Standard D6671/D6671M-06, "Standard Test Method for Mixed Mode I-Mode II Interlaminar Fracture Toughness of Unidirectional Fiber Reinforced Polymer Matrix Composites," ASTM International, West Conshohoken, Pennsylvania, 2006, DOI: 10.1520/D6671_D6671M-06, www.astm.org.

8. Todo, M., Nakamura, T., Takahashi, K. (1999). Mode II Interlaminar Fracture Behavior of Fiber Reinforced Polyamide Composites under Static and Dynamic Loading Conditions. *Journal of Reinforced Plastics and Composites, 18*(15), 1415–1427.

9. Carlsson, L.A., Gillespie, J.W., Pipes, R.B. (1986). On the Analysis and Design of the End Notched Flexure (ENF) Specimen for Mode II Testing. *Journal of Composite Materials, 20*(6), 594–604.

10. Tate, M.B., and Rosenfeld, S.J. (1984). "Preliminary Investigation of Loads Carried by Individual Bolts in Bolted Joints," Technical Note No. 1051, National Advisory Committee of Aeronautics, 1984."

11. Huth, H. (1986). "Influence of Fastener Flexibility on the Prediction of Load Transfer and Fatigue Life for Multiple-Row Joints," *Fatigue in Mechanically Fastened Composite and Metallic Joints, ASTM STP 927*, John M. Potter, Ed., American Society for Testing and Material, Philadelphia, pp. 221–250.

12. NASA Report. (2002). The Virtual Crack Closure Technique: History, Approach and Applications. (NASA/CR-2002-211628, ICASE Report No. 2002–10).

13. Mabson, G.E., Deobald, L.R., Dopker B. (2007). *Fracture Interface Elements for the Implementation of the Virtual Crack Closure Technique*. Proceedings from the 48th AIAA/ASME/ASCE/AHS/ ASC Structures, Structural Dynamics, and Materials Conference, Honolulu, HI.

14. Wang, J., Qiao, P. (2006). Fracture Analysis of Shear Deformable Bi-Material Interface. *Journal of Engineering Mechanics*, *132*(3), 306–316.

15. Hart-Smith, L. J., (1982). "Design Methodology for Bonded-Bolted Composite Joints." Technical Report AFWAL-TR-81-3154, Douglas Aircraft Company.

16. Kelly, G. (2006). Quasi-static strength and fatigue life of hybrid (bonded/ bolted) composite single-lap joints. *Composite Structures, 72*(1) 119–29.

17. Odagiri, N., Muraki, T., Tobukuro, K. (1988). *Toughness Improved High Performance Torayca Prepreg T800H/3900 Series.* Proceedings from the 33rd International SAMPE Symposium, Anaheim, CA.

18. Cheung, C.H., Lin, K.Y. (2012). Numerical Analysis of Fastener Delamination/Disbond Arrest Mechanism in Aircraft Composite Structures. *Journal of aircraft, 49*(2), 630–635.

19. Richard, L. (2013). *Experimental and Analytical Study of Delamination Arrest by Multiple Fasteners in Composite Structures* (M.S. Thesis). Dept. of Aeronautics and Astronautics, University of Washington, Seattle, WA.

20. Lin, K.Y., Richard, L. (2016). *Analytical and Experimental Studies on Delamination Arrest in Bolted- Bonded Composite Structures*. Proceedings from the 2016 AIAA SciTech Forum, San Diego, CA.

21. Rodriguez, P. (2015). “Analytical study of delamination arrest features in ABAQUS FEA”, Master of Aerospace Engineering Project, Dept. of Aeronautics and Astronautics, University of Washington, Seattle, WA.

22. Liu, W. (2014). *Analysis of Delamination Arrest in Bolted-Bonded Composite Structures* (M.S. Thesis). Dept. of Aeronautics and Astronautics, University of Washington, Seattle, WA.

APPENDIX A—RAW PROPAGATION LOAD DATA

Short Panel – Quasi-isotropic layup

	#3 (no tab)	#1 (no tab)	#5 (no tab)	#7 (no tab)	#6 (with tab)	#4 (with tab)	#2 (with tab)
Fastener Installation Torque	**47.0 in-lb**	**47.0 in-lb**	**finger-tight**	**finger-tight**	**21.4 in-lb**	**21.4 in-lb**	**21.4 in-lb**
Crack-Tip Location (in)	**Propagation Load in kN**						
-1 6/8							
-1 5/8							
-1 4/8							
-1 3/8							
-1 2/8							
-1 1/8	~~~	~~~	~~~	~~~	~~~	~~~	~~~
-1	40.2	37.8	34.7	39.1	43.5	41.2	40.8
- 7/8							
- 6/8							
- 5/8							
- 4/8							
- 3/8							
- 2/8	40.2	37.8	34.7				
- 1/8	48.7	45.7	38.8	39.1		41.2	40.8
0	55.3	54.5	47.2	45.0	43.5	52.2	45.1
1/8	58.2	59.5	52.6	50.3	45.8	55.1	48.8
2/8	64.7	62.2	55.3	52.3	50.4		51.0
3/8		63.8	56.3	52.8	53.5		54.7
4/8	64.1	65.2	57.2	54.5	54.5		56.7
5/8		65.5			55.8	60.2	
6/8			57.6	55.7			58.7
7/8				56.4		60.3	59.0
1			58.2		56.5		59.4
1 1/8	63.9				57.8		60.1
1 2/8					58.3	60.4	60.7
1 3/8						61.1	
1 4/8		66.3		57.0	58.5		61.1
1 5/8					59.0	61.7	61.3
1 6/8	64.1	66.4	58.7		59.5	62.2	61.5
1 7/8	64.5	66.7	59.1	57.5	60.0	63.3	62.4
2	64.6	66.9	59.8	59.1	60.5	63.6	62.7
2 1/8	64.9	66.9	60.1		61.2	63.9	63.6
2 2/8	65.3		60.4	59.8	61.9	64.3	64.3
2 3/8	65.8	67.1		60.0	62.4	64.8	64.7
2 4/8	65.6	67.5			63.1	65.4	65.1
2 5/8	66.5				63.8	65.7	65.8
2 6/8		67.5			64.2	65.7	67.0
2 7/8	67.1				64.9	66.3	67.8
3	67.5	67.9			65.5	66.9	68.6
3 1/8	68.0	68.8			65.9	67.9	69.5
3 2/8		70.1			66.4	68.3	69.9
3 3/8		70.6			66.7	69.3	70.4
3 4/8		70.6			67.4	70.2	70.9
3 5/8					67.5		71.3
3 6/8							72.0
3 7/8							
4							76.5
4 1/8							
Final Failure Mode	**FHT**	**At Grip**	**At Grip**	**At Grip**	**FHT**	**stopped**	**FHT**

Short Panel – 50% 0° layup

	1	3	2	4	5	6	7	8
Fastener Installation	**50 in-lb**	**50 in-lb**	**finger tight**	**80 in-lb**	**21 in-lb**	**80 in-lb**	**21 in-lb**	**finger tight**
Crack-Tip Location (in)	**Propagation Load in kN**							
-1	40.5	41.7	43.0	40.3	41.9	39.4	38.3	37.7
- 7/8								
- 6/8								
- 5/8								
- 4/8								
- 3/8			43.0				38.3	
- 2/8							46.7	
- 1/8	40.5	41.7		40.3		39.4	50.5	
0	42.8	41.8		52.8	41.9	50.1	59.2	37.7
1/8	51.3	52.1		64.9	50.0	59.4	64.6	46.1
2/8	55.7	56.2	43.1	71.1	59.1	65.8	68.3	50.3
3/8	60.4	63.7	48.1	77.2	64.1	75.5	70.6	54.9
4/8	66.6	70.4	54.8	79.5	69.1	76.7		59.4
5/8		74.1	58.8		75.5			60.8
6/8		76.0	62.8					61.9
7/8								62.1
1								62.3
1 1/8								62.3
1 2/8								
1 3/8								
1 4/8								
1 5/8								
1 6/8							70.7	
1 7/8			63.0					
2							69.7	62.0
2 1/8	68.7		62.7				70.4	
2 2/8								62.0
2 3/8	67.3							
2 4/8			63.7				70.7	
2 5/8	67.6							
2 6/8	67.9		64.0	80.9		77.5	71.5	
2 7/8	68.4			78.9				
3	69.0		65.6		76.6	74.5	71.6	61.9
3 1/8	69.4	80.0	66.7	79.1			72.2	
3 2/8	69.9	76.1			72.8	74.7	72.5	
3 3/8	70.3	76.4		79.6			73.0	
3 4/8	70.5	77.1	68.0	80.5	74.0		73.5	62.1
3 5/8	71.6	77.7	68.9	81.5		76.3	73.8	
3 6/8	72.0			82.0				63.0
3 7/8	72.1	77.8	69.8		75.4	77.1		
4	72.3			82.3			74.0	63.2
4 1/8	72.5		69.9	82.9			74.7	
4 2/8	72.7	77.6	70.0		76.0		75.7	
4 3/8	73.5			83.3				63.5
4 4/8	74.1	78.1	70.4	83.4	76.5		75.9	
4 5/8	74.9				76.9			63.8
4 6/8	75.4		71.1	83.8	77.0	78.5	76.3	
4 7/8	75.8				77.3		76.9	64.4
5	76.4	78.5	71.9	84.0	77.7	80.0	77.6	65.2
Final Failure Mode	**Delam Reached Grip**	**Delam Reached Grip**	**Delam Reached Grip**	**Delam Reached Grip**	**Delam Reached Grip**	**Delam Reached Grip**	**Delam Reached Grip**	**Delam Reached Grip**

Long Panel – Quasi-isotropic layup (1 of 2)

	1	2	3	4	5	6	7	8
Fastener Installation Torque	**finger-tight**	**finger-tight**	**20in-lb**	**20in-lb**	**50in-lb**	**50in-lb**	**80in-lb**	**80in-lb**
Crack-Tip Location (in)	**Propagation Load in kN**							
-1								
-15/16								
-14/16								
-13/16								
-12/16								
-11/16								
-10/16								
- 9/16								
- 8/16								
- 7/16								
- 6/16								
- 5/16								
- 4/16							32.4	
- 3/16							36.5	
- 2/16							39.2	
- 1/16							43.4	
0						36.8	45.5	35.7
1/16				37.1		39.3	46.6	39.8
2/16			34.2	38.2	36.3	42.5	48.5	43.3
3/16			34.7	39	38.2	43.8	51.5	45.4
4/16			37	40.7	38.8	44.6	54	46.7
5/16			39	44.1	42.9	45.6	55	47.3
6/16	35.8	34.4	41.2	46.1	45.1	48.3	55.6	49
7/16	37.6	38.5	42.7	50.5	45.9	51.7	56.4	52.5
8/16	40.3	40.3	44.5	52.3	47.1		57.6	53.1
9/16	43	43	46.5		50.2		58.6	56.7
10/16	45.8	43.5			53.5		59.5	58.2
11/16		44					61.5	58.5
12/16	46.5	44.5						59.6
13/16		45		53				
14/16	47.4	47		53.5				
15/16				53.9				
1	48.6			54.1				
1 1/16				54.3				
1 2/16			52.8	55				
1 3/16				55.2				
1 4/16		48.5	53.8	55.4	56.2	52		
1 5/16								
1 6/16		49.5	54.4	55.8	56.4	53		
1 7/16				56.3				
1 8/16	51.2		55.3		56.8			
1 9/16								
1 10/16		50.8	57	57.1	57.5	53.5		
1 11/16						53.8		
1 12/16	51.8	51.3	58.4	57.5	58	54.1		
1 13/16				57.7		54.3		
1 14/16	53.1	51.7	59.1	57.9	58.5	54.5		
1 15/16								

Long Panel – Quasi-isotropic layup (2 of 2)

	1	2	3	4	5	6	7	8
Crack-Tip Location (in)	**Propagation Load in kN**							
2		52	59.8	58.2		54.8		
2 1/8								
2 2/8		52.4	60.3	58.6		55.3		
2 3/8						55.8		60.3
2 4/8	54	52.9	62.8	58.8		56.1		
2 5/8						56.2		
2 6/8	56.4	54	65.3	59.1		56.5		60.8
2 7/8						57.1		
3	57.5	56	67.3	60.9		57.6		61.4
3 1/8						57.8		62.1
3 2/8	58.4	58.1	68.8	61.8		57.9		62.9
3 3/8						58.3		63.5
3 4/8	60.1	61.5		63.4		58.6		64.7
3 5/8						59.2		65.3
3 6/8	63.2	63.1		64		59.4		65.7
3 7/8						59.7		66.1
4	65.5	64.4		64.7		60		66.6
4 1/8						60.8		
4 2/8	66.4			65.4		62		66.6
4 3/8						63.2		67
4 4/8	66.9			66.1		63.8		67.3
4 5/8						65		67.6
4 6/8	67.3	65.4		66.8		66.1		68
4 7/8						66.7		68.6
5	67.8	67.1		67.6		67		69.5
5 1/8						67.2		
5 2/8		68.9		69		67.4		70
5 3/8						67.8		
5 4/8	68.3	69.8		71.2		68.5		
5 5/8								
5 6/8	69.2	71.1		71.8		69.3		
5 7/8								
6	70.5	71.6		73		69.7		
6 1/8						70.3		
6 2/8	71.1			74.1		72.1		
6 3/8								
6 4/8	71.5							
6 5/8								
6 6/8	72							
6 7/8								
7								
7 1/8								
7 2/8								
7 3/8								
7 4/8								
7 5/8								
7 6/8								
7 7/8								
8								
8 1/8								
Final Failure Mode	**FHT**	**FHT**	**FHT**	**FHT**	**Slipped from grip**	**FHT**	**Slipped from grip**	**FHT**

Long Panel – 50% 0° layup (1 of 2)

	1	2	3	4	5	6	7
Fastener Installation Torque	finger-tight	finger-tight	20in-lb	20in-lb	50in-lb	80in-lb	80in-lb
Crack-Tip Location (in)	Propagation Load in kN						
-1			44	33		35.5	
- 15/16				33.3			
- 14/16				33.5			
- 13/16				33.9			
- 12/16				34.6			
- 11/16				35.4			
- 10/16				37.2			
- 9/16				38			
- 8/16				38.8			
- 7/16							
- 6/16			44.5				
- 5/16							
- 4/16		31.8	47.2				
- 3/16		34.6				35.7	
- 2/16	29.8	37.3	48.5			36.9	
- 1/16	36.3	42				38.3	
0	40	45.8	49.3			39.4	
1/16	44	47.1	51.5				
2/16	45.4	49.7	52.2		52.2	43.3	49.6
3/16	49.2	52.7	54		52.7	45.9	50.3
4/16	50.8	53.6	55.9		53.3	49.3	53.6
5/16	55	54.3			54	52.1	54.8
6/16	56					53.7	56.1
7/16	57.4					56.4	59.7
8/16	58.6		59.6		66.8	59.3	62.7
9/16					68.1	62.5	63.9
10/16			60.3				67.1
11/16							68.7
12/16		56.9					70.3
13/16							
14/16		57.5					
15/16				65.9			
1	59.2	57.7	64				
1 1/16	59.5						
1 2/16	59.7	58.6	64.3	66.5			
1 3/16							
1 4/16	60.1	59.4	64.6				
1 5/16				66.8			
1 6/16	61.3		66				
1 7/16							
1 8/16	62	60.5	67	67.7			
1 9/16							
1 10/16	62.8	60.7	67.5	68.2			
1 11/16							
1 12/16	63.7	61		68.8			
1 13/16							
1 14/16	64.1	61.3	67.8	70.4			
1 15/16				71.1			

Long Panel – 50% 0° layup (2 of 2)

	1	2	3	4	5	6	7
Crack-Tip Location (in)	Propagation Load in kN						
2	64.5	61.6	68	71.4	71.7		
2 1/8	65.1		69.5				
2 2/8	65.7		71.6	71.8			71.1
2 3/8	66	61.7	72	72		70.5	
2 4/8	66.2	62.5	74	72.5			
2 5/8	66.3	63.6		72.8			
2 6/8	66.5		75.3	73.1			
2 7/8	67.1	65	76.1	73.5			73.5
3	67.4		77	75.3	72.1	70	
3 1/8	67.8		77.2	76.3			75.1
3 2/8	68.2	65		78.1	73.9	71.1	75.4
3 3/8	68.6			78.8		71.6	
3 4/8	69.8		77.6	79.6	74.2	71.9	
3 5/8	70.4	65		80.1	74.8	72.2	75.6
3 6/8	70.7				75.8		75.7
3 7/8	71.1	66	78.8		76.4	74.2	76.3
4	71.7	66.7	79.3	81.4	76.8		
4 1/8	72.3	67		81.9	77.2		
4 2/8	73.1		80.1		77.4	75.6	
4 3/8	73.5			82.6	78.4		
4 4/8	74	67.4		82.9		76.3	80.3
4 5/8	74.4		81.3	83.1	78.7		81.1
4 6/8	74.7			83.4	79.1	77.5	81.8
4 7/8	75.4	67.7			79.7		82.9
5	76.4	69.3	82.5	84.2	80.5	79.3	83.5
5 1/8	76.9	70.2	82.9	85			
5 2/8	77.3	71.1		85.2	80.9	80.3	84
5 3/8	77.5	72		85.5	81		84.2
5 4/8	78	72.9		85.7	81.8	81.6	
5 5/8	78.5	73.8	82.5		82.1		85.7
5 6/8	78.8	75.6	83.4	85.7	82.7	81.9	
5 7/8	78.9	76.1	83.7			82.3	
6	79.1	76.5	84.3	85.9		83.1	86.8
6 1/8	79.3	77.6	85		83.7	83.2	
6 2/8	79.5	79.3	85.7	85.9	84.1		
6 3/8	79.8	80.4				85.1	87.3
6 4/8	80	81.5			86.2		87.6
6 5/8	80.3	82.6					88.7
6 6/8	80.6	83.3		86.2	86.4		89.5
6 7/8	80.9	84.2			86.4		
7	81.5	85.4		86.3		86.3	
7 1/8	82.1	86.3			86.7	86.7	90.6
7 2/8	100.3	86.6					91
7 3/8					87.4	89.6	
7 4/8				86.6	87.5	90.2	
7 5/8					88.1	90.5	
7 6/8		86.6			89.7		
7 7/8				86.6	90.6		
8		87.5			91.3		
8 1/8					92.3		
					93.4		
	FHT	Slipped from grip	Slipped from grip	FHT	FHT	FHT	FHT

APPENDIX B—MATLAB® FILES

MATLAB® files omitted because of length; available on request.